

DEVELOPMENT OF A HIGH DYNAMIC RANGE
PIXEL ARRAY DETECTOR FOR SYNCHROTRONS
AND XFELS

A Dissertation

Presented to the Faculty of the Graduate School
of Cornell University

in Partial Fulfillment of the Requirements for the Degree of
Doctor of Philosophy

by

Joel T. Weiss

December 2017

© 2017 Joel Weiss
ALL RIGHTS RESERVED

DEVELOPMENT OF A HIGH DYNAMIC RANGE PIXEL ARRAY DETECTOR FOR SYNCHROTRONS AND XFELS

Joel T. Weiss, Ph.D.

Cornell University 2017

Advances in synchrotron radiation light source technology have opened new lines of inquiry in material science, biology, and everything in between. However, x-ray detector capabilities must advance in concert with light source technology to fully realize experimental possibilities. X-ray free electron lasers (XFELs) place particularly large demands on the capabilities of detectors, and developments towards diffraction-limited storage ring sources also necessitate detectors capable of measuring very high flux [1–3]. The detector described herein builds on the Mixed Mode Pixel Array Detector (MM-PAD) framework, developed previously by our group to perform high dynamic range imaging, and the Adaptive Gain Integrating Pixel Detector (AGIPD) developed for the European XFEL by a collaboration between Deutsches Elektronen-Synchrotron (DESY), the Paul-Scherrer-Institute (PSI), the University of Hamburg, and the University of Bonn, led by Heinz Graafsma [4, 5]. The feasibility of combining adaptive gain with charge removal techniques to increase dynamic range in XFEL experiments is assessed by simulating XFEL scatter with a pulsed infrared laser. The strategy is incorporated into pixel prototypes which are evaluated with direct current injection to simulate very high incident x-ray flux.

A fully functional 16x16 pixel hybrid integrating x-ray detector featuring several different pixel architectures based on the prototypes was developed. This dissertation describes its operation and characterization. To extend dy-

dynamic range, charge is removed from the integration node of the front-end amplifier without interrupting integration. The number of times this process occurs is recorded by a digital counter in the pixel. The parameter limiting full well is thereby shifted from the size of an integration capacitor to the depth of a digital counter. The result is similar to that achieved by counting pixel array detectors, but the integrators presented here are designed to tolerate a sustained flux $>10^{11}$ x-rays/pixel/second. In addition, digitization of residual analog signals allows sensitivity for single x-rays or low flux signals. Pixel high flux linearity is evaluated by direct exposure to an unattenuated synchrotron source x-ray beam and flux measurements of more than 10^{10} 9.52 keV x-rays/pixel/s are made. Detector sensitivity to small signals is evaluated and dominant sources of error are identified. These new pixels boast multiple orders of magnitude improvement in maximum sustained flux over the MM-PAD, which is capable of measuring a sustained flux in excess of 10^8 x-rays/pixel/second while maintaining sensitivity to smaller signals, down to single x-rays.

BIOGRAPHICAL SKETCH

Joel Weiss was born in Orlando Florida in 1988. He grew up there with his parents, two brothers, and a dog named Buck. In 2007 he began college at the University of Florida majoring in physics. He graduated with a Bachelor of Science degree in 2011 and began graduate studies in physics at Cornell University later that year.

This document is dedicated to my family.

ACKNOWLEDGEMENTS

The work described in this dissertation would not have been possible without the help and guidance of the Gruner group's members and many others.

Sol Gruner's curiosity and general excitement for science and discovery is contagious. His ability to maintain a broad view while delving into details has been the foundation of the work described here, and his steady guidance over the last six years has shaped me as a scientist. Mark Tate's apparent mastery of every project in the Gruner group still boggles my mind, and his work ethic is unmatched. He's been a role model for me and effectively a second adviser. Talking through details with him is always enlightening.

Hugh Philipp has been a constant teacher to me and is a great person to work a synchrotron night shift with (especially if there are tricycles). His expertise has been essential to this work and I've learned a tremendous amount about circuit design through discussions with him. I've had the good fortune to work closely with Kate Shanks on a number of projects, including the work on uranium dioxide described in Chapter 3. She taught me all about x-ray detectors when I joined the group and brings an unparalleled level of organization to any project she touches. Her fastidiousness was essential to the completion of the HDR-PAD. I'm lucky to call her both a colleague and a friend.

Prafull Purohit has taught me a lot about FPGAs and computer technology while performing all of our FPGA programming. He's also demonstrated immense patience when inundated by my requests for FPGA modifications and feature additions. Darol Chamberlain provided invaluable knowledge and experience, and I learned a lot from him as well. He always went out of his way to help with circuit analysis or a soldering iron.

Martin Novak's expertise has been essential to this work as he built the ma-

jority of mechanical components. He always knows the best way to build whatever it is you need, including a dog trap. I feel fortunate to have shared an office with Jeney Wierman. She brings cheer everywhere she goes and makes positive impacts both inside and outside of work. Veronica Pillar has also been a great friend, and I'm glad to have learned circuits by working through Horwitz and Hill with her.

The work described in Chapter 3 was conducted in collaboration with scientists from Idaho National Lab including Krzysztof Gofryk and Daniel Antonio. Developing the experiment on uranium dioxide with them was exciting and I learned a great deal. Jacob Ruff was the initial driving force in this experiment, and helped me to perform the final test of the HDR-PAD described in Chapter 7. I admire his straightforward approach to problems and depth of knowledge. The work at the APS would not have been possible without Zahir Islam. I've thoroughly enjoyed working closely with him during my trips to Illinois, and I've learned a tremendous amount from him, the least of which includes the best places to eat in Lemont. He's been a great teacher and mentor.

The work described in Chapter 4 was performed with Julian Becker, who helped me design the laser system before he had even arrived in our group as a postdoctoral researcher. I've learned a lot from him as well. I want to thank Professors Veit Elser and Alyssa Apsel for serving on my committee and for their guidance throughout my work at Cornell. The foundation of my analog integrated circuit experience comes from Professor Apsel through her course on the topic.

My interest in physics was fostered in high school by my exceptional physics teacher Angela Cortez who I am lucky to have learned from. Professor Stephen Hagen introduced me to research while at the University of Florida. Though the

particulars of my work have changed, he gave me the foundational skills and understanding that I've used in research ever since.

My parents have always been supportive and their hard work is a constant inspiration. The family they've built is a foundation on which I try to build, and any good I can do is thanks to them. Likewise my brothers Josh and Micah are both individuals that I look up to and admire. They set examples for me to follow as they forge their unique paths. Micah, Josh, and Sarah are each supportive in their own right and live with principals that I strive to emulate. Alex's support has been invaluable and has helped me through the toughest stretches of graduate school.

I've had the pleasure to work with many other collaborators that I have not named here, but to everyone, thank you. This research was supported by the U.S. National Science Foundation and the U.S. National Institutes of Health/National Institute of General Medical Sciences via NSF award DMR-1332208, U.S. Department of Energy Award DE-FG02-10ER46693 and DE-SC0016035, and the W. M. Keck Foundation. This work is based in part upon research conducted at the Cornell High Energy Synchrotron Source (CHESS) which is supported by the National Science Foundation under award DMR-1332208. This research used resources of the Advanced Photon Source, a U.S. Department of Energy (DOE) Office of Science User Facility operated for the DOE Office of Science by Argonne National Laboratory under Contract No. DE-AC02-06CH11357.

TABLE OF CONTENTS

Biographical Sketch	iii
Dedication	iv
Acknowledgements	v
Table of Contents	viii
List of Tables	xi
List of Figures	xii
1 Introduction	1
1.1 X-ray diffraction	1
1.2 Experimental requirements	6
1.2.1 Light sources	7
1.2.2 X-ray detectors	12
1.3 Summary and document organization	18
2 Hybrid pixel array detectors	20
2.1 Introduction	20
2.1.1 PAD overview	20
2.2 Semiconductor physics	22
2.2.1 Energy bands	22
2.2.2 Doping semiconductors	25
2.2.3 P-n junctions	28
2.2.4 Radiation in a reverse biased diode	29
2.2.5 CMOS	31
2.2.6 Radiation hardened components	36
2.3 Pixel array detectors	40
2.3.1 Integrating detectors	41
2.3.2 Amplifier noise in feedback	45
2.3.3 Electronic noise	46
2.3.4 Counting detectors	49
2.3.5 Comparing integrating pixels and counting pixels	50
2.4 Integrating PAD state-of-the-art	54
2.4.1 The Mixed Mode Pixel Array Detector (MM-PAD)	56
2.4.2 The Adaptive Gain Integrating Pixel Detector (AGIPD)	59
3 Application of detectors	62
3.1 Introduction	62
3.2 Uranium dioxide background	62
3.3 Experimental design	64
3.3.1 Pulsed magnet	65
3.3.2 Uranium measurements	66
3.3.3 Azimuthal calibration	70
3.4 Data analysis	74

3.4.1	Future work	77
3.5	Necessity of high dynamic range	77
4	The high dynamic range detector concept	80
4.1	Measuring the plasma effect	81
4.1.1	Experimental apparatus	83
4.1.2	Transient current analysis	88
4.1.3	Conclusions	94
4.2	Adaptive gain and charge removal combined	95
5	Pixel substructure testing	97
5.1	Pixel architectures	98
5.1.1	MM-PAD 2.0	99
5.1.2	Charge dump oscillator	102
5.1.3	Capacitor flipping pixel	105
5.2	Integrating amplifier	108
5.2.1	Flipped voltage follower	110
5.2.2	Local common mode feedback	112
5.2.3	Amplifier output	114
5.2.4	Noise properties	116
5.2.5	Pole splitting	116
5.3	Current injection tests	119
5.3.1	Probe pad current injection	120
5.3.2	Performance and analysis	122
5.4	Summary	126
6	The high dynamic range pixel array detector	127
6.1	Introduction	127
6.2	System overview	127
6.3	HDR-PAD ASIC	131
6.3.1	Pixel overview	132
6.3.2	Data readout	134
6.3.3	Adaptive gain implementation	140
6.3.4	Programmable test sources	141
6.3.5	Radiation hardening	142
7	HDR-PAD Characterization	147
7.1	Introduction	147
7.1.1	Dark current integration	148
7.1.2	Photon histograms	151
7.1.3	High flux measurements	155
7.2	Small signal resolution	163
7.2.1	Global noise sources	164
7.2.2	Local noise	169

8	Conclusions	173
A	Laser pulse measurement schematics	177

LIST OF TABLES

4.1	Table listing some x-ray energies, their attenuation length in silicon, and the IR wavelength with a matching attenuation length in room temperature silicon. X-ray attenuation lengths were drawn from the NIST database [64], and IR photon attenuation lengths were drawn from [65].	82
5.1	Pixel Average Power Consumption From Simulation	125
6.1	Pixel front-end specifications	134
7.1	Parameters extracted from photon histograms	155
7.2	Power supply variability	168
7.3	Pixel noise in reset	169
7.4	Pixel noise in low gain	170

LIST OF FIGURES

1.1	Two scattering bodies separated by \vec{d} . Radiation is incident with wave vector \vec{k} and radiation is scattered with wave vector \vec{k}' . The path length difference between light scattering from one point versus the other is $\vec{d} \cdot (\hat{n} - \hat{n}')$	2
1.2	LEFT: a bending magnet steers an electron beam and produces radiation throughout the curved motion. MIDDLE: A wiggler induces sinusoidal motion in an electron beam and produces a cone of radiation which sweeps from side to side. RIGHT: An undulator induces sinusoidal motion in an electron beam and produces a cone of radiation which maintains an overlapping portion while sweeping from side to side. Figure adapted from [15].	8
1.3	Schematic of SASE FEL insertion device. Long undulators are used such that light produced by the mild sinusoidal motion of electrons at the start of the beam segment modulate the spatial density of electrons further along. The resultant electron bunching causes electrons to amplify the radiation coherently. Adapted from [13].	11
1.4	Percent of x-rays absorbed in 500 μ m silicon at normal incidence. Attenuation length data from [23].	16
2.1	A cartoon schematic of a hybrid pixel array detector. The CMOS electronics layer is a lattice of pixel-circuits which measure signals coming from the diode detection layer. The diode detection layer converts incident radiation into an electronic signal. The bump bonds connect the diode detection layer and CMOS electronics layer on a per-pixel basis, transferring electronic signals from the region of the detection layer in which radiation was absorbed to the nearest pixels. The image is adapted from [28] and is not to scale.	21
2.2	(a) Allowed energies of an electron in a one dimensional sinusoidal potential with periodicity a . When the wave vector is equal to an integer multiple of reciprocal lattice vectors, two solutions to the Schrodinger equation exist corresponding to standing waves with peaks on or between the potential peaks. (b) The allowed energies wrapped back and depicted as bands in the "reduced zone scheme." Image adapted from [33].	24

2.3	Cartoon depiction of electron pairing in a silicon crystal. Note that the diamond structure of the lattice is not represented here. Only valence electrons are drawn. (a) Silicon atom in perfect lattice. Four valence electrons make covalent bonds with all nearest neighboring atoms. (b) One boron atom replaces a silicon atom. A hole is present because the boron has only three valence electrons and cannot bond with all four nearest neighbors. (c) One phosphorus atom replaces a silicon atom. Four of the five phosphorus valence electrons engage in covalent bonding. The fifth valence electron occupies a state in the conduction band.	27
2.4	Cartoon depiction of radiation being absorbed in a reverse biased diode. The image is not to scale. The clouds of charge carriers formed are offset in this image for clarity. The aluminum contact on the sensor is labeled. Image adapted from [36].	31
2.5	N-type MOSFET transistor cross-section. The four transistor terminals are the source, drain, gate, and substrate. Width and length (W and L respectively) describe the dimensions of the conductive channel formed beneath the gate when inverted. Image adapted from [37] with alterations.	32
2.6	Photo of the CS-PAD hybridized ASIC wirebonded to support electronics. The wirebonds send biases and control signals to the ASIC, and also transmit readout signals from pixels to support electronics for processing and recording. The silicon sensor layer is about 20mm wide. (photograph by Mark W. Tate)	41
2.7	MM-PAD ASIC bump bonds. The ASIC contains a 128x128 array of solder bumps, one connected to each pixel, which can be bonded to a sensor with suitable backside metalization. Pixel pitch is 150 μ m.	42
2.8	Basic integrating pixel schematic. The diode represents a connection to the photodiode sensor. The amplifier collects charge incident from the photodiode onto C_f . C_d is not a real capacitor, but represents the parasitic capacitance on the front end of the pixel. V_{out} is the pixel output, typically digitized outside of the pixel through an analog transmission chain (not shown).	43
2.9	Basic counting pixel schematic. The diode represents a connection to the photodiode sensor. C_d is not a real capacitor, but represents the parasitic capacitance on the front end of the pixel. The pulse shaper outputs a pulse for incident photocurrent spikes. The comparator determines whether the pulse height indicates that an x-ray was absorbed in the sensor. When the comparator fires, the counter is incremented. The total digital counts in a given period are readout off chip (read out chain not shown). . .	49

2.10	Illustration of pulse pileup in a photon counting detector. The true and observed pulses line depicts the "true" pulses that would result from each photon event individually on top of the "observed" pulses that the pulse shaper outputs. The detector's state line illustrates the window in which the comparator will read only one photon, while the events on detector line is the actual timing of photon events. With five photons incident on the pixel, only three are counted. Image adapted from [48].	52
2.11	Measured counts per second (cps) of incident x-rays on a PILATUS photon counting pixel versus the actual flux at the European Synchrotron Radiation Facility (ESRF). Here we see the impact of synchrotron pulse structure on the count rate limitations of photon counting detectors. Regardless of average flux, the instantaneous flux measurable by a counting pixel is limited. Observed count rate varies with synchrotron mode. The plot is adapted from [49].	54
2.12	Measured count rate of incident 10 keV x-rays on a PILATUS3 photon counting pixel versus the actual flux. Severe count rate non-linearity occurs above 10^6 counts per second without re-triggering. Implementation of re-triggering improves estimation of count rate to some extent, but is still inherently limited. The plot is adapted from [50].	55
2.13	Simplified MM-PAD schematic. The switched capacitor for charge removal is enclosed in the dotted box. The diode in the schematic represents a connection to the detector sensor, a reverse-biased diode.	57
2.14	(a) Analog output signals as a function of exposure time while integrating a constant source. The output forms a sawtooth wave, dropping each time a charge removal cycle is executed. (b) Number of charge removal cycles executed versus exposure time. Data corresponds to the measurements in (a). (c) Analog output signals merged with digital output yielding total integrated signal versus exposure time. The red line in each plot is a fit to illustrate linearity. Plots adapted from [54].	58
2.15	Block level AGIPD schematic taken from [5]. Capacitors $C_{f,mid}$ and $C_{f,low}$ begin with switches open. If the integrator output voltage crosses V_{ref} the switch connecting $C_{f,mid}$ is closed. If V_{ref} is crossed again, $C_{f,low}$ is connected. The storage cell matrix after the CDS stage is an array of in-pixel storage cells for burst framing.	59
2.16	Transfer characteristics of the AGIPD detector pixels. The three regions plotted represent the three gain settings of the AGIPD. The gain setting at readout is dependent on incident signal. The dynamic range spans four orders of magnitude at 12.4 keV. Plot adapted from [5].	61

3.1	The sample is mounted in the magnet and diffraction is collected by the detector in back-scatter geometry. Note that the sample does not rotate independently from the magnet.	67
3.2	Sample θ measures the rotation of the sample relative to the incident beam. 2θ measures the angle of diffraction relative to the transmitted beam.	68
3.3	Detector pixels are mapped horizontally to diffraction angles (2θ). Detector pixels are summed in the vertical direction (χ) to create the $\theta - 2\theta$ plots referred to throughout this chapter. Due to sample orientation, diffraction primarily occurs in the y-x plane.	68
3.4	Uranium dioxide $\theta - 2\theta$ plot measured at zero field and 14 K. The vertical lines in the intensity are artifacts resulting from gaps between the MM-PAD detector modules. This plot serves as a baseline for comparison of diffraction from the sample with magnetic fields applied.	69
3.5	Sample frame of uranium dioxide diffraction peak $\langle 888 \rangle$ at room temperature. The color scale is logarithmic and the exposure time was 10 ms. The peak flux is close to the maximum measurable by the MM-PAD. Gaps between the modules of the MM-PAD are also visible.	70
3.6	Pulsed magnetic field as measured by the Hall current monitor, based on the known inductance of the solenoid. To illustrate magnetic field sampling, MM-PAD exposures are highlighted. Each exposure time was $140\mu\text{s}$	71
3.7	Pixel to 2θ calibration geometry. Diffraction from a silicon monochromator is measured with two different x-ray energies and fixed detector position. This allows calculation of the azimuthal angular position of each pixel on the detector surface.	73
3.8	A selection of $\theta - 2\theta$ plots of uranium dioxide as a function of magnetic field. Each plot is composed of a separate frame for each sample θ value. Values of 2θ correspond to pixels on the MM-PAD. This depiction illustrates the behavior of electron density in reciprocal space as a function of magnetic field.	75
3.9	Integrated intensity along reciprocal lattice vector $\langle hhh \rangle$ as a function of magnetic field. At zero field a single diffraction peak is seen. The peak shifts as field increases, and a weaker peak diverges from the primary diffraction above 5 T. The plot is formed by dividing $\theta - 2\theta$ plots along the line $\theta = \theta$ into bins perpendicular to this line, spanning the entire dataset. The top and bottom images are the same data. The top plot has a linear scale and the bottom plot has a log scale.	76

4.1	Attenuation length in silicon of x-rays (left) matches attenuation length in silicon of IR photons (right). The green line highlights the correspondence of 12 keV photons to 1016 nm photons. In this way, IR laser pulses can simulate XFEL pulses.	82
4.2	Simulated hole density created in one micron slices of a silicon sensor as a function of depth into the sensor for a laser pulse of 1016 nm wavelength photons with various spectral distributions at normal incidence. The laser pulse was simulated with 6 μm pulse radius and 10^{11} eV pulse energy at room temperature.	84
4.3	Laser beam path for transient current technique studies. The pulsed infrared laser is controlled by a computer (not shown) which coordinates the oscilloscope readings. Laser pulses pass through a beam sampler which consists of an 1% silvered mirror at 45 degrees to the beam path. A dedicated diode reads the fractional pulse to record pulse-to-pulse energy variations. The main pulse then passes through a filter wheel which enables large scale pulse intensity variation. The pulse is subsequently expanded through a Galilean telescope to permit tighter focus by the achromatic doublet lens. The focused pulse is absorbed by a custom silicon photo diode and the photocurrent transient is routed to the oscilloscope through a custom PCB. The main pulse transient and split pulse transient are read by the oscilloscope to the data acquisition computer.	86
4.4	Gaussian fit to derivative of lateral translation scan of target diode with 950nm laser incident. The fitted line describes the laser pulse profile in one dimension perpendicular to the beam path.	90
4.5	Characteristic shape of photocurrent transients produced by high intensity pulses ($> 10^4$ x-rays). The transient above is an average of one hundred 950 nm pulses (equivalent to 8 keV attenuation length) with a mean single pulse energy equivalent to 10^6 8 keV x-rays. The sensor was bias was 200 V.	90
4.6	Normalized integrated charge versus integration time of 1016 nm (12 keV equivalent attenuation length) pulses at three pulse energies. The red dotted line is a low energy pulse ($< 10^3$ x-rays, simulated from previous work [66]) for reference. Sensor bias was 200 V.	92
4.7	Average pulse duration as a function of total pulse energy at three wavelengths. Pulse durations were measured as time above two times the standard deviation of background noise. Sensor bias was 200 V.	92
4.8	Averaged photocurrent traces from 950nm laser pulses focused to 6 μm incident on a 500 μm thick silicon diode. The diode bias was 200 V.	93

5.1	Simplified MM-PAD 2.0 schematic. Control logic box engages adaptive gain prior to enabling switched capacitor charge removal.	100
5.2	MM-PAD 2.0 gated oscillator and charge removal switched capacitor block level schematics.	101
5.3	Simplified CDO schematic. The ring oscillator charge removal circuitry is enclosed in the dashed box. Selectable gain was replaced with an adaptive gain scheme in a subsequent fabrication.	103
5.4	Simplified capacitor flipping pixel schematic. Dynamic thresholding circuitry is enclosed in the dotted box. An adaptive gain scheme was implemented in the most recent fabrication.	106
5.5	Class AB amplifier topology utilized in pixel prototypes. Architecture adapted from [70].	110
5.6	Example of negative feedback.	116
5.7	Inferred input currents based on pixel outputs versus actual input current. The dotted line represents an ideal response (inferred input equals actual input). The charge dump oscillator is plotted with circles, the MM-PAD 2.0 with triangles, the externally thresholded capacitor flipping pixel with diamonds, and the dynamically thresholded capacitor flipping pixel with squares. Input and inferred current values are converted to the number of 8 keV x-rays absorbed in silicon per second which would produce an equivalent photocurrent. Inset: Magnification of the same data.	121
5.8	Measured comparator delays from the capacitor flipping pixel with dynamic thresholding are plotted. Measured values assume that all deviations from linearity in the capacitor flipping pixel's output are a result of charge integrated during switching delays. Values from simulation are plotted as a dotted line. . . .	123
6.1	Photograph of the high dynamic range pixel array detector (HDR-PAD) unit with FPGA, vacuum enclosure, and PCB support electronics shown. Not shown are power supply units, controlling computer, vacuum, water chiller, and thermoelectric controller. The vacuum housing is roughly four inches along each edge.	128
6.2	LEFT: ZIF socket on the support electronics PCB with thermally regulated cold finger protruding. The PCB metalization which is sandwiched by the clam shell assembly is visible. RIGHT: Hybridized module wire bonded to a ceramic pin grid array (PGA) package, seated in the ZIF socket. The cold finger makes contact with the backside of the packaging.	129

6.3	Close up image of a HDR-PAD hybrid module wire bonded to the PGA package. A single wire bond connects to the top surface of the sensor layer to supply the reverse biasing voltage. The wire bond is made to a thicker aluminization which is visible along the edge of the sensor.	131
6.4	Simplified MM-LDO schematic. The pixel is identical to the MM-PAD 2.0, but rather than an externally supplied V_{low} , the voltage is maintained by a low dropout regulator circuit. The level of this voltage is set relative to the front end.	133
6.5	Simplified ASIC analog readout chain schematic. Sample and hold circuits in each pixel connect to a column bus through a switch. A row select signal closes this switch and connects all sample and hold circuits in a given row to the column bus. A buffer at the edge of the column bus feeds a multiplexer. A column select signal drives the multiplexer to connect each column buffer to an edge buffer in sequence. The edge buffer sends analog signals off-ship for digitization. Each bank possesses its own copy of the depicted circuitry.	138
6.6	Schematic of an enclosed layout transistor (ELT) with source, gate, and drain terminal connections labeled. Additional dimensions are required to parametrize the transistor. Rather than simply a length and a width, two lengths and two widths are required, labeled as L_1 , L_2 , a , and b where L 's are lengths.	143
6.7	Dummy switch compensation schematic. The active switch is flanked by two half-sized switches. The half sized switches are shorted so that they do not control any connections between nodes. They are driven by the complement of the active switching signal which results in opposite charge injection of the active switch. If the charge injected by the active switch is split evenly between the nodes it connects, the net charge injection of each node should be zero.	145
7.1	Average MM-PAD 2.0 pixel output as a function of exposure time. The pixel input is sensor dark current, which is relatively constant, so exposure time corresponds linearly to total integrated signal. Basic operation of the pixel is evident. Positive charge accumulates on the integration node, causing the integrator output to decrease in voltage. Once $V_{out} = V_{th}$ (roughly 4800 ADU) the adaptive gain is triggered (at 50ms), and the pixel continues to integrate. When $V_{out} = V_{th}$ again, charge removal occurs (first at 650ms).	149

7.2	Cartoon depiction of pinhole mask alignment. Pin holes are smaller than pixels and spaced more than one pixel width apart. Aligning the pinholes over the center of pixels ensures that the signal from each photon absorbed by a pixel is not shared with neighboring pixels.	152
7.3	Histogram of 25,000 analog outputs from an MM-LDO pixel with low flux silver $k\alpha$ radiation. Exposure time was 1 ms. The histogram is fit by a sum of five Gaussian functions. Parameters from the fit describe the pixel's gain and noise characteristics. Peaks corresponding to integer numbers of photons absorbed by the pixel in the integration window are labeled.	153
7.4	Photon histograms of MM-LDO pixels with progressively higher flux. Photon peaks are fit from zero photons up to twenty-one photons. A final peak was added where a twenty-second peak would sit. This signal level triggers the adaptive gain circuitry and brings the pixel integrator output away from the threshold voltage.	156
7.5	CHESS A2 beamline schematic. Beam enters the hutch through beam defining slits and enters the first ion chamber (IC1) which measures the full beam flux. A variable attenuator rotates to place aluminum of various thicknesses in the path of the beam. A second ion chamber (IC2) measures the attenuated flux. The attenuated beam strikes the HDR-PAD directly.	158
7.6	Sample image with 1 ms exposure to the full A2 beam. The scale is logarithmic.	158
7.7	Signal measured by the MM-PAD 2.0 pixel with a total integration capacitance of 880 fF versus the signal measured by ion chambers. The dashed line represents perfect performance for comparison.	159
7.8	Signal measured by the MM-PAD 2.0 pixel with a total integration capacitance of 2630 fF versus the signal measured by ion chambers. The dashed line represents perfect performance for comparison.	160
7.9	Signal measured by the capacitor flipping pixel with an externally supplied threshold voltage versus the signal measured by ion chambers. The dashed line represents perfect performance for comparison.	161
7.10	Signal measured by the capacitor flipping pixel with dynamic thresholding enabled versus the signal measured by ion chambers. The dashed line represents perfect performance for comparison.	162
7.11	Signal measured by the MM-LDO pixel versus the signal measured by ion chambers. The dashed line represents perfect performance for comparison.	162

7.12	Pixel bank average versus pixel bank average. Each point represents one frame. Bank averages from within the same frame are compared. Correlation coefficient is computed.	164
7.13	The standard deviation of N pixels averaged together is plotted as a blue dotted line. The average standard deviation of N pixels divided by N is plotted as an orange dashed line. If there were no global noise, the standard deviation of the average value of many pixels would approach zero as N increases.	166
A.1	Layout of sample PCB used in pulsed infrared laser studies discussed in Chapter 4. The circle labeled HV on the right side of the board is punched through to permit laser pulses to strike the diode, which is connected to the ring which supplies the bias voltage. Immediately to the left of this ring are wire bonding pads which are connected directly to pixels on the diode. Signals are routed through a connector to the circuitry for which schematics are provided on subsequent pages.	177

CHAPTER 1

INTRODUCTION

X-rays are used to obtain structural information about samples on the atomic scale. This experimental probe finds applications in fields from material science to biology and everything in-between. Each experiment requires an x-ray light source and a sample, but they also require a suitable x-ray detector or means of measuring the experimental output. New x-ray light sources require new x-ray detectors with commensurate capabilities. This thesis outlines the development of such a detector suitable for use at new, high brightness x-ray sources. By extending the measurable dynamic range, light sources can be utilized to their full potential.

1.1 X-ray diffraction

To probe matter on the atomic scale, we need photons with wavelengths of the appropriate size. Visible photons have wavelengths that are several hundreds of nanometers. These photons interact with a large number of atoms simultaneously when they strike an object because atomic spacing in matter is on the order of angstroms, 10^{-10}m . This corresponds to a photon energy of $\frac{hc}{\lambda} = 12.4\text{keV}$, which is the realm of x-rays. To understand how x-rays interact with matter, we will base our discussion on the derivation of the Von Laue formulation of x-ray diffraction in Solid State Physics by Ashcroft and Mermin [6]. To simplify the discussion, we will assume that the scattering of photons from matter is elastic, meaning that no energy is lost in the scattering process, and thus the wavelength of scattered light is the same as the wavelength of incident

light.

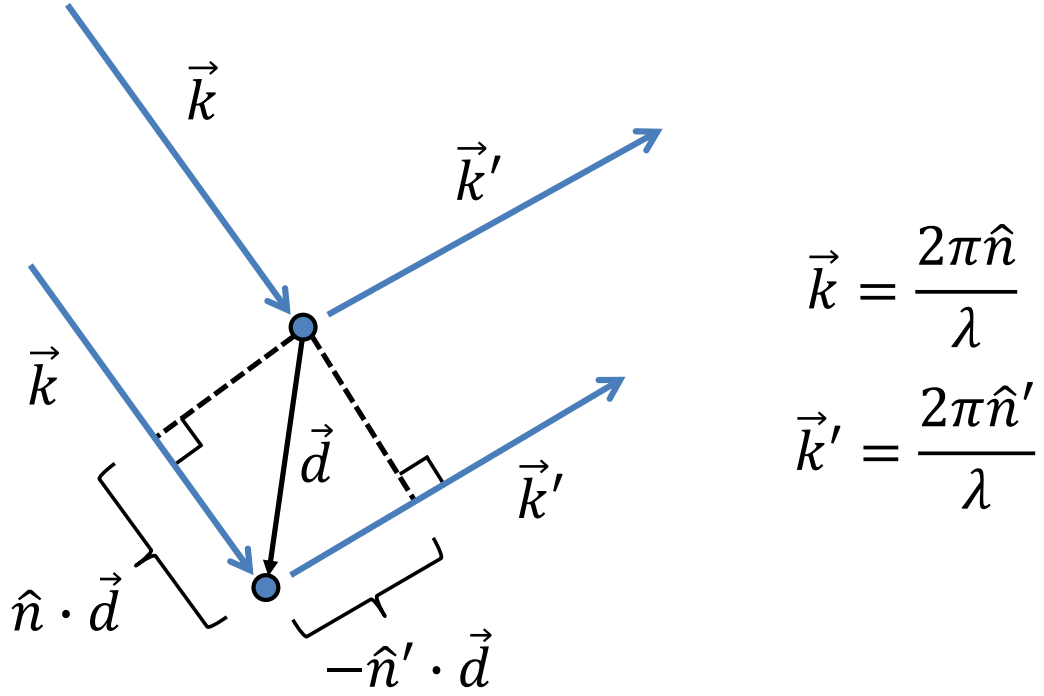


Figure 1.1: Two scattering bodies separated by \vec{d} . Radiation is incident with wave vector \vec{k} and radiation is scattered with wave vector \vec{k}' . The path length difference between light scattering from one point versus the other is $\vec{d} \cdot (\hat{n} - \hat{n}')$.

Consider two small scattering bodies separated by a vector \vec{d} as depicted in Figure 1.1. Assume that light arrives at the bodies from very far away so that the incident wave vector of each photon is parallel. The wave vector is defined as $\vec{k} \equiv \frac{2\pi\hat{n}}{\lambda}$ where \hat{n} is the unit vector parallel to \vec{k} . Consider scattered photons with wave vector $\vec{k}' \equiv \frac{2\pi\hat{n}'}{\lambda}$. To interfere constructively, the difference in length between the two paths must be an integer multiple of the light's wavelength:

$$\vec{d} \cdot \hat{n} - \vec{d} \cdot \hat{n}' = \vec{d} \cdot (\hat{n} - \hat{n}') = m\lambda \quad (1.1)$$

where m is an integer. Multiplying both sides of the equation above by $\frac{2\pi}{\lambda}$ yields

$$\vec{d} \cdot (\vec{k} - \vec{k}') = 2\pi m. \quad (1.2)$$

Now applying Euler's formula,

$$e^{ix} = \cos(x) + i \sin(x), \quad (1.3)$$

we find that

$$\left| e^{i(\vec{k}-\vec{k}')\cdot\vec{d}} \right| = \left| e^{i2\pi m} \right| = |\cos(2\pi m) + i \sin(2\pi m)| = 1. \quad (1.4)$$

Finally, we can define \vec{K} to be the change in wave vector of the scattered light:

$$\left| e^{-i\vec{K}\cdot\vec{d}} \right| = 1. \quad (1.5)$$

To reiterate, the equations above specify, in general terms, the spatial relation required for two bodies to scatter light that will interfere purely constructively. From this calculation we can in theory perform a simple experiment to measure the distance between two atoms, given that we scatter monochromatic light from them and measure the angle at which the scattered light interferes constructively. Of course we would often like to image matter that is composed of more than two atoms.

Interestingly, Equation 1.5 is precisely the definition of the reciprocal lattice for a Bravais lattice with points at \vec{d} . Many sources exist for a rigorous discussion of Bravais lattices and crystals in general (for example see [6, 7]). Here we will outline the concept briefly.

A given Bravais lattice is defined by its basis vectors. In three dimensions a set of Bravais basis vectors may be any three vectors which do not lie in the same plane, and the corresponding Bravais lattice is the collection of all points of the form $\vec{d} = m_1\vec{a}_1 + m_2\vec{a}_2 + m_3\vec{a}_3$ where m_1 , m_2 , and m_3 are integers and \vec{a}_1 , \vec{a}_2 , and \vec{a}_3 are the basis vectors [6]. Bravais lattices are used to describe crystalline materials, materials in which all of the constituent atoms are arranged

periodically. The magnitudes of a Bravais lattice's reciprocal lattice vectors are inversely proportional to atomic spacing and their direction is perpendicular to atomic planes. Specifically, for lattice vectors \vec{a}_1 , \vec{a}_2 , and \vec{a}_3 , the reciprocal lattice vectors are

$$\vec{b}_1 = 2\pi \frac{\vec{a}_2 \times \vec{a}_3}{\vec{a}_1 \cdot (\vec{a}_2 \times \vec{a}_3)}, \quad (1.6)$$

$$\vec{b}_2 = 2\pi \frac{\vec{a}_3 \times \vec{a}_1}{\vec{a}_1 \cdot (\vec{a}_2 \times \vec{a}_3)}, \quad (1.7)$$

and

$$\vec{b}_3 = 2\pi \frac{\vec{a}_1 \times \vec{a}_2}{\vec{a}_1 \cdot (\vec{a}_2 \times \vec{a}_3)}. \quad (1.8)$$

In the case of crystalline materials, equation 1.5 leads to the conclusion that for constructive interference, the change in the incident wave vector must be a linear combination of reciprocal lattice vectors. In this context, Equation 1.5 is equivalent to the familiar Bragg condition,

$$2d \sin \theta = m\lambda, \quad (1.9)$$

where d is the spacing between atomic planes, m is a positive integer, θ is the angle of incidence relative to the atomic planes, and λ is the wavelength. The derivation above does not assume specular reflection or a particular arrangement of atoms. The mathematical formalism gives us a rigorous framework to understand diffraction due to elastic scattering. In a more intuitive sense however, we find that atomic spacing can be measured by the angle at which x-rays scatter constructively from a sample.

The work above can be used to understand scattering from non-periodic arrangements of atoms as well. Note that Equation 1.2 specifies the condition

for purely constructive interference. More generally, $e^{-i\vec{k}\cdot\vec{d}}$ is the difference in phase factors between photons scattered at the origin and photons scattered at \vec{d} [7]. Suppose we define some function $\rho(\vec{d})$ to be the electron density of an object at all points in space. Assume that the amplitude of a wave scattered from a volume element dV is proportional to the electron density of the volume element. The amplitude of electric and magnetic fields for radiation scattered in the direction \vec{k}' will be proportional to the integral over all space of the electron density function multiplied by the term describing the phase relationship [7]. Specifically, the scattering amplitude, F , is

$$F = \int_{\vec{R}} e^{-i\vec{k}\cdot\vec{d}} \rho(\vec{d}) dV. \quad (1.10)$$

Note that equation 1.10 is the Fourier transform of the spatial distribution of the electron density. In this light, scatter from a periodic arrangement of atoms is a special case in which the spatial frequency of electron density is dominated by a discrete set of frequencies, thus sharp peaks are observed in x-ray diffraction from crystals. However, diffraction is measurable from any scattering body. Note that the situation is more complicated when the energy of incident radiation is close to the energy of an electron transition in the diffracting atoms. This leads to so called resonant scattering which involves results of the incident x-rays altering the distribution of electrons in the sample. For more information on this phenomena see sources such as [8, 9].

Of course, diffraction is not the only useful measurement that can be performed with x-rays. Radiography relies on the transmission of x-rays to gain information about density variations in the material being imaged. More dense materials absorb or scatter more x-rays, and so regions of a sample which transmit a larger fraction of incident x-rays are less dense. This is the general tech-

nique employed in most medical x-ray imaging. Fluorescence can be utilized to map the elemental constituents of a sample. X-rays of the correct energy excite inner-shell electrons in atoms to outer shells or ionize the atoms completely. When an electron subsequently drops in energy to fill the now under-filled orbital, light is emitted with energy equal to the change. This results in characteristic energies for each element, and by exciting the atoms of a sample and measuring the resultant fluorescence, the atomic constituents of the sample can be uncovered. Many more techniques utilizing x-rays to make useful measurements exist, but this dissertation work focuses primarily on diffraction experiments.

1.2 Experimental requirements

With an experimental probe for atomic scale information of a sample established in theory, we arrive at the question: what is required to perform these measurements in practice? The intricacies of experimental design and execution could fill volumes and vary drastically between each particular implementation. We'll settle here for a more basic treatment. To study a sample with x-ray diffraction requires a suitable x-ray source, a sample from which the x-rays will scatter, and a device with which to detect the scattered x-rays.

1.2.1 Light sources

X-ray tube sources

The most common x-ray source in a laboratory is an x-ray tube source. An overview of a tube source's operation is outlined below.

Electrons are emitted from a filament. The electrons are accelerated through a very high electric field created by a voltage difference between an anode and a cathode. Electrons then strike the anode. X-rays are generated primarily through two processes [10]. Bremsstrahlung radiation, or braking radiation, is the result of electrons decelerating in the anode material. The product is a broad spectrum of photons whose energies are limited by the voltage across which the electrons were accelerated. The second process involves the excitation of inner shell electrons in the anode material. Electrons are ejected from atoms in the anode, and when an electron drops in energy to take this now vacant set of quantum numbers, the change in energy is released as a photon. This results in distinct photon energy emissions that vary based on the anode material.

With an x-ray tube source, the primary limitation on maximum x-ray flux obtainable is the rate at which energy deposited in the anode as heat can be drawn away. Only about $\sim 0.2\%$ of the power, electron current multiplied by acceleration voltage, is actually converted to x-ray radiation [10]. To increase the maximum flux of tube sources, some sources employ a large, constantly moving anode that allows deposited heat to be distributed over a larger area. More recently, sources with a liquid metal anode have been implemented [11]. However, synchrotron radiation facilities dwarf tabletop x-ray production and will be discussed in the next section.

Synchrotron radiation facilities

Synchrotron radiation facilities have evolved significantly since their inception over 50 years ago [12]. A synchrotron is a particle accelerator in which charged particles are set to run in a closed path at relativistic speeds. Further acceleration of these charged particles produces radiation with specific characteristics. Precise control of this acceleration allows production of light with a variety of useful properties.

At present, over 50 synchrotron facilities are in operation worldwide, with 12 of these being so-called third generation sources [13]. Still more synchrotrons are under construction as the demand for beam time among scientists is far greater than its supply. Synchrotrons utilize bending magnets, wigglers, and undulators to produce intense, collimated x-ray beams [14]. Figure 1.2 is a cartoon depiction of radiation from these devices.

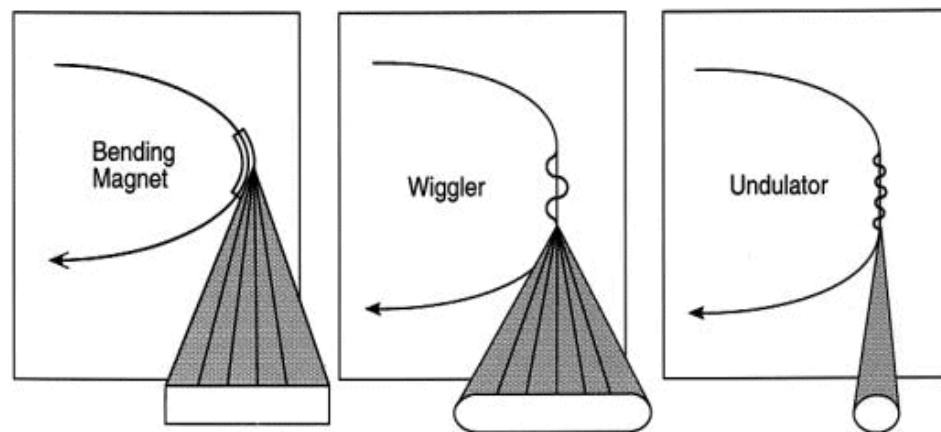


Figure 1.2: LEFT: a bending magnet steers an electron beam and produces radiation throughout the curved motion. MIDDLE: A wiggler induces sinusoidal motion in an electron beam and produces a cone of radiation which sweeps from side to side. RIGHT: An undulator induces sinusoidal motion in an electron beam and produces a cone of radiation which maintains an overlapping portion while sweeping from side to side. Figure adapted from [15].

Bending magnets are used to steer electron beams via the Lorentz force, but the acceleration that they cause also produces radiation. At synchrotrons, relativistic effects compress the emitted radiation into a cone with an opening angle in radians proportional to $\frac{1}{\gamma}$ where γ is the Lorentz factor [14]. Wigglers and undulators are used at synchrotrons, in addition to bending magnets, to generate radiation with useful properties. Wigglers are a series of bending magnets with alternating polarity which produce no net deflection of the electron beam. Undulators have the same magnetic structure as wigglers, but the deflection caused by their magnetic fields is small enough that the cone of radiation generated at each bend maintains an overlap in space. This causes interference of the radiation emitted at each turn which permits generation of highly coherent beams with sharp energy spectra [14].

In third generation light sources, light is typically emitted in pulses with tens of picoseconds duration and tens of nanoseconds gaps between pulses [12]. Shorter pulses are achievable through techniques such as electron bunch slicing at the cost of beam intensity. The energy of x-rays produced in modern sources is often tunable. The light produced is typically linearly polarized in the plane of acceleration. Some sources have tunable polarization as well.

An important metric in comparing light sources is brilliance. Brilliance is a property inherent to the light source and serves to compare sources both within and between synchrotron generations. The metric is defined as [16]

$$\frac{\#photons}{second * mrad^2 * mm^2 * 0.1\%BW} \tag{1.11}$$

The value begins with total x-ray flux, photons/second. The value is then

divided by a quantity with dimensions of area. This quantity is the source size. An ideal light source will have an infinitesimally small source size. Further, the quantity is divided by a term with units of mrad^2 . This quantity describes the divergence of a light source. Minimal divergence is desirable such that the light source is angularly collimated. Finally, the brilliance of a source includes information about its monochromaticity. The 0.1% BW term describes how much of the total flux falls within 0.1% of the desired bandwidth. Comparing a light bulb to a table-top laser, we find that while the light bulb may produce more photons in total, the laser may actually have a higher brilliance, as its light is more monochromatic and better collimated. Ultimately, all light sources must obey the diffraction limit which is related to the lateral coherence of the source [16]. The source's longitudinal coherence is related to its monochromaticity. The coherence of a light source is closely related to its brilliance [16]. Third generation sources presently reach average brilliances on the order of $10^{21} \frac{\text{photons}}{\text{second} \cdot \text{mrad}^2 \cdot \text{mm}^2 \cdot 0.1\% \text{BW}}$, and could theoretically be increased by 1-3 orders of magnitude.

X-ray free electron lasers

A new synchrotron technology further expands the possibilities of x-ray science by producing x-ray beams with some unprecedented characteristics. X-ray free electron lasers (XFELs), produce exceedingly brilliant x-ray beams by utilizing the interaction of light with the very electrons that produce synchrotron radiation [12]. The result is an x-ray beam consisting of extremely short, extremely brilliant x-ray pulses. Specifically, FELs internally modulate the density of the electron bunches used to generate synchrotron radiation. This density modula-

tion is achieved primarily through two strategies: seeding with an external laser and self amplified stimulated emission (SASE) [13].

In the seeding process, seed light supplied by an external laser travels along the electron flight path. As the electrons enter an undulator, the electric fields of the seed light compress electron bunches and spaces them according to the wavelength of the seed light [13]. The microbunching of electrons yields synchrotron pulses of very short duration with very high coherence. In SASE, the same process occurs, but rather than an external laser modulating the electron bunches, a suitably long undulator is used such that radiation produced at the start of the undulator has time to perform the desired spatial redistribution [13]. The result is analogous and is depicted in figure 1.3.

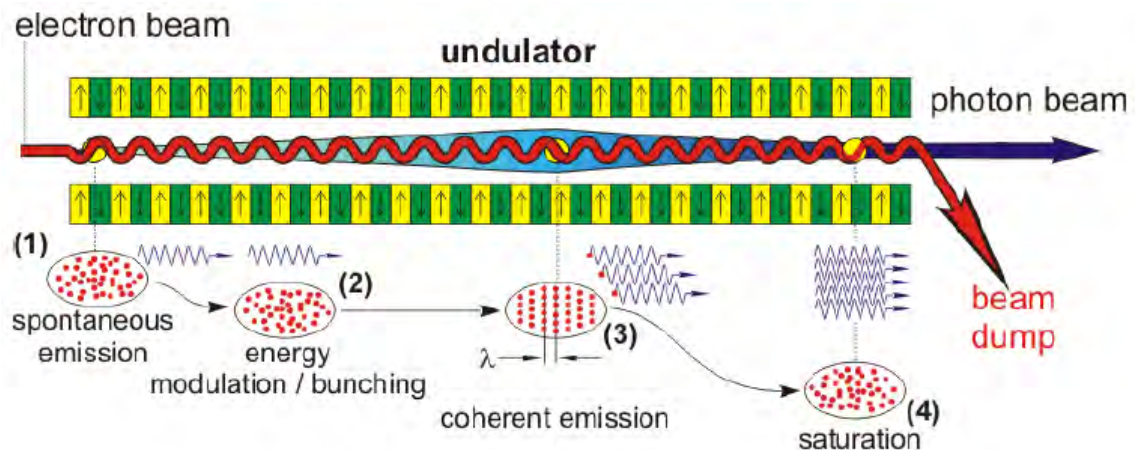


Figure 1.3: Schematic of SASE FEL insertion device. Long undulators are used such that light produced by the mild sinusoidal motion of electrons at the start of the beam segment modulate the spatial density of electrons further along. The resultant electron bunching causes electrons to amplify the radiation coherently. Adapted from [13].

X-ray pulses produced at XFELs are typically on the order of 10s of femtoseconds in duration. Energy resolution is typically $< 10^3 (\frac{E}{\Delta E})$ [17]. Pulses can be further monochromated, but this typically lengthens the pulse. Tuning

of XFEL radiation energy is possible, but at present the process is more time consuming than energy tuning at third generation sources. Pulse frequency is limited by electron gun properties, but is currently being pushed upwards of 10^4 pulses/second on average [17].

In addition to average brilliance, peak brilliance is used as a metric to describe XFELs. Typical peak brilliance values seen at XFELs which have been built or are being built reach upwards of $10^{33} \frac{\text{photons}}{\text{second} \cdot \text{mrad}^2 \cdot \text{mm}^2 \cdot 0.1\% \text{BW}}$. This tremendous increase in brilliance, along with drastically reduced pulse duration, will enable entirely new and exciting experiments.

1.2.2 X-ray detectors

There are numerous ways to detect and quantify an x-ray signal. This section aims to provide a brief overview of the dominant architectures with two dimensional spatial resolution. Specifically, point and strip detectors (zero dimensional and one dimensional detectors, respectively) will not be discussed, though they do find use in modern x-ray science. Area detectors all require some sensing medium, which absorbs incident radiation to be measured, and some means of quantifying the absorbed signal.

One distinction amongst x-ray detectors can be made with regard to the means by which they convert radiation to a measurable signal: direct and indirect. Indirect conversion x-ray detectors use a sensing medium to convert x-rays to an intermediate signal prior to conversion to the signal that is ultimately measured. A prime example of indirect conversion detectors is the phosphor-coupled charge coupled device.

Charge coupled devices, more commonly referred to as CCDs, find wide use in optical imaging both in consumer and scientific markets. CCDs consist of silicon doped in particular patterns such that light can be absorbed in the camera's pixels, and generated photo-charge is held in electric potential wells in the pixels in which the radiation was absorbed. At the end of an imaging period, a sequence of voltage changes can shuffle a column's charge to the edge of the sensor pixel-by-pixel to a readout amplifier which converts the integrated charge to a voltage. While direct detection CCDs designed for infrared light and x-rays have been constructed with thicknesses of hundreds of microns [18], the pixel volume in which light can be absorbed and measured efficiently in most CCDs is only a few microns [19]. The penetration depth of x-rays in silicon is much longer than that of visible light, so CCDs designed for use with visible light will only detect a small fraction of incident x-ray radiation. Most incident x-rays will pass through the sensitive volume without depositing a measurable signal. The absorption of photons in a semiconductor will be discussed further in Chapter 2. To increase the fraction of x-rays which can be detected by a CCD, the surface of the CCD can be coated with a scintillator or phosphor. Alternatively, the scintillator can be placed on a fiber optic bundle that couples the light to the CCD pixel array.

The phosphor absorbs x-rays and subsequently emits visible photons. These photons can then be imaged by the optical CCD with much greater efficiency. While CCDs can be manufactured with very low noise specifications, the phosphor intermediary introduces a number of undesirable effects in the data obtained. For example, the light emitted by the phosphor is emitted isotropically, so half of the signal is directed away from the imager. Additionally, the conversion efficiency of the phosphor is less than one, and thus the signal to noise ratio

of the data will be reduced relative to an efficient direct detection implementation [19]. Furthermore, the location at which the radiation struck the phosphor is more poorly defined, generally by a factor related to the thickness of the phosphor, as the emitted visible light undergoes a random walk through the phosphor prior to being detected by the CCD. These problems can be addressed to some extent, but are common to all indirect sensing detectors. Some other camera archetypes fall into the indirect detection category as well, including most monolithic active pixel sensors, which employ a scintillating layer in x-ray applications for the same reason as CCDs [20].

As noted above however, direct detection CCDs are used in x-ray science, and their development is ongoing [18, 21]. Film is also a direct detection technology, though its use has decreased as alternate means of quantifying x-ray signals have matured. The detector architecture focused on in this dissertation is the hybrid pixel array detector (PAD), also a direct detection technology. Hybrid PADs employ a dedicated sensing layer which electrically couples directly to pixels. Chapter 2 contains a detailed discussion of the technology.

There is no universally optimal detector. The particular requirements of an experiment will dictate which detectors are suitable. The following section briefly outlines some common measures which can be used to evaluate and compare detector performance.

Detector metrics

Various metrics exist for the comparison of x-ray detectors. Here we introduce several parameters which will be relevant in later sections. A broad measure of

a detector's limitations is the detective quantum efficiency (DQE) defined as

$$\text{DQE} = \frac{(S_o/N_o)^2}{(S_i/O_i)^2}. \quad (1.12)$$

S and N in Equation 1.12 refer to signal and noise respectively while the subscript o refers to the output and i refers to the input. This is a measure of the detector's impact on the signal-to-noise ratio [22]. For example, if the signal being measured is x-rays subject to Poisson statistics, the input noise is the square root of the number of incident x-rays. A DQE of 1 implies that the detector perfectly measures the input signal without introducing any additional noise or uncertainties. A real detector's DQE is always less than one. DQE can vary between individual measurements based on many parameters such as the magnitude of the input, the spatial distribution of the input, the energy of photons which constitute the input, and more, but DQE can be used to compare the performance of different detectors measuring the same signal. Factors which affect a detector's DQE can be examined independently.

As alluded to earlier, stopping power is the fraction of incident x-rays which deposit their energy in the detector's sensitive region. This is the metric which indirect detection methods improve with phosphor coatings. Direct detection methods also have a stopping power less than unity. Some fraction of incident x-rays will not be absorbed, even by an ideal sensor. Transmission at normal incidence of x-rays through a material of thickness d drops exponentially with thickness as

$$T = e^{-n\mu_a d} \quad (1.13)$$

where n is the number of atoms per unit volume in the material and μ_a is the atomic photoabsorption cross section [23]. As such, the absorption of x-rays in the material is one minus this quantity. Other factors such as absorption of sig-

nal x-rays in material coatings or other non-sensitive regions of a detector will further decrease the fraction of signal detected. Figure 1.4 plots the percent of incident x-rays absorbed by 500 μm thick silicon, a common x-ray sensor material, as a function of x-ray energy.

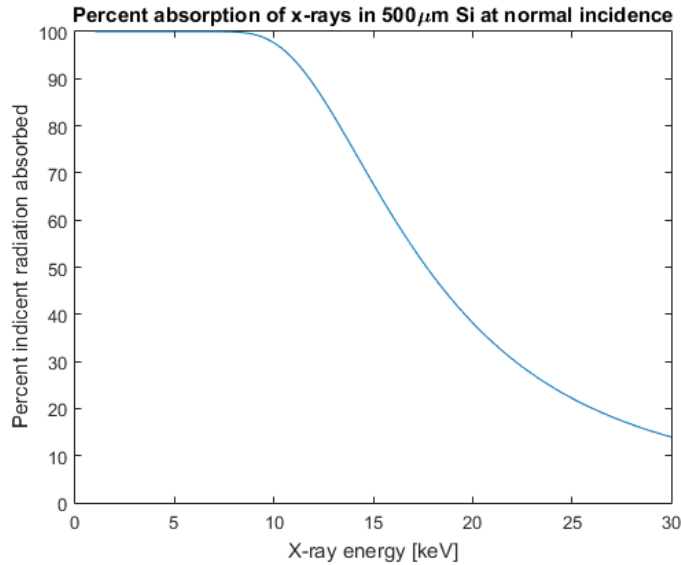


Figure 1.4: Percent of x-rays absorbed in 500 μm silicon at normal incidence. Attenuation length data from [23].

Given that some x-rays are absorbed in an area detector's sensitive volume, its spatial resolution can be quantified in several ways. A common measure is the point spread function (PSF) [22]. Given a point input, the PSF describes an imager's output. Mathematically, for an input I_{in} the imager's output, I_{out} , is the convolution of the input with the PSF:

$$I_{out} = I_{in} * \text{PSF} = \int_{\text{area}} I(\xi, \eta) \text{PSF}(x - \xi, y - \eta) d\xi d\eta \quad (1.14)$$

A related measure is the line spread function, an imager's response to a line of illumination, which is mathematically equivalent to a one dimensional integration of the PSF. Furthermore, the line spread function is related to the edge

spread function, an imager's response to a step function input. The line spread function is the derivative of the edge spread function [24].

The maximum signal that an imager can measure without saturation is the full well, usually specified on a per-pixel basis. The dynamic range of an imager describes the range of signal magnitudes which can be accurately measured. What this means exactly can vary between imagers and applications. Often dynamic range is reported as a pixel's full well divided by the read noise. For the purposes of this work, we will consider two definitions. One is the single pulse dynamic range. This is the range of signals measurable when the input arrives within a time frame that is much faster than the detector's response time. The second is the continuous signal dynamic range. This is the range of continuous signals which can be measured, generally expressed in units of x-rays per pixel per second. Each parameter is relevant in different scenarios.

To understand this metric, we must ask what it means for a signal to be measurable. In this work, the smallest signal of interest will be the signal from a single x-ray. To resolve this signal with very few false positive or false negative detections, one might require, for example, a signal to noise ratio of at least 5. This indicates that, in the absence of actual signal, a one x-ray signal will be seen due to noise less than once per one million measurements in a given pixel, assuming that pixel noise is Gaussian. Regarding the upper end of dynamic range, x-ray signals are subject to shot noise, owing to the discrete nature of photons. This means that measurements of photons are subject to Poisson statistics and the inherent uncertainty in the determination of the average number of photons which should arrive in a given time window is the square root of the number

of photons measured¹. When measuring a large signal, this uncertainty is unavoidable. Noise is also added to the measurement by the detector. Because these two noise sources are independent and uncorrelated they add in quadrature [25]. In this work we aim to keep the uncertainty in a measurement due to the detector smaller than the uncertainty due to Poisson statistics. Of course the fractional uncertainty of a signal goes to zero as the mean signal goes to infinity. Formally speaking, the upper end of dynamic range can be specified by when uncertainty in a measurement is dominated by detector systematics. Practically speaking, useful measurements can be made with uncertainties of a few tenths of a percent for large signals.

1.3 Summary and document organization

X-rays are a powerful probe of materials that can provide information about the organization and spacing of atoms in a sample. Obtaining this information requires a suitable x-ray source and x-ray detector. Synchrotron radiation facilities are a high brilliance source of x-rays. As synchrotron technology matures, the list of its useful scientific applications continues to grow, but hurdles still exist which prevent the full realization of these promising new techniques. Perhaps most prominent among these challenges is the detector problem. In essence, x-ray light source technology is out pacing x-ray detector technology. While x-ray free electron lasers enable a wide range of experiments in *theory*, their full real-

¹To understand this, imagine trying to measure the rate of cars passing a particular exit on a busy highway. You can count cars for one minute and you will measure an integer number of cars because cars are discrete objects. If you were to repeat this measurement, you would probably count a slightly different number of cars, just by chance. Some variation between measurements is expected. Measuring the number of x-rays that arrive at a detector within some time window, the integration time, yields variations described by Poisson statistics.

ization is hindered by a lack of suitable x-ray detectors [26, 27]. X-rays can be diffracted, but the experimenter has poor means of adequately quantifying the scattered x-rays.

The development of a high dynamic range pixel array detector, discussed herein, aims to bridge the gap between synchrotron capabilities and x-ray detector capabilities. Chapter 2 discusses the technology of integrating hybrid pixel array detectors and the complementary metal oxide semiconductor (CMOS) technology that underlies their unique functionality. Chapter 3 discusses a particular application of integrating hybrid pixel array detector technology to illustrate the importance of high dynamic range. Chapter 4 discusses the conceptual framework for the high dynamic range detector built in this work. Chapter 5 details the first pixel substructures built for this detector and their characterization. Finally, chapters 6 and 7 discuss the 16x16 pixel x-ray detector constructed with these pixels and discusses its performance.

CHAPTER 2

HYBRID PIXEL ARRAY DETECTORS

2.1 Introduction

Several varieties of x-ray detectors are in operation around the world. Of these detectors, hybrid pixel array detectors (PADs) are arguably best suited to meet the dynamic range requirements of modern synchrotron and x-ray FEL light sources. This chapter contains an outline of PADs and an examination of the technology and semiconductor physics which underlie their functionality. The two primary archetypes of PADs, integrating and counting, will be discussed and compared. Finally, two integrating pixel array detectors with state-of-the-art dynamic range will be discussed, as the strategies they employ will be utilized in this work.

2.1.1 PAD overview

A hybrid pixel array detector (PAD) module consists of three primary components as depicted in Figure 2.1: the diode detection layer, the CMOS electronics layer, and bump bond connections between the two. Additional off-chip electronics are wire bonded to the CMOS electronics layer to send data to and from pixels, supply power, manage bias voltages and currents, and interface with the chip in any other ways needed.

The diode detection layer, or simply the sensor, converts incident signal x-rays into an electronic charge which is measurable by pixel-circuits contained in

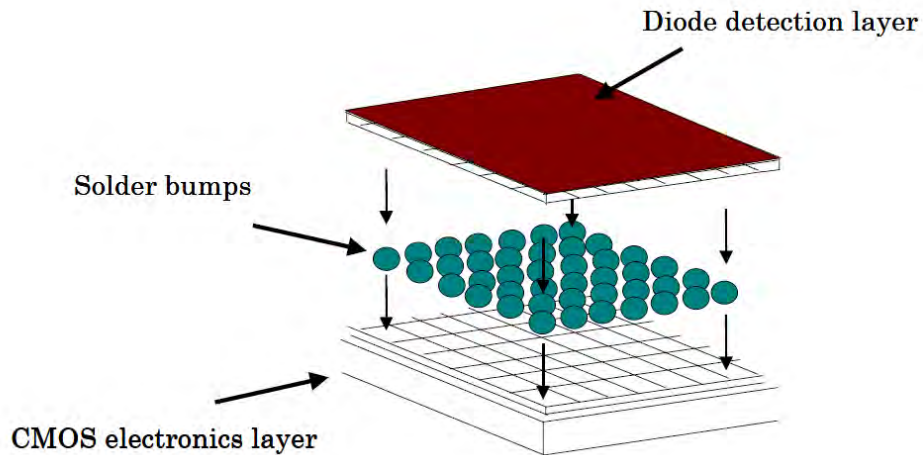


Figure 2.1: A cartoon schematic of a hybrid pixel array detector. The CMOS electronics layer is a lattice of pixel-circuits which measure signals coming from the diode detection layer. The diode detection layer converts incident radiation into an electronic signal. The bump bonds connect the diode detection layer and CMOS electronics layer on a per-pixel basis, transferring electronic signals from the region of the detection layer in which radiation was absorbed to the nearest pixels. The image is adapted from [28] and is not to scale.

the CMOS electronics layer. The CMOS electronics layer, an application specific integrated circuit (ASIC), is the heart of the detector. The ASIC is segmented into pixels, and each pixel contains dedicated signal processing circuitry. Bump bonds connect the two layers pixel-by-pixel such that charge generated in the sensor flows into pixels in the ASIC. Charge carriers generated in the sensor will typically enter the pixels nearest the sensor region in which they were generated. As a result, PADs perform spatially resolved imaging. The ASIC contains additional, non-pixel circuitry to communicate with off-ship electronics.

To understand how these pieces function, some understanding of semiconductor and CMOS device physics is necessary. The following section aims to provide that foundation.

2.2 Semiconductor physics

The simplified discussion given here will be limited to monatomic crystalline semiconductors, as their function is most relevant to this work. By this means we will attempt to gain a qualitative understanding of the origins of some relevant semiconductor properties. More in-depth reviews of semiconductors, semiconductor physics, and CMOS device physics, can be found in many excellent textbooks [7, 29, 30].

2.2.1 Energy bands

Broadly speaking, materials can be categorized by their resistivity as insulators, metals, or semiconductors. Other categories such as semi-metals can be defined, but for the sake of simplicity we will limit discussion to the first three categories mentioned. The resistivity of metals varies, but can be as low as 10^{-10} Ω -cm. A strong insulator can have a resistivity as high as 10^{22} Ω -cm [7]. Throughout the middle of this enormous range are materials called semiconductors. The resistivity of semiconductors is generally temperature dependent. For example, a semiconductor may insulate at low temperatures, but conduct reasonably well at high temperatures. In contrast, many insulators will melt or sublime before attaining an appreciable conductivity [31].

To understand the massive variation in resistivity seen throughout nature, we must understand energy bands in crystalline materials. The possible energies of an electron bound to a lone atom are discrete. These are the so called energy levels of a given element. Two atoms of the same element which are

far apart will each create an identical set of allowed electron states. If we bring the two atoms close together, the degeneracy of their energy levels is broken by splitting into two different but closely spaced energy levels [32]. A crystal is composed of many atoms brought together in a lattice, and the result is the splitting of energy levels into many separate states which, in the case of an infinite crystal, form a continuum called a band. The allowed electron states in a crystal are therefore described by energy bands.

Alternatively, we can view electrons in a crystal as mostly free, but perturbed by a periodic potential produced by the lattice of atomic nuclei. A free electron's momentum is described by a wave vector. In a periodic potential particular wave vectors yield multiple solutions to the Schrodinger equation. Specifically, two standing wave solutions with different energies exist for wave vectors composed of a linear combination of reciprocal lattice vectors. In one solution that standing wave is peaks between peaks in the potential, the lower energy solution, while the other features peaks which coincide with potential peaks, corresponding to a higher energy state. These states are related to Bragg reflections as discussed in Chapter 1, however the wave in this case is the electron's position probability density function. The result is a gap between continuums of allowed electron wave vectors in the presence of a periodic potential [7]. The gaps between bands are known as band gaps.

To be slightly more concrete, figure 2.2 depicts the dispersion relation (energy as a function of wave vector \vec{k}) for an electron in a one dimensional weak sinusoidal potential with periodicity a . The dispersion relation for a completely free electron (i.e. potential = 0 everywhere in space) is a parabola. Figure 2.2 differs from the free electron most notably at integer multiples of $\frac{\pi}{a}$. At these

points two standing wave solutions to the Schrodinger equation exist. Part (b) of the figure depicts the dispersion relation plotted in the reduced zone scheme. The electron's wave vector corresponds to its momentum, and so positive and negative wave vectors describe electrons moving in opposite directions.

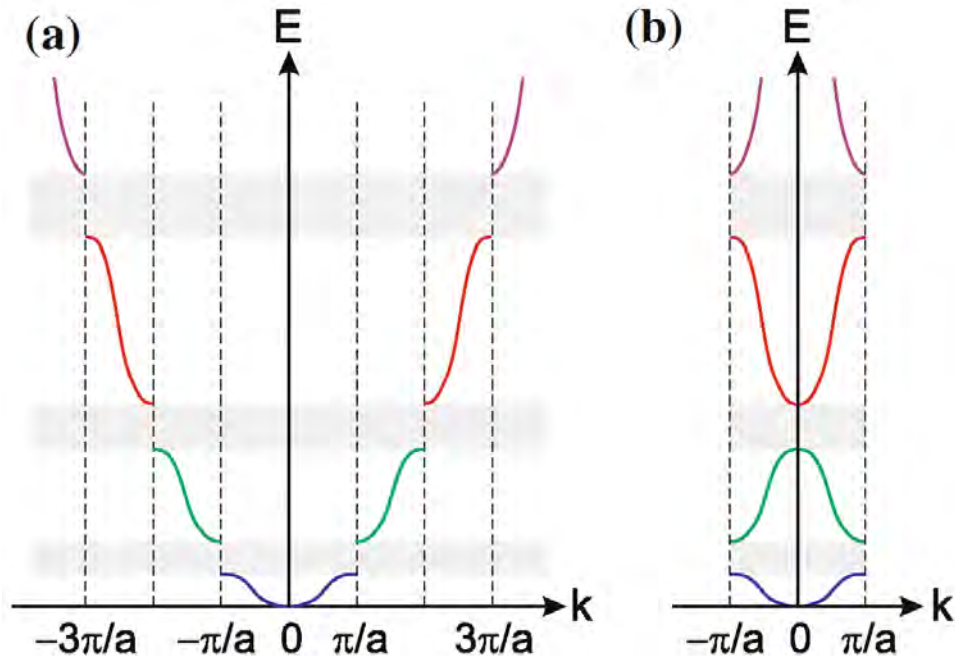


Figure 2.2: (a) Allowed energies of an electron in a one dimensional sinusoidal potential with periodicity a . When the wave vector is equal to an integer multiple of reciprocal lattice vectors, two solutions to the Schrodinger equation exist corresponding to standing waves with peaks on or between the potential peaks. (b) The allowed energies wrapped back and depicted as bands in the "reduced zone scheme." Image adapted from [33].

In the ground state, a band corresponding to energy levels in the valence shell of crystal atoms is the highest energy band with occupied states. If the band is fully occupied, applying an electric field leads to no net movement of charge, because there are an equal number of electrons with a given momentum in one direction as there are in the opposite direction. However, if the band is only partially occupied, electrons can shift in energy to occupy states with momentum in a preferred direction, and a net current can flow with the appli-

cation of an electric field. Metals have a valence band which is partially full and thus conduct electricity. Insulators have a valence band which is completely full, and thus they conduct poorly. However, allowed electron states exist in bands with higher energy than the valence band. With sufficient energy an electron can move to an unoccupied band. If electrons from a fully occupied band are excited into a higher energy band, the material becomes conductive. The band above the valence band is called the conduction band. The band gap in insulators is typically large relative to thermal energy. The band gap in semiconductors is often comparable to the thermal energy (on the order of 1 eV). Higher temperatures lead to greater occupancy of the conduction band in semiconductors. This explains why semiconductors conduct more at higher temperatures, while insulators may melt before they gain an appreciable conductivity.

2.2.2 Doping semiconductors

From the band model we see that a material with a partially filled band conducts electricity, while materials with only full and empty bands are insulators. Materials with nearly full or nearly empty bands are weak conductors. With a suitably small band gap, increasing temperature can alter band populations and increase the conductivity of a semiconductor. An alternative means of increasing the conductivity of a semiconductor is doping.

For a qualitative understanding of doping, consider a silicon crystal. Silicon has four valence electrons and forms a diamond lattice, the silicon atoms each bond covalently with their four nearest neighbors. Suppose that we replace one silicon atom with one boron atom. Boron has three valence electrons, so it will

be able to fulfill three of the four bonds that are ordinarily made by atoms in the diamond lattice.

Because the boron atom lacks an electron relative to the silicon atom it replaces, one electron has been removed from the valence band of the crystal. An electron could be paired with the neighboring, unpaired silicon electron, but in a charge neutral material no electron is present for pairing. One could imagine an electron from a nearby atom jumping over to fill this vacancy. The jumping electron would of course leave behind its own vacancy, which could be filled by another jumping electron, and so on. By replacing a silicon atom with a boron atom we've added a hole to the valence band of the silicon crystal, and the hole can now facilitate the net movement of charge.

Conversely, we might replace one silicon atom with one atom of phosphorus, which has five valence electrons. All four silicon bonds can be satisfied in the diamond lattice, but the fifth valence electron of the phosphorus atom is unpaired. The electron must still occupy a state defined by the band structure of the crystal, and so the electron occupies a state in the conduction band. The electron is free to move with an externally applied electric field, i.e. conduct electricity. Figure 2.3 provides a cartoon depiction of the electron pairing in a fictitious, two dimensional silicon square lattice with and without doping.

Note that the conducting charges in each doping case are opposite polarity. When electron acceptors such as boron are added, the charge moving through the crystal is positive. When electron donors are added, such as phosphorus, the mobile charge is negative. Doped silicon is classified as n or p type, depending on whether the dopant is an electron donor or acceptor, respectively. This process is of course more complicated than presented above. For example, dopants

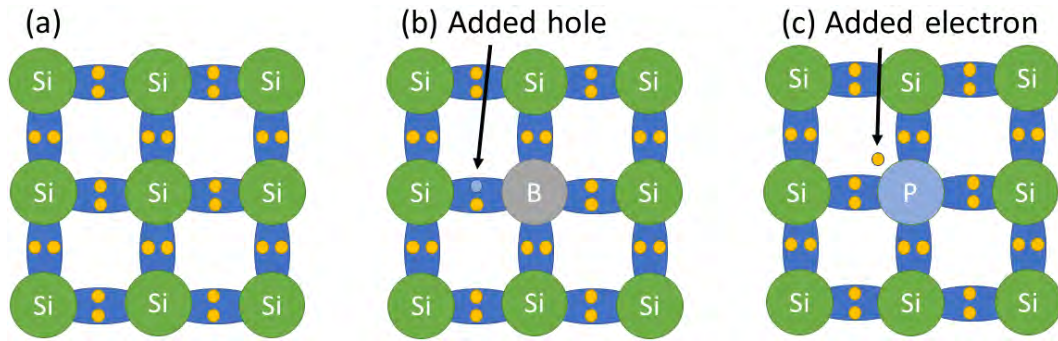


Figure 2.3: Cartoon depiction of electron pairing in a silicon crystal. Note that the diamond structure of the lattice is not represented here. Only valence electrons are drawn. (a) Silicon atom in perfect lattice. Four valence electrons make covalent bonds with all nearest neighboring atoms. (b) One boron atom replaces a silicon atom. A hole is present because the boron has only three valence electrons and cannot bond with all four nearest neighbors. (c) One phosphorus atom replaces a silicon atom. Four of the five phosphorus valence electrons engage in covalent bonding. The fifth valence electron occupies a state in the conduction band.

are generally chosen such that donor electrons will have bound energies close to the conduction band so that thermal excitation will disassociate them from the dopant, but that is not always the case.

Conductivity is dependent on the density of free charge carriers, amongst other things. Therefore the important conclusion from the cartoon depiction above is that doping allows engineers to alter the resistivity of a semiconductor. For example, the resistivity of silicon can be changed by seven orders of magnitude by replacing just one in every one million silicon atoms with a dopant [31]. Doped semiconductors also bring about other interesting properties. Moving forward, as is standard, silicon doped with acceptors will be referred to as p-type silicon while silicon doped with donors will be referred to as n-type.

2.2.3 P-n junctions

Consider two adjacent regions of a doped semiconductor, one doped with donors and the other with acceptors. Charge carriers from each region will diffuse into the other and electrons from donor dopants will fill the vacancies from acceptor dopants. Now the regions on either side of the boundary will possess a net electric charge. Donor dopant atoms which have lost their 5th valence electron now have a net positive charge and acceptor dopant atoms which have accepted a fourth valence electron now have a net negative charge. As a result, an electric field is established across the junction. This field counteracts free charge carrier diffusion, sweeping charge carriers away from the junction and establishing an equilibrium condition. The region that is devoid of mobile charge carriers is called the depletion region.

This p-n junction is a diode. Consider the effects of applying a bias voltage across the device. If the n-doped side of the junction is brought to a higher voltage than the p-doped region, the applied bias serves to widen the depletion region by pulling electrons in the n-doped region away from the junction and pushing holes in the p-doped region away from the junction. The depleted region will grow until the charge of atoms in the region form an electric field strong enough to reach an equilibrium with the externally applied bias. After a brief flow of current out of the diode, no more current flows due to the externally applied voltage. The junction is reverse biased. If we increase the applied bias high enough, electrons receive enough energy from the electric field to jump from the valence band to the conduction band. This is Zener breakdown [29]. Additionally, avalanche breakdown can occur when applied electric fields are strong enough that accelerated charge carriers create electron-hole pairs when

they collide with atoms in the lattice. However, our discussions will not concern these regions of operation.

If enough of the opposite bias is applied, such that the p-doped region is brought to a higher voltage than the n-doped region, each side's respective charge carriers will be pushed towards the junction. Opposite charge carriers from either side will combine and nullify. Here we see that current flows relatively freely. In this case the diode is forward biased.

2.2.4 Radiation in a reverse biased diode

Now return to the case of reverse biasing. Suppose we supply a large enough voltage to deplete the bulk of the semiconductor. In a fully depleted diode the current drawn will be primarily due to thermally excited electron hole pairs generated in the depletion region and swept out by the diode's internal electric field. This is the so-called "dark current." The magnitude of dark current falls off exponentially with temperature as [34]

$$I \propto T^2 \exp\left(-\frac{E_g}{2k_B T}\right) \quad (2.1)$$

where I is the dark current, T is temperature, E_g is the semiconductor's band gap energy, and k_B is the Boltzmann constant. Impurities in the semiconductor material exacerbate the dark current, as the impurities can provide energy levels accessible to valence band charge carriers that are intermediate to the valence band and the conduction band. These "stepping stones" allow smaller thermal excitations to eventually bring electrons to the conduction band.

If a high energy photon is absorbed in a reverse biased diode, the energy

deposited creates a cloud of electron-hole pairs. In silicon, roughly 3.6eV is required to create an electron-hole pair. When a single x-ray with an energy of 8 keV is absorbed in a silicon diode, more than two thousand electron hole pairs are created. The exact number of pairs will vary slightly between absorption events, but note that the distribution of the number of electron-hole pairs created is not Poissonian because the creation of each electron-hole pair is not an independent random event. Rather, the events are correlated and because of the finite number of channels for the x-ray energy to enter, the standard deviation of the number of electron-hole pairs created is only a fraction of the square root of the mean. This fraction is called the Fano factor and equals 0.1 in silicon.

The electron-hole pairs generated form a small cloud [29]. The electric field inside the diode will separate the electrons from the holes and pull them to separate terminals. Figure 2.4 is a cartoon depiction of a reverse biased diode which forms the sensor of a pixel array detector. As the clouds drift through the diode, the cloud expands due to diffusion. More will be said about this in Chapter 4. Some electrons and holes will recombine before separation by the electric field. The rate at which this occurs is the carrier lifetime. In silicon, this lifetime is surprisingly long as a result of silicon being an indirect band gap material, but is often facilitated by impurities and lattice defects. More can be found on the topic in, for example, [35].

Ultimately, a reverse biased diode can serve as a sensor for radiation: photons are absorbed and an electric current flows out of the diode in proportion to the energy of the absorbed radiation. While the specifications of x-ray PAD sensors vary, along with the material used, the detectors in this work utilize 500 microns thick Si photodiode sensors.

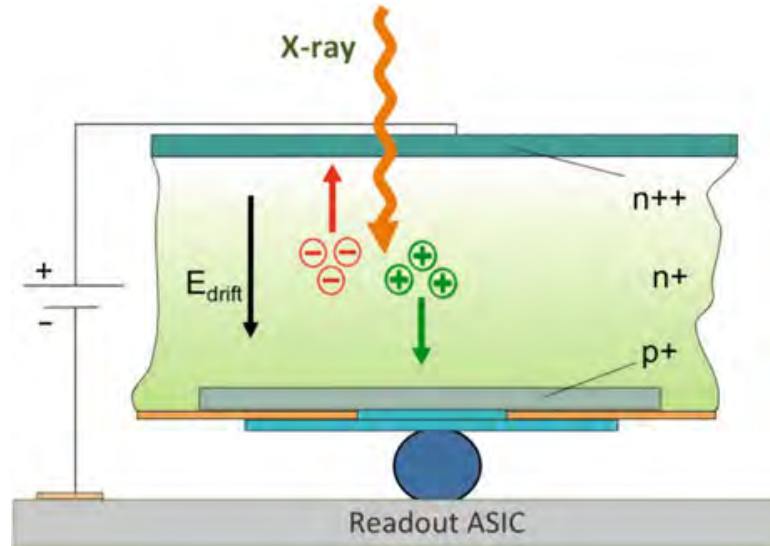


Figure 2.4: Cartoon depiction of radiation being absorbed in a reverse biased diode. The image is not to scale. The clouds of charge carriers formed are offset in this image for clarity. The aluminum contact on the sensor is labeled. Image adapted from [36].

2.2.5 CMOS

Photodiodes provide a means of converting x-rays into current, but a means of measuring this current is still required. The CMOS electronics in the readout ASIC perform this function in hybrid pixel array detectors. In this section we will briefly discuss transistors, which are the primary building block of CMOS circuits.

CMOS stands for complementary metal oxide semiconductor. CMOS devices are based on the doping described in previous sections. CMOS circuits are usually fabricated on silicon wafers and allow many transistors to be fabricated on the same wafer. In addition to semiconductor doping, deposition of metals and silicon oxide (an insulator) are used to build transistors. The transistors discussed in this section are field effect transistors (FET). Figure 2.5 is a cross-sectional view of an n-type metal-oxide-semiconductor field effect tran-

sistor (MOSFET). The transistor is fabricated on a p-type substrate. The device has four terminals (the substrate itself is the fourth terminal, but an explicit substrate connection is not shown here). P-type MOSFETs can be constructed on the same wafer as n-type MOSFETs, but they must be fabricated in a region which is heavily n-doped to form a local n-type well, effectively setting the device in an n-type substrate, and must be biased appropriately. N-type MOSFETs on p-type wafers will be discussed below, but the results apply to both types with appropriate changes in voltage sign and charge carrier species.

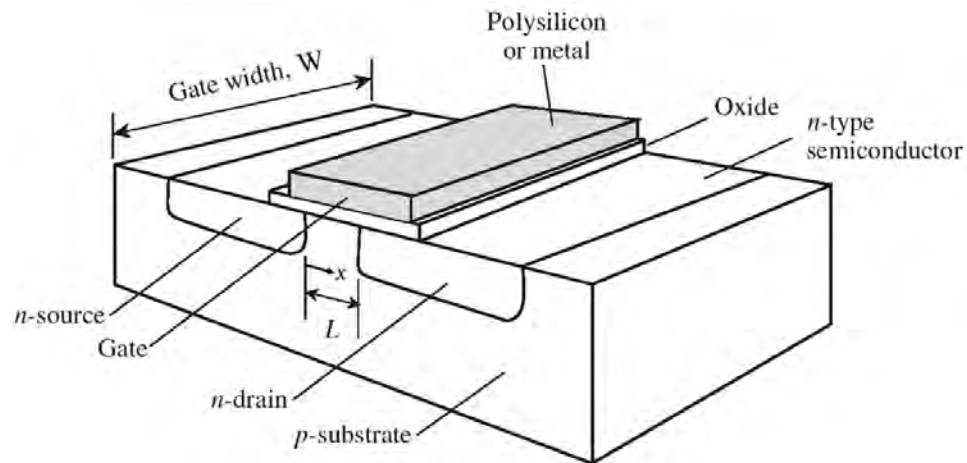


Figure 2.5: N-type MOSFET transistor cross-section. The four transistor terminals are the source, drain, gate, and substrate. Width and length (W and L respectively) describe the dimensions of the conductive channel formed beneath the gate when inverted. Image adapted from [37] with alterations.

Note that the transistor in figure 2.5 is physically symmetric about the gate. For this reason, which terminal serves as the source and which terminal serves as the drain depends on bias conditions. The source and drain terminals are each heavily n-doped regions. Usually the substrate is tied to the lowest system voltage. For our purposes, we will assume that the chip has only a positive supply, and so the substrate is tied to ground. It can be seen based on the analysis of n-p junctions above that the source to substrate and drain to substrate

are diode junctions which will never be forward biased if the substrate remains at ground. The gate terminal is usually composed of metal or a highly doped polycrystalline silicon [38] and is separated from the substrate by a thin insulating layer. If the gate is held at ground and a bias is applied between the source and drain terminals, the n-p-n segment beneath the gate cannot conduct electricity in either direction because one of the n-p junctions will always be reverse biased.

A capacitance is formed between the gate and substrate which is proportional to the product of the length and width of the transistor gate as depicted in figure 2.5. By applying a positive voltage to the gate of the transistor, holes (the majority charge carrier in the substrate) are repelled. A depletion region forms beneath the gate and the electric potential of the substrate at the silicon-silicon oxide interface rises [30]. If the gate bias is increased further, the energy level of the conduction band at the silicon oxide interface approaches the Fermi level of electrons in the substrate [37]. Eventually the conduction band at this interface is populated by electrons and current can flow between the source and drain. When the electron density in this channel is equal to the native hole density of the doped substrate the transistor is said to be inverted: electrons are now the dominant charge carrier at the interface. Note that the "turning on" of a transistor is a gradual process. For the sake of disambiguation, an "on" voltage is defined, generally as the gate voltage sufficient to invert the channel, and is referred to as the transistor threshold voltage (V_{th}).

More formally, for an n-type MOSFET the electric potential of the channel, ψ_s , when mobile electron concentration equals the dopant concentration must

be

$$\psi_s = 2\Phi_F \quad (2.2)$$

relative to ground defined by the substrate very far from the channel, where Φ_F is the potential of the bulk in depletion due to positively charged acceptor atoms which is equivalent to the Fermi level of the unbiased substrate minus the Fermi level of the depleted substrate. From Boltzmann statistics we have

$$\Phi_F = \frac{k_B T}{e} \ln \frac{N_a}{n_i} \quad (2.3)$$

where k_B is the Boltzmann constant, T is temperature, e is the electron charge, N_a is the density of doped acceptor atoms, and n_i is the intrinsic density of charge carriers in the unbiased semiconductor [37]. The gate voltage required to achieve inversion is the threshold voltage:

$$V_{th} = \Phi_{MS} + 2\Phi_F + \frac{Q_{dep}}{C_{ox}}, \quad (2.4)$$

where Φ_{MS} is the difference in work function between the gate material and the substrate, C_{ox} is the gate oxide capacitance per unit area, and Q_{dep} is the charge in the depletion region,

$$Q_{dep} = \sqrt{4\epsilon_{si}eN_a|\Phi_F|} \quad (2.5)$$

where ϵ_{si} is the dielectric constant of the substrate (silicon) [30].

We can analyze the current flow between the source and drain when the channel is inverted. Note that the source is the source of charge carriers conducting through the device. In the case of an n-type transistor the charge carriers are electrons. For gate voltages beyond V_{th} , charge in the channel will mirror charge across the oxide capacitance on the gate. Assuming that the source voltage is held at ground and $V_{gs} \geq V_{th}$ where V_{gs} is the voltage difference between the gate and the source, following the derivation in [30], the charge in the channel

per unit length is

$$Q_d = WC_{ox}(V_{gs} - V_{th}), \quad (2.6)$$

where W is the width of the transistor channel. If the voltage between the drain and source, V_{ds} , is greater than zero, the potential throughout the channel will not be uniform, and the charge density will not be either. The charge per unit length in the channel a distance x from the source will be

$$Q_d(x) = WC_{ox}[V_{gs} - V(x) - V_{th}], \quad (2.7)$$

where $V(x)$ is the potential in the channel as a function of x . In semiconductors, the mean carrier velocity is $v = \mu E$ where μ is the charge mobility and E is the electric field [30], so the current in the channel is

$$I_{ds}(x) = WC_{ox}[V_{gs} - V(x) - V_{th}]\mu_n \frac{dV(x)}{dx}, \quad (2.8)$$

noting that μ_n is the electron mobility in silicon and $E = -\frac{dV}{dx}$. The minus sign in the equation for current is lost because the charge carriers have negative charge, therefore positive current flows in the direction opposite their velocity. Now separating variables and integrating we have

$$\int_{x=0}^{x=L} I_d(x)dx = \int_{V=0}^{V=V_{ds}} W\mu_n C_{ox}[V_{gs} - V(x) - V_{th}]dV \quad (2.9)$$

which, assuming the biases meet saturation criteria, yields current through the channel:

$$I_d = \mu_n C_{ox} \frac{W}{L} \left[(V_{gs} - V_{th}) V_{ds} - \frac{1}{2} V_{ds}^2 \right]. \quad (2.10)$$

For a given V_{gs} the current as a function of V_{ds} is a convex parabola. The maximum current occurs when $V_{ds} = V_{gs} - V_{th}$ and is

$$I_{d,max} = \frac{1}{2} \mu_n C_{ox} \frac{W}{L} (V_{gs} - V_{th})^2. \quad (2.11)$$

$V_{gs} - V_{th}$ is called the overdrive voltage. If $V_{ds} \leq V_{gs} - V_{th}$ the transistor is said to be operating in the triode region.

As mentioned above, transistors do conduct when $V_{gs} < V_{th}$ and the channel is not yet completely inverted. A full derivation of sub-threshold operation is beyond the scope of this work, but excellent treatments of the topic can be found in textbooks such as [37, 38]. The transistor is a core building block with which integrated circuits are constructed, including the ASICs of pixel array detectors.

2.2.6 Radiation hardened components

Radiation damage is an inevitable part of x-ray detector operation. Measures can be taken to minimize the exposure of integrated circuits to radiation, but the issue must always be addressed. Radiation damage in CMOS typically occurs in two forms: displacement damage and ionization damage [34].

Displacement damage occurs when silicon atoms are displaced by radiation. The altering of the silicon lattice leads to altered electrical properties of the material. X-rays do not cause direct displacement damage, as the process requires significant momentum transfer. The damage can be caused by Compton scattering of highly energetic photons, but it is a far less prominent mechanism of radiation damage in x-ray detectors, so this section will focus on ionization damage.

Ionization damage is most evident in the ionization of silicon oxide. Ionization of oxide is problematic because the carrier mobility of electrons and holes in oxide are vastly different. As a result, if an electron is liberated in oxide, it will often leave the material, never to recombine with its hole. Holes will undergo some migration, depending on the applied electric fields, but they are far more prone to trapping in the oxide. This leaves the oxide with an undesired,

long-term positive charge, which creates parasitic electric fields. This can have a range of effects depending on what the oxide in question is used for. Ionization in conductive materials is not damaging because both charge carriers can be neutralized.

In reference to figure 2.5, conduction through the FET is regulated by the voltage on the gate, labeled G. Conduction is inhibited by the opposite doping of the source (S)/drain (D) and the channel/bulk. These nodes cannot conduct unless properly biased. When a positive voltage is applied to the gate of an NMOS transistor, electrons form a channel beneath the gate connecting the drain and source which allows current to flow through the transistor when a drain-to-source voltage is applied.

Ionization damage in the oxide separating the gate from the bulk leads to holes trapped near the oxide-bulk interface. The effect of these holes on the formation of a channel in the FET is the same as a positive voltage being applied to the gate. In essence, ionization damage in FET oxides reduces the gate voltage required to operate the FET. In extreme cases, it could cause a transistor to remain permanently “on.” These trapped holes can be neutralized, for example through tunneling of electrons from the bulk into the oxide. Changes in threshold voltages for FETs due to ionization damage are typically on the order of 100-200mV [39]. Thinner oxides are less prone to long-term ionization damage because the probability of electrons tunneling through to trapped holes is greater at shorter distances, and the ability of holes to migrate out of the oxide is greater for thinner oxides. Ultimately, radiation damage can cause leakage current issues in NFETs, degrading the ability of switches to full open and prevent, for example, voltages sampled on capacitors from drifting. Quantitative

analysis of the impact of radiation damage is entirely dependent on the circuit in question. For instance, it is possible that in some cases radiation damage in more than one part of a circuit can lead to canceling effects. Ultimately, radiation damage causes circuits to function in ways they were not intended to.

Depending on the complexity of the diode detection layer structures, radiation damage can have a significant impact there as well. Insulators are used to prevent leakage current in ring structures around the perimeter of large area diodes used as sensors. High voltages applied to thin diodes (hundreds of volts across a diode that is less than a millimeter thick in many cases) must be prevented from conducting on diode edges. Oxide guard ring structures are often used to segregate regions of varying voltages, and ionization damage can compromise this insulation. This leads to increased dark current.

Further, diodes in PADs typically use some oxide patterning to isolate electrodes of adjacent pixels. Ionization of this oxide could lead to long term charge at the oxide-silicon boundary. As with the NFETs discussed above, this has the potential to form conductive electron channels linking adjacent pixels' electrodes. This would obviously have a detrimental effect on the detector's spatial resolution, as charge being collected in one pixel could easily leak to an adjacent pixel. As a result of this potential for radiation damage, holes are often collected in PADs [40]. Here, positive charge in the oxide actually reinforces the insulating properties of the structure, inhibiting the conduction of holes.

A variety of circuit design, fabrication, and layout techniques have been conceived to produce circuits whose performance is less susceptible to degradation due to radiation damage [39]. As device scaling moves to smaller and smaller feature sizes, the long-term impact of radiation damage is mitigated because

charges trapped in oxide can more readily tunnel out. Even so, it is useful to design circuits whose operation is robust in the face of heavy irradiation.

Designing a radiation hard circuit involves considering what circuit features are most susceptible to radiation damage. For example, in the design of the MM-PAD (a detector discussed in some depth below) pixel integrators, it was noted that bias currents are used to set the functionality of the amplifier. As a result of radiation damage to the bias network, or to biasing transistors in the amplifier, gate voltages associated with given bias currents could be altered. For this reason, it was important to make the function of the amplifier relatively insensitive to bias current variations within a range that could be expected to result from radiation damage.

Several steps have been identified in the device fabrication process which can reduce the susceptibility of a circuit to radiation damage. For example, hydrogen at the silicon-silicon oxide boundary of FETs serves to increase the trapping of holes at the interface, which is detrimental to the function of FETs, as discussed above. Annealing of intermediate circuits in pure nitrogen at specific temperatures has been found to decrease the amount of hydrogen trapped at the boundary, and thus reduce the detrimental impact of radiation on CMOS circuits fabricated in this way. At the layout level, many design structures, which often come with an increased area cost, have been implemented to produce more radiation hardened circuits. Incorporation of p-doped silicon guard structures to reduce thickness of oxides required in some circuit structures is one example of these techniques [39].

2.3 Pixel array detectors

In this section we present a brief overview of pixel array detectors followed by a discussion of the two dominant pixel architectures with which PAD ASICs are built: counting and integrating.

As depicted in figure 2.1, hybrid PADs consist of two distinct layers, a dedicated sensing layer and a signal processing layer. To provide a sense of scale, figure 2.6 is a photograph of a hybridized sensor wire bonded to support electronics. Figure 2.7 is a photograph of the an unhybridized PAD ASIC. The detector depicted in figure 2.6 is the CS-PAD [41]. The detector depicted in figure 2.7 is the MM-PAD. It is a 128x128 pixel array with 150 μ m pixel pitch and a 500 μ m thick silicon sensor.

As discussed above, the sensing layer of a PAD is typically a monolithic photodiode which is reverse biased and functions as described above. The sensing layer is connected to the signal processing layer pixel-by-pixel via bump bonds. Charge generated via x-ray absorption in the sensor is transferred to the pixelated, signal processing ASIC. The diode is biased to create electric field lines perpendicular to the p-n junction with the aim of sweeping photo-generated charge from the point of absorption directly to the pixels corresponding to that volume. Some patterning on the back side of the sensor is required to facilitate the bonding of the ASIC and reduce cross-talk between pixels.

The ASIC contains an array of pixel-circuits. Each pixel contains its own signal processing circuitry which can function in a number of ways. Below we will discuss two dominant pixel architectures employed in hybrid PADs for measuring x-ray signals.



Figure 2.6: Photo of the CS-PAD hybridized ASIC wirebonded to support electronics. The wirebonds send biases and control signals to the ASIC, and also transmit readout signals from pixels to support electronics for processing and recording. The silicon sensor layer is about 20mm wide. (photograph by Mark W. Tate)

2.3.1 Integrating detectors

Integrating detectors accumulate a signal over time and output a value indicative of the integrated quantity. Each pixel-circuit also contains elements which send signals indicative of the collected charge to circuits outside of the pixel, but for the time being we will focus on the integrating portion of the pixel, the front end circuitry. Figure 2.8 depicts a basic integrating pixel front end. The diode in the schematic represents a connection to the PAD sensor layer. The capacitor C_d is not an explicit capacitor, but represents parasitic capacitance on the integration node from sources such as the connection to the sensor. Charge collects on the inverting terminal of the op-amp, which is connected to the op-amp's out-



Figure 2.7: MM-PAD ASIC bump bonds. The ASIC contains a 128x128 array of solder bumps, one connected to each pixel, which can be bonded to a sensor with suitable backside metalization. Pixel pitch is 150 μm .

put through the feedback capacitor C_f . The op-amp produces a voltage which pulls incident charge onto the feedback capacitor such that the inverting terminal voltage will remain equal to the non-inverting terminal voltage, which is typically supplied by an external source [42].

For small signals, the integrator resolution will be limited by noise sources originating in the detector. For large signals, without additional circuitry, the full well of the integrator in figure 2.8 will be limited by its feedback capaci-

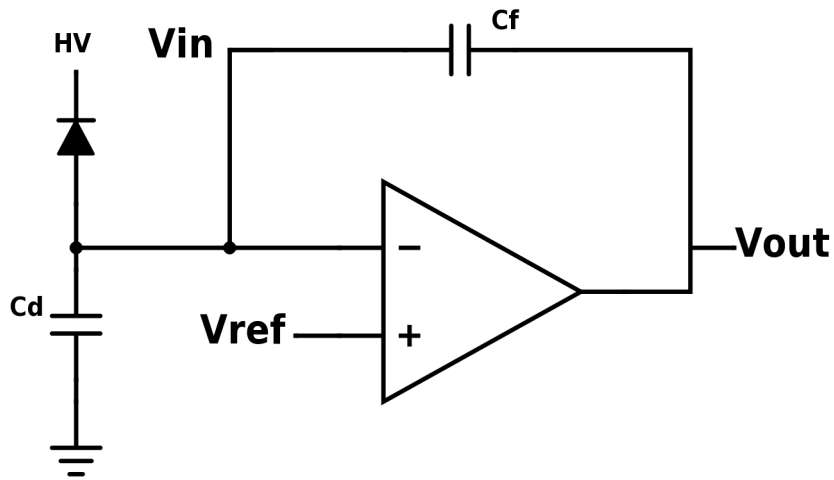


Figure 2.8: Basic integrating pixel schematic. The diode represents a connection to the photodiode sensor. The amplifier collects charge incident from the photodiode onto C_f . C_d is not a real capacitor, but represents the parasitic capacitance on the front end of the pixel. V_{out} is the pixel output, typically digitized outside of the pixel through an analog transmission chain (not shown).

tance and operating voltages. A larger capacitor will allow charge generated by a larger number of x-rays to be collected, but this impacts the small signal sensitivity of the integrator. Increasing the capacitance reduces the gain of the integrator and increases the equivalent noise charge due to noise sources internal to the amplifier [43]. Therefore, to maintain single photon sensitivity, a sufficiently small capacitor must be used. To better understand these limitations, the basic operation of an integrating pixel is derived below.

Integrator properties

Assume that the amplifier in figure 2.8 is an ideal op-amp with infinite input impedance and large gain A . The output voltage of the amplifier is

$$V_{out} = A(V_{ref} - V_{in}). \quad (2.12)$$

If positive charge Q_{in} enters the integration node through the photodiode, V_{in} increases and V_{out} decreases. As a result, the voltage across the feedback capacitor increases to

$$\Delta V_f = V_{in} - V_{out} = V_{in} - A(V_{ref} - V_{in}). \quad (2.13)$$

Assuming for the time being that the parasitic capacitance C_d is small, all charge must be pulled onto the feedback capacitance because the input impedance of the amplifier is infinite, so

$$Q_f = C_f \Delta V_f = Q_{in}. \quad (2.14)$$

The charge to voltage gain of this configuration is then

$$\frac{V_{out}}{Q_{in}} = \frac{A(V_{ref} - V_{in})}{C_f(V_{in} - A(V_{ref} - V_{in}))} \approx \frac{-1}{C_f} \quad (2.15)$$

for large A . Therefore the output of the integrator in relation to the input charge is approximately determined by the feedback capacitance.

Of course, this initial derivation neglects several important details. To understand the interaction between C_f and C_d , we can view C_f as a capacitor connected in parallel to C_d with a capacitance enhanced by the dynamic response of the backside voltage, the so called Miller effect [34]. In this way, the effective capacitance on the front end due to C_f is

$$C_{eff} = C_f(A + 1). \quad (2.16)$$

The input charge is distributed between the two capacitors, C_f and C_d . The fraction of charge deposited on C_f , which is the quantity being measured, is

$$\frac{Q_f}{Q_{in}} = \frac{C_{eff}}{C_{eff} + C_d}, \quad (2.17)$$

which is approximately one for large gain or small C_d . This emphasizes the importance of a high gain integrating amplifier and illustrates that parasitic capacitance on the pixel front end degrades the integrator charge collection efficiency.

2.3.2 Amplifier noise in feedback

As noted above, the small signal resolution of an integrating pixel array detector is limited by the noise performance of the charge sensitive pre-amplifier (the integrator). Output referred noise from the amplifier sees a capacitive voltage divider formed by the feedback capacitor and the front end parasitic capacitance. As a result, the output referred noise of the integrator shows up on the input as [44]

$$V_{in} = V_{out} \frac{X_{C_d}}{X_{C_f} + X_{C_d}} \quad (2.18)$$

which simplifies to

$$V_{out} = V_{in} \left(1 + \frac{C_d}{C_f} \right) \quad (2.19)$$

where V_{in} is the noise on the input as a result of the output referred noise being fed back, V_{out} is the output referred noise, X_{C_d} and X_{C_f} are the reactance of the front end parasitic capacitance and the feedback capacitance respectively, and C_d and C_f are those capacitances. The equivalent input noise charge, the amount of integrated charge that the noise is interpreted as, is then

$$Q_{noise-in} = V_{out} C_f = V_{in} (C_d + C_f) \quad (2.20)$$

which yields a signal to noise ratio of

$$\frac{Q_s}{Q_{noise-in}} = \frac{Q_s}{V_{in} (C_d + C_f)} \quad (2.21)$$

where Q_s is the charge signal you hope to measure, subject to the charge collection efficiency derived in the previous section. Based on the analysis above, we can design amplifiers with acceptable noise characteristics. Acceptable is of course a subjective term, so design goals must be set. For example, it is commonly desirable in x-ray PADs to achieve good single x-ray sensitivity. It can then be decided that the average integrated noise power of the amplifier must

yield a signal to noise ratio of at least 5 for the signal from a single 10keV x-ray. Given amplifier noise characteristics and expected parasitic capacitances, a maximum integration capacitance can be chosen. Conversely, a desired full well might dictate the integration capacitance, and an amplifier with sufficiently low noise can then be designed.

Calculation of the noise signal from a specific amplifier involves modeling the noise of each component in the circuit, and propagating its effect through the rest of the circuit. For example, if a transistor gate forms the input of an amplifier, the noise generated by that transistor, modeled as an input voltage noise source, results in the initial input noise power multiplied by the entire amplifier's gain. Noise from other transistors within the amplifier may have less of an impact on the amplifier's total noise. The bandwidth of the system also regulates the impact of noise sources. When examining an amplifier for noise consideration, it is also important to look at the amplifier's susceptibility to external noise sources, such as power supply ripple.

2.3.3 Electronic noise

Amplifier noise is a complicated subject and highly dependent on the specific amplifier in question. An examination of general noise considerations will be given here which is applicable to all amplifiers. While the discussion of noise in feedback above dealt with output referred noise for the purpose of analysis (that is the combination of all noise sources inherent to the amplifier), the source of noise in amplifiers is typically internal to the device. Two forms of noise are present in all circuits, namely Johnson noise and flicker noise, or $1/f$ noise [42].

Johnson noise, also referred to as thermal noise, arises from random, thermal motion of charge carriers in circuit elements. Take a simple resistor as an example. The charge carriers in the resistor undergo random thermal motion, and at any given moment we can expect to find a different number of electrons on either end of the resistor. Even if the resistor is not connected to a circuit of any kind, the free charge carriers in the resistor will be in motion. The time average of the charge carriers' velocities is zero, but at any given moment there may be a non-zero voltage across the resistor due to charge imbalance. This phenomena is the source of thermal noise in circuits. We find that the noise power spectral density associated with Johnson noise is [42]

$$\overline{V_n^2} = 4k_B T R \quad (2.22)$$

where k_B is the Boltzmann constant, T is the temperature of the resistor, and R is its resistance. For field effect transistors, the power spectral density of thermal noise is [30]

$$\overline{V_n^2} = \frac{8k_B T}{3} g_m \quad (2.23)$$

where g_m is the transconductance of the transistor. Johnson noise is present in any circuit element with finite resistance and its power spectrum is white. In equation 2.22, equation 2.23, and all following equations in this section, power spectral density is being referenced, and each equations is implicitly in watts per hertz (W/H_z). The noise is subject to filtering effects of the circuit in question, and the total noise power manifested is the integral over frequency of the relevant noise quantity (e.g. equation 2.22 for a purely resistive network) multiplied by the transfer function of the effective filter.

Flicker noise is also pervasive and arises from trapping of charge carriers in materials. Often this trapping occurs at material boundaries such as field effect

transistor (FET) gate oxide boundaries. Material boundaries present dangling atomic bonds which introduce extra energy states accessible to charge carriers, creating the potential for temporary trapping of charges [34]. Because conduction in FETs occurs at the oxide boundary, flicker noise is the dominant form of noise in FETs. Interestingly, flicker noise is not frequency independent. It generally exhibits a spectral dependence of the form $1/f^n$ where n is some number indicative of the material or sample, but typically of order one. For this reason flicker noise is often referred to as $1/f$ noise. For FETs, flicker noise is often modeled as a voltage source on a FET's gate with average spectral power density of [30]

$$\overline{V_n^2} = \frac{K}{C_{ox}WL} * \frac{1}{f} \quad (2.24)$$

where K is a process dependent constant on the order of $10^{-25}\text{V}^2\text{F}$, C_{ox} is the gate-oxide capacitance per unit area, and WL is the product of the width and length of the transistor gate in question.

Each of these noise sources can be represented in a circuit in multiple ways. Often circuits are modeled as noise-free circuits with noise voltage or current sources added as described by equations such as 2.22 and 2.24, but placement of these noise sources is important. Noise can be represented as input or output referred and as a voltage or current source. For example, if an amplifier with gain A_0 has a noise output of $\overline{V_n^2}$, the circuit model can include a noise source on the amplifier's output with power spectral density $\overline{V_n^2}$ or a noise source on the amplifier's input with power spectral density $\overline{V_n^2}/A_0^2$, as discussed above. Typical noise root mean square (RMS) magnitude in CMOS amplifiers are on the order of nV/\sqrt{Hz} input referred noise voltage.

2.3.4 Counting detectors

Photon counting PADs are an alternative to integrating PADs that minimize the impact of many noise sources. Rather than accumulating signal over time, photon counting detectors perform pixel level discrimination of signals in real time. Figure 2.9 depicts the core of a photon counting pixel. The diode in the schematic represents a connection to the PAD sensor layer. The capacitor C_d represents parasitic capacitance on the integration node. Photon absorption in the sensor produces a burst of photocurrent that enters the pixel and interacts with the analog pulse shaping circuitry. The output of the pulse shaper is monitored by a comparator, and if the peak pulse voltage is greater than the threshold voltage, V_{th} , an in-pixel counter is incremented. The counter is read out to off-chip electronics at the end of the exposure.

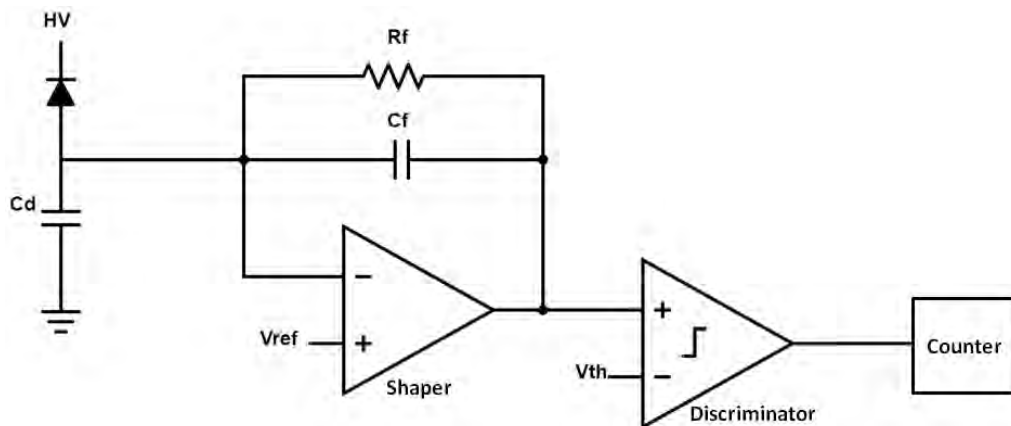


Figure 2.9: Basic counting pixel schematic. The diode represents a connection to the photodiode sensor. C_d is not a real capacitor, but represents the parasitic capacitance on the front end of the pixel. The pulse shaper outputs a pulse for incident photocurrent spikes. The comparator determines whether the pulse height indicates that an x-ray was absorbed in the sensor. When the comparator fires, the counter is incremented. The total digital counts in a given period are readout off chip (read out chain not shown).

The pulse shaper can be constructed in many different ways, but often con-

sists of an integrating amplifier with a DC feedback element, such as a resistor, to prevent signal from persisting on the integration capacitance [45]. The threshold V_{th} can be set such that only x-rays with sufficient energy will trigger the comparator and thus increment the counter. This has several advantages and disadvantages which will be discussed in the next section. amplifier noise on the front end amplifier and power supply or reference voltage fluctuations, along with the pulse shaper properties, set the minimum photon signal which can be recorded.

By performing an analog to digital conversion at the pixel level, full well is no longer limited by a capacitor size, but instead the depth of a digital counter. This extends the full well drastically.

2.3.5 Comparing integrating pixels and counting pixels

By identifying individual photon events, counting detectors (with proper calibration, which can be difficult) are able to ignore dark current entirely. In contrast, integrating detectors accumulate dark current, which must be accounted for in measurements through a background subtraction. Furthermore, threshold discrimination can eliminate fluorescence photons from imaging if the energy of the fluorescence is sufficiently lower than the energy of the photons of interest. Some photon counting detectors, such as the Medipix3 can use multiple thresholds and multiple in-pixel counters, which enables “color” imaging [46]. For example, if two distinct photon energies are expected in an image, photons of each energy can be distinguished. This is only possible in integrating detectors if very few photons arrive in the integration window, such that

the signal can be reliably divided into photon components. These photon counters are able to reject higher harmonic x-rays from storage ring sources, which is not possible with integrating detectors. The signal from higher harmonics appear as several fundamental wavelength x-rays arriving at the same pixel in integrators.

By performing analog to digital conversion in-pixel, photon counting detectors are also less susceptible to noise in the readout chain, as digital values are more robust in transmission than analog values.

However, photon counting detectors have significant drawbacks relative to integrating detectors. To begin, setting the detection threshold is not trivial, and pixel level trimming of threshold values is often necessary. Without perfect threshold selection, pixel boundaries can become insensitive to x-rays. This is because an x-ray which is absorbed at a boundary between pixels will deposit a portion of the generated charge into each nearby pixel. The pulse in each pixel may then be too small to pass the threshold for photon detection. This problem is worst at pixel corners in a square pixel array, where charge is shared between four pixels. Alternatively, a split event may signal detection in more than one pixel and the x-ray will be double-counted. Some circuits have been designed to address this problem, for example the Medipix3 counting detector permits pixels to communicate with nearest neighbors to negotiate split events and properly assign photon counts to whichever pixel receives the most charge, provided that the pixels cumulatively received enough charge to cross the detection threshold [47]. These systems have their own complication, including the necessity of elaborate calibrations.

Perhaps most problematic in many applications of counting detectors rel-

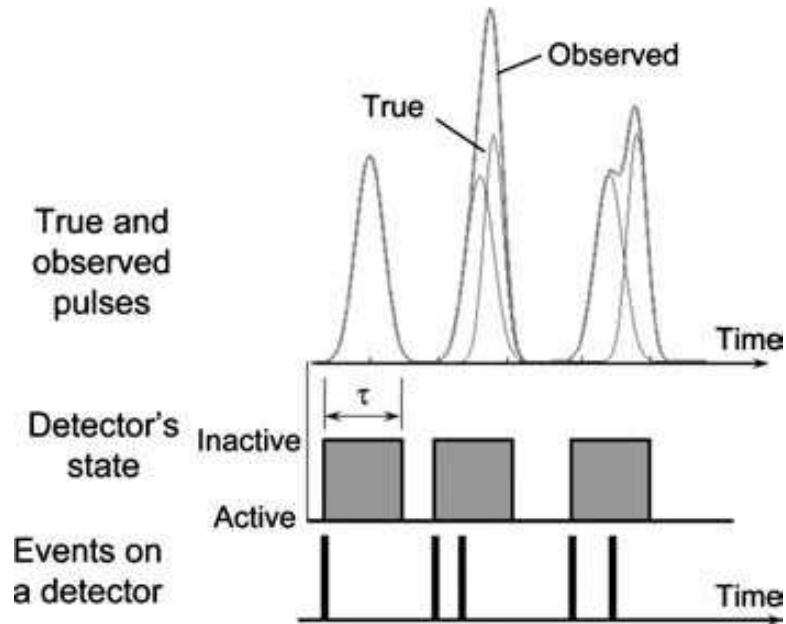


Figure 2.10: Illustration of pulse pileup in a photon counting detector. The true and observed pulses line depicts the "true" pulses that would result from each photon event individually on top of the "observed" pulses that the pulse shaper outputs. The detector's state line illustrates the window in which the comparator will read only one photon, while the events on detector line is the actual timing of photon events. With five photons incident on the pixel, only three are counted. Image adapted from [48].

ative to integrating detectors is the count-rate limitation of photon counting pixels. Photon counting pixels shape incident photocurrent pulses with some characteristic time constant. If more than one photon arrives within the span of this time constant, a composite pulse will be produced, and the comparator may be unable to distinguish the two events from a single photon event. In essence, multiple photons arriving within a sufficiently small time window are counted as a single photon. The pulse pileup problem is illustrated in figure 2.10. The figure depicts a counting detector pulse shaper output with five photons incident. The individual pulses are drawn beneath the composite pulses. The Detector's state indicates that only three photons are recorded.

This severely limits the maximum flux which can be utilized in experiments

with photon counting detectors. Because the arrival of photons is subject to shot noise, maximum flux must be kept below a level which produces even a small probability that more than one photon may arrive at any given pixel within the shaping time constant. This shortcoming is exacerbated by the pulsed nature of synchrotrons which often have a duty cycle as low as 0.05%. Figure 2.11 plots measurements of average flux taken at the European Synchrotron Radiation Facility (ESRF) under different fill conditions. In most cases, measurement linearity rolls off significantly at just 10^6 counts per second (cps). The degradation of linearity varies based on synchrotron fill pattern because the limiting factor for counting detectors is not average flux, but instantaneous flux. More intense pulses of x-rays are more prone to under counting. This means that counting detectors are effectively non-viable for use at XFELs, where all x-rays arrive in less than one picosecond.

Some circuits have been devised to address this limitation of photon counting detectors. For example, some models of the PILATUS photon counting detector utilize a re-triggering technique to gain better measurements of photons arriving at a pixel experiencing pile-up [36]. If a pulse is long enough to keep the in-pixel comparator high (presumably due to pileup) the comparator is forcefully re-triggered after some predefined time, and a second count is registered. Measurements from [50] demonstrating improved count rates with forced re-triggering is plotted in figure 2.12.

Alternatively, some photon counting detectors simply multiply signals by a correction factor when rates which are known to experience pileup are measured. While these techniques help, they also introduce greater uncertainty into the measurement. Overall, photon counting detectors offer great advantages

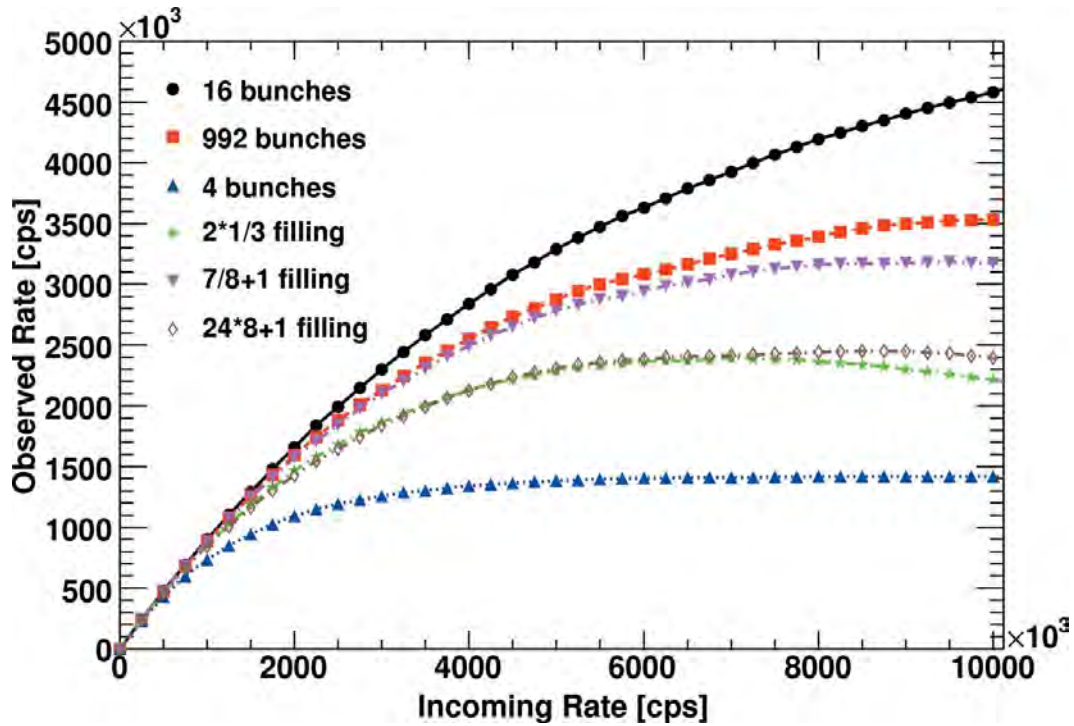


Figure 2.11: Measured counts per second (cps) of incident x-rays on a PILATUS photon counting pixel versus the actual flux at the European Synchrotron Radiation Facility (ESRF). Here we see the impact of synchrotron pulse structure on the count rate limitations of photon counting detectors. Regardless of average flux, the instantaneous flux measurable by a counting pixel is limited. Observed count rate varies with synchrotron mode. The plot is adapted from [49].

in noise reduction and extraneous signal rejection. However, count-rate limitations make them best suited to relatively low flux applications.

2.4 Integrating PAD state-of-the-art

As discussed above, the full well of a simple integrating pixel, defined as the amount of integrated photocurrent that can be stored in such a pixel, is limited by the size of the front-end amplifier feedback capacitance for a given output voltage swing. Increasing the integration capacitance to increase full well

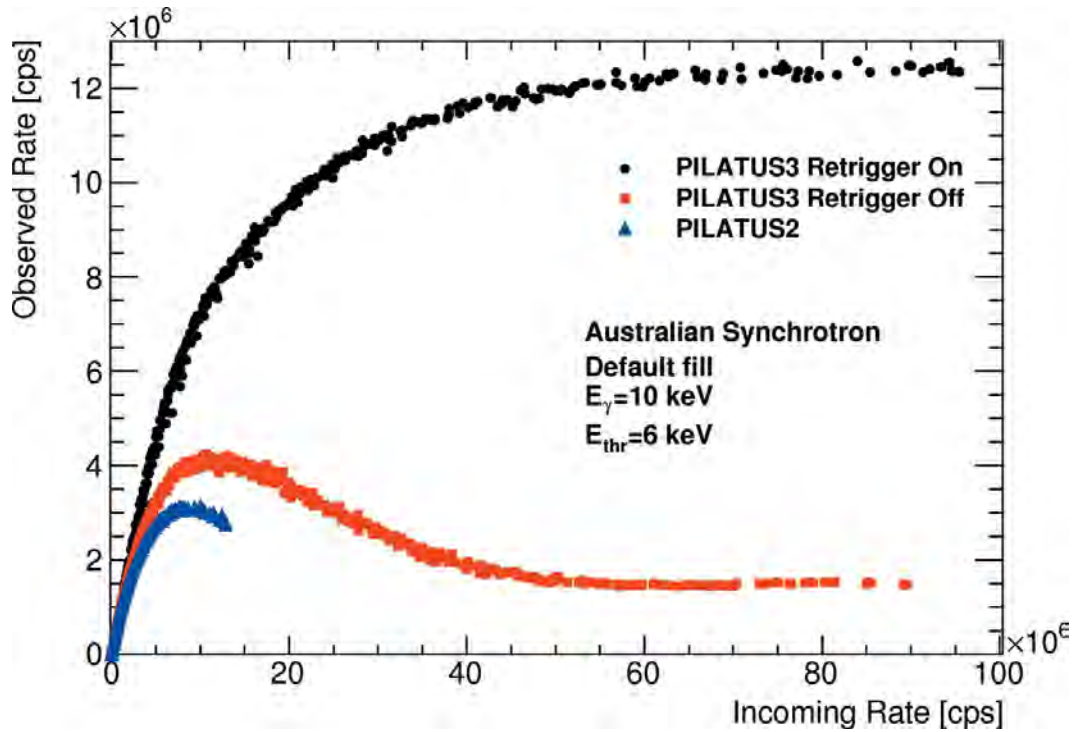


Figure 2.12: Measured count rate of incident 10 keV x-rays on a PILATUS3 photon counting pixel versus the actual flux. Severe count rate non-linearity occurs above 10^6 counts per second without re-triggering. Implementation of re-triggering improves estimation of count rate to some extent, but is still inherently limited. The plot is adapted from [50].

is ultimately constrained by pixel size. Perhaps more importantly however, a larger integration capacitance couples the output noise of the integrating amplifier to its front-end more strongly, leading to a larger equivalent noise charge, and thereby obscuring small signals. Thus increasing the well depth of an integrating pixel while maintaining sensitivity to single photon signals requires architectures more sophisticated than the simple integrator discussed above.

2.4.1 The Mixed Mode Pixel Array Detector (MM-PAD)

Dynamic range extension of an integrating pixel can be achieved in many ways, one of which is eliminating integrated charge to prevent integrator saturation. If this is done in a controlled way, the total integrated charge can be reconstructed. For example, the readout ASICs described in [51] and [52] each use charge pumps to systematically eliminate integrated charge, and the number of charge pumps utilized is recorded as a digital value. The mixed-mode pixel array detector (MM-PAD), a detector developed by Sol Gruner's research group at Cornell University [53], performs this digitization in each pixel of a two dimensional array during integration.

In the MM-PAD, photocurrent resulting from absorption of x-rays in a reverse-biased photodiode is integrated onto a charge sensitive amplifier whose output is monitored by a comparator. When the amplifier output (V_{out} in figure 2.13) crosses an externally set threshold (V_{th} in figure 2.13), a gated oscillator is enabled that triggers a counter and the switched capacitor circuit enclosed in the dotted box in figure 2.13. With each pulse of the gated oscillator this switched capacitor removes a fixed quantity of charge ($\Delta Q = C_{rem}(V_{front-end} - V_{low})$) from the integration node while an in-pixel counter is incremented. The charge removal incurs no dead time and helps the integrator avoid saturation. The integration capacitance is sized such that the signal from a single 8 keV x-ray is readily measurable with an excellent signal to noise ratio. This strategy shifts the full well limiting parameter from the size of a capacitor to the depth of the in-pixel digital counter.

Figure 2.14 plots measurements which outline the mixed mode integration of the MM-PAD. Section (a) of figure 2.14 is the analog portion of integrated

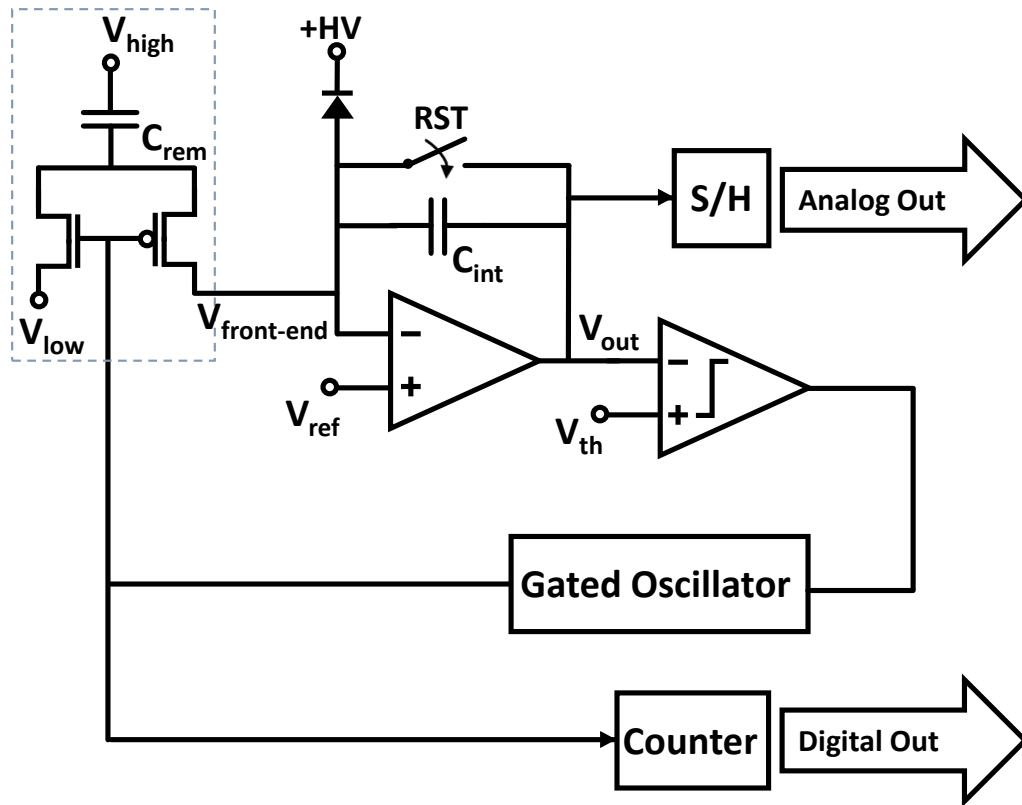


Figure 2.13: Simplified MM-PAD schematic. The switched capacitor for charge removal is enclosed in the dotted box. The diode in the schematic represents a connection to the detector sensor, a reverse-biased diode.

signal. This is scaled and merged with the digital portion in (b) to produce a measurement of total input (with a constant source) versus exposure time in (c). By utilizing in-pixel digitization and elimination of signal during integration, the MM-PAD achieves a full well of 4×10^7 8 keV x-rays/pixel/frame while maintaining sensitivity to signals as small as one 8 keV x-ray. The detector also achieves a frame rate of 1kHz [53]. The pixel array is composed of six modules butted in a 2x3 array, and each module is composed of 128x128 pixels with 150 μ m pitch.

Mixing digital and analog modes in the MM-PAD has its own limitations. Most prominently, in the existing design, digitization and removal of integrated

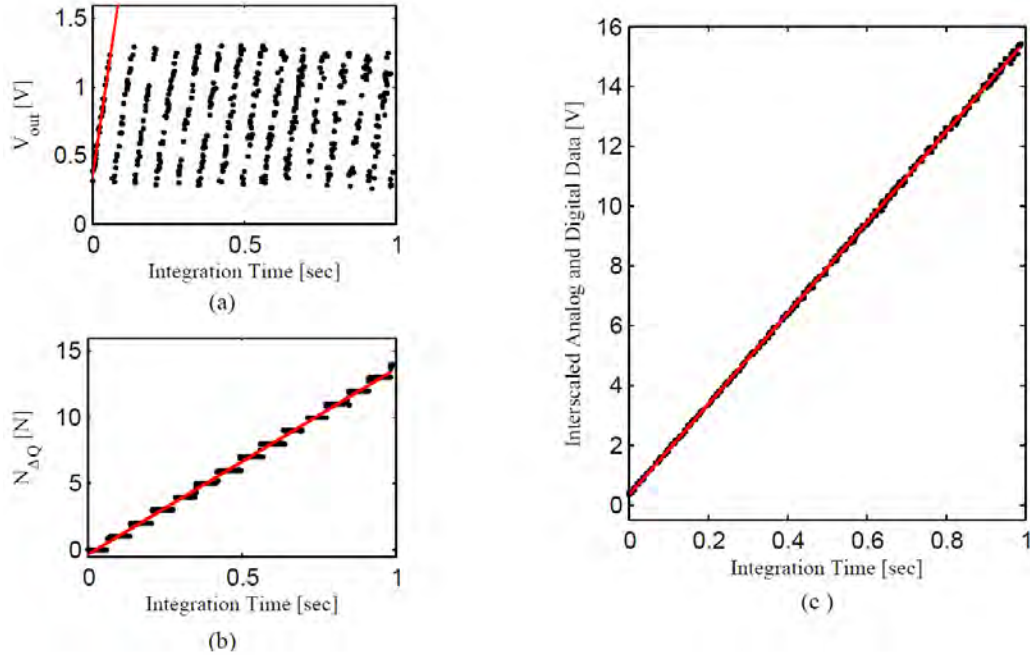


Figure 2.14: (a) Analog output signals as a function of exposure time while integrating a constant source. The output forms a sawtooth wave, dropping each time a charge removal cycle is executed. (b) Number of charge removal cycles executed versus exposure time. Data corresponds to the measurements in (a). (c) Analog output signals merged with digital output yielding total integrated signal versus exposure time. The red line in each plot is a fit to illustrate linearity. Plots adapted from [54].

charge is limited to a rate of 2MHz. This is the maximum speed at which the in-pixel gated oscillator was designed to run. Reliable charge integration in the high flux regime requires that, once the charge removal capacitor is connected to the integration node, the node returns to virtual ground before it is disconnected. Deviation from this behavior leads to uncertainty in ΔQ , the charge removed per oscillator cycle. The MM-PAD amplifier meets this requirement within its design specifications, but the question of front-end virtual ground fidelity becomes more challenging with larger inputs, particularly for high peak photocurrent. In the MM-PAD, the charge removed per gated oscillator cycle is roughly equal to the integrated photocurrent generated by 200 8 keV x-rays

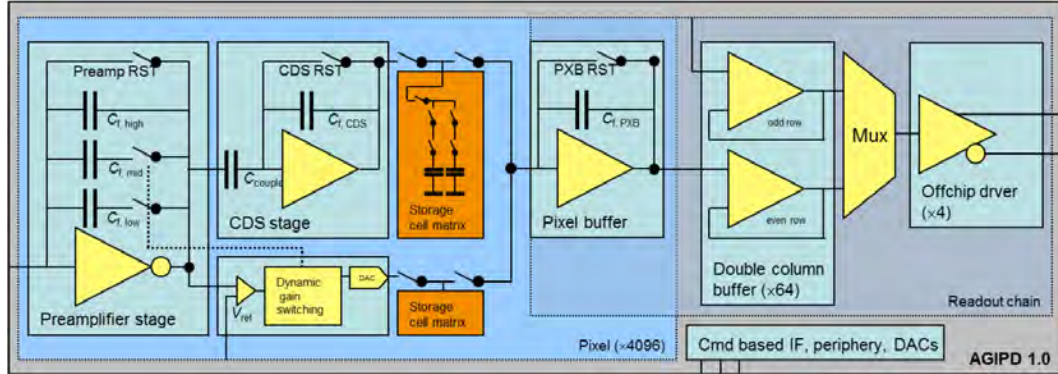


Figure 2.15: Block level AGIPD schematic taken from [5]. Capacitors $C_{f,mid}$ and $C_{f,low}$ begin with switches open. If the integrator output voltage crosses V_{ref} the switch connecting $C_{f,mid}$ is closed. If V_{ref} is crossed again, $C_{f,low}$ is connected. The storage cell matrix after the CDS stage is an array of in-pixel storage cells for burst framing.

converted in the silicon x-ray sensor, resulting in a sustained flux capability of 4×10^8 8 keV x-rays/pixel/s.

2.4.2 The Adaptive Gain Integrating Pixel Detector (AGIPD)

An alternative means of extending dynamic range has been demonstrated by the Adaptive Gain Integrating Pixel Detector (AGIPD), a detector currently under development for the European XFEL by a collaboration between Deutsches Elektronen-Synchrotron (DESY), the Paul-Scherrer-Institute (PSI), the University of Hamburg, and the University of Bonn, led by Heinz Graafsma [4, 5]. Figure 2.15 depicts a block level schematic of the AGIPD pixel. Like the MM-PAD it is an integrating pixel, but extends dynamic range with an adaptive gain scheme rather than charge removal.

Like the MM-PAD, the integrating amplifier begins framing with a capacitor small enough to measure the signal of a single x-ray and a comparator monitors

the amplifier output. When the integrator is approaching saturation, the comparator signals the control logic, and a second capacitor, this one significantly larger, is connected in parallel to the first ($C_{f,mid}$ in figure 2.15). By increasing the total feedback capacitance, the gain of the integrator is reduced and saturation is avoided. As demonstrated in previous sections, sensitivity to single x-rays may be lost with the additional feedback capacitance, but under these conditions the integrated signal is already larger than a single x-ray, so the reduced resolution is tolerable so long as shot noise remains the dominant source of uncertainty. A third capacitor, larger still, is available in the event that saturation is reached a second time.

When reading out, the AGIPD transmits the integrated signal as an analog value in addition to a second value which indicates the final gain stage engaged while framing. In this way the AGIPD achieves a full well of more than 10^4 x-rays per pixel per frame. There are minimal instantaneous flux limitations on the pixel. This is important because the pixel is designed for use at the European XFEL, where x-ray pulses with durations on the order of femtoseconds will have to be measured. The AGIPD provides a means of integrating arbitrarily short x-ray pulses with up to 10^4 12 keV x-rays/pixel/pulse. In contrast, the MM-PAD can integrate arbitrarily short x-ray pulses of up to 200 8 keV x-rays and experiences count rate limitations for larger pulses. The limitation is set by the rate of charge removal. However, the maximum full-well and thus dynamic range of the AGIPD is still constrained by capacitor size, and thus pixel size. The MM-PAD full well is set by the depth of a digital counter, which scales exponentially with number of bits and is in general drastically smaller than capacitors in CMOS. With a significantly deeper full well, the MM-PAD can integrate sustained fluxes of up to 4×10^8 8 keV x-rays/pixel/s. While the adaptive

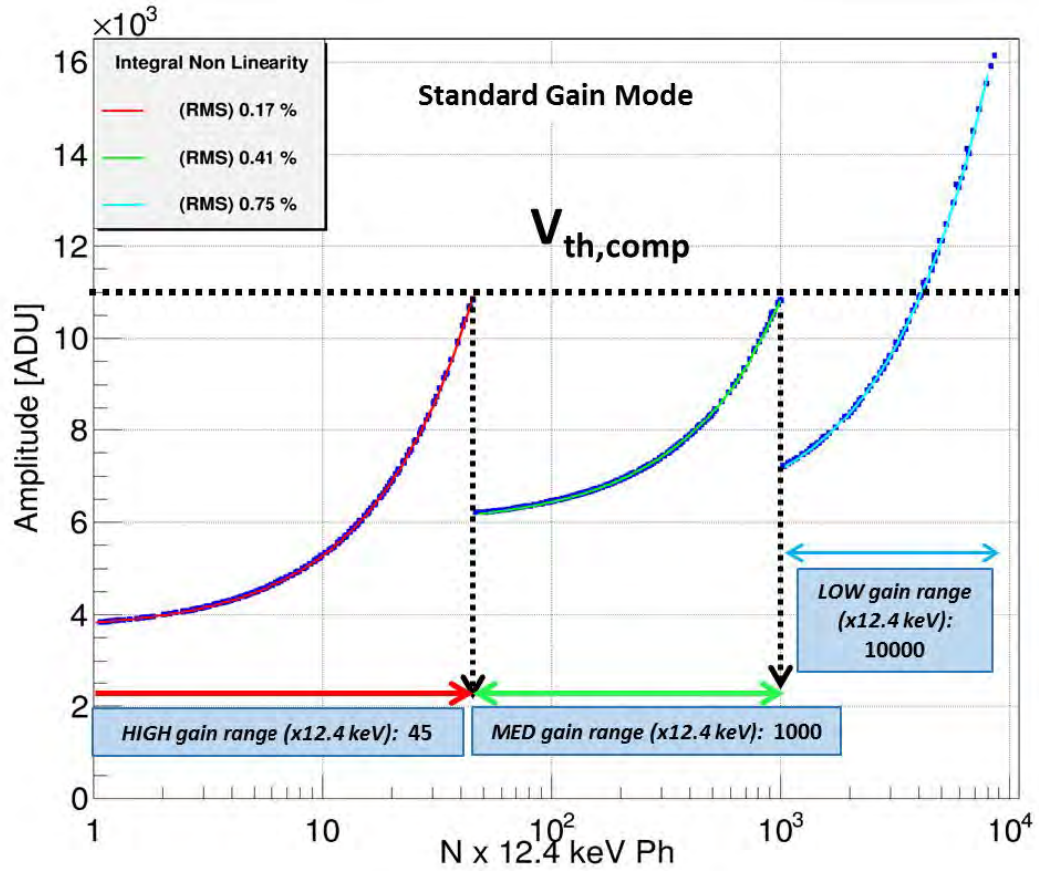


Figure 2.16: Transfer characteristics of the AGIPD detector pixels. The three regions plotted represent the three gain settings of the AGIPD. The gain setting at readout is dependent on incident signal. The dynamic range spans four orders of magnitude at 12.4 keV. Plot adapted from [5].

gain scheme implemented in the AGIPD is powerful, increasing dynamic range much further requires capacitor sizes that may be unreasonable.

Later in this dissertation a pixel architecture will be described which combines the advantages of the AGIPD and the MM-PAD into a single high dynamic range pixel. First however, we aim to demonstrate the importance of dynamic range in x-ray detectors for synchrotron science with some concrete examples.

CHAPTER 3

APPLICATION OF DETECTORS

3.1 Introduction

This chapter discusses an experiment utilizing the MM-PAD, an x-ray detector developed by the Gruner group. The purpose of this discussion is to illustrate the importance of high dynamic range detectors in synchrotron science. The work described here is a diffraction study of uranium dioxide under pulsed magnetic fields conducted at the Advanced Photon Source (APS) experimental hutch 6-ID-C. My collaborators included Zahir Islam from the APS, Jacob Ruff from CHESS, Krzysztof Gofryk and Daniel Antonio from Idaho National Lab, and Kate Shanks from the Gruner group at Cornell University.

Two benefits of high dynamic range detectors will be examined. Higher dynamic range allows for finer temporal resolution and the measurement of small signals which can provide important information that would otherwise be drowned out by larger signals.

3.2 Uranium dioxide background

Nuclear fission of uranium dioxide provides upwards of 20% of the world's power. The thermal conductivity of uranium dioxide governs the conduction of heat produced by fission which is ultimately converted to electricity, and thus understanding this property is vital. While the material has been studied extensively since the Manhattan Project, some elastic and magnetic properties remain

poorly understood. Uranium dioxide exhibits a first order transition to an anti-ferromagnetic state at 30.8 K [55], and abrupt changes in unit cell volume have been observed around this temperature [56]. The material has a cubic lattice (CaF type 2) at room temperature. Unit cell changes at the Néel temperature are theorized to be the result of Jahn-Teller distortions in the oxygen cage around the uranium atoms [57]. Application of strong magnetic fields have been found to amplify these distortions. The coupling of magnetic and elastic properties in uranium dioxide could have profound implications on the present understanding of this material's thermophysical properties.

Bulk measurements have shown that above the Néel temperature magnetic fields applied along the $\langle 111 \rangle$ lattice vector compress the unit cell along this axis and expansion in transverse directions is observed. However, below the Néel temperature the reverse is observed: magnetic fields applied in the $\langle 111 \rangle$ direction induce elongation of the unit cell, and constriction occurs perpendicular to the applied field. Recent studies have found that reversing the direction of the applied magnetic field after cooling the uranium dioxide below the Néel temperature can also reverse the contraction [58]. This behavior is indicative of piezomagnetism which, in addition to magnetostriction, suggests that a magnetic moment can be induced by physical strain on the material. Quantitatively, piezomagnetism implies a linear coupling between a material's mechanical strain and magnetic polarization. Very few piezomagnetic materials are known to exist.

In uranium dioxide, switching of the piezomagnetic behavior occurs at ± 18 T. In practice, the sign of lattice expansion relative to magnetic field direction is set by application of magnetic fields > 18 T in one direction and is only reversed

when fields >18 T are applied in the opposite direction. If this behavior is the result of piezomagnetism, with a coercive field strength of 18 T, uranium dioxide is the strongest piezomagnet ever observed.

The inter-atomic interactions of uranium dioxide are ripe for exploration. Bulk measurements yield net crystallographic properties, but single crystal diffraction is arguably the best way to directly measure unit cell changes. For example, while a net expansion transverse to the $\langle 111 \rangle$ axis has been measured in bulk, whether this is due to a uniform shift in unit cells or twinning of crystallographic grains can not be discerned. Below, an experiment to further investigate these phenomena is discussed. In this experiment, a detector with a high dynamic range is essential to obtain high resolution data of phenomena in pulsed magnetic fields and to discern the fine details of the sample's atomic distortion.

3.3 Experimental design

The experiments described below were conducted at experimental hutch 6-ID-C at the Advanced Photon Source (APS). The APS is a third generation synchrotron source with a 1104 m circumference storage ring described in [59]. Experimental hutch 6-ID-C is fed by an undulator through a double Si $\langle 111 \rangle$ monochromator with a 3.2-28 keV energy range. Energy resolution is $\Delta E/E \approx 10^{-4}$. A 3-stripe vertical focusing mirror with 60 cm active area is used to reject higher harmonic photons and focus the beam to < 1 mm.

3.3.1 Pulsed magnet

The 6-ID-C hutch contains a novel apparatus for collecting diffraction data from a sample mounted in a cryogenic solenoid which is connected to a 10 kV, 500 kJ capacitor bank. Samples can be exposed to pulsed magnetic fields >30 T every ~ 12 minutes with a peak field time > 1 ms. The custom designed solenoid enables x-ray scatter from samples to be collected over a roughly 23.6° arc in forward scatter or back scatter geometries while under maximum magnetic field, as described in [60]. Adjustment of sample position within the magnet allows a larger arc of diffraction to be collected at lower peak fields, but this was not explored in the work described here.

To control the peak magnetic field, and to control the duration of the magnetic field pulse, a choke coil is placed in series between the capacitor bank and the magnet. Capacitor charging voltage can also be used to limit peak magnetic field on a per-pulse basis. The greatest limitation to high throughput data acquisition is the cooling rate of the solenoid. Due to finite impedance of the magnet coils, heat is generated with each pulse. To minimize physical damage to the solenoid the pulse rate is limited.

Samples are cantilevered on a thermally conductive and electrically insulating arm, made of single crystal sapphire, into the bore of the magnet. The arm thermally couples the sample to a closed cycle cryostat which can cool samples to below 10 K. The sample chamber, including the magnet, is sealed. The magnet itself sits in a liquid nitrogen bath which is thermally independent from the sample cryostat. Motors control the translation of the sample in three mutually perpendicular directions and rotation on both axes perpendicular to the x-ray beam. Magnetic fields are applied along the axis of the beam.

3.3.2 Uranium measurements

The sample is a 1mm x 1mm x 500 μ m (height x width x depth from the beam's perspective) single crystal block of uranium dioxide with the $\langle 111 \rangle$ face polished. The sample is mounted with the $\langle 111 \rangle$ surface facing the beam. The magnet is positioned so that the $\langle 888 \rangle$ diffraction condition is met in back-scatter. Beam defining slits set the beam size on the sample to roughly 200 μ m x 200 μ m. The beam flux is 3.5×10^{12} 15.85 keV x-rays/s.

Figures 3.1 through 3.3 illustrate the geometry of the experiment¹. Further discussion of typical diffractometer geometries can be found in many sources. For an overview of the methods used here, see the equatorial and moving-crystal-moving-detector methods described in Chapter 2 of Single Crystal Diffractometry by Arndt [61].

Zero field $\theta - 2\theta$ maps were taken of the sample at 40 K and 14 K to measure lattice constants and verify the expected sample contraction based on previous bulk measurements, roughly ~ 100 micro-strain. Strain refers to the change in a dimension relative to the unstrained dimension. In this case, the lattice constant has changed by 10^{-4} times its original value, 5.47 Å, due to a phase transition at 30.8 K. Figure 3.4 is the $\theta - 2\theta$ map at 18 K. This map is produced by taking images of the sample at a range of sample θ values (angle of the sample relative to the beam). Each image is integrated in the polar angular direction χ (perpendicular to the plane of θ and 2θ , as shown in figure 3.3) to obtain the total diffracted intensity at a given sample θ angle across the range of 2θ angles subtended by the detector. Figure 3.5 is a single frame taken of the uranium dioxide $\langle 888 \rangle$ diffraction peak at 14 K.

¹Figures 3.1 through 3.3 were drawn by Alexandra Westbrook

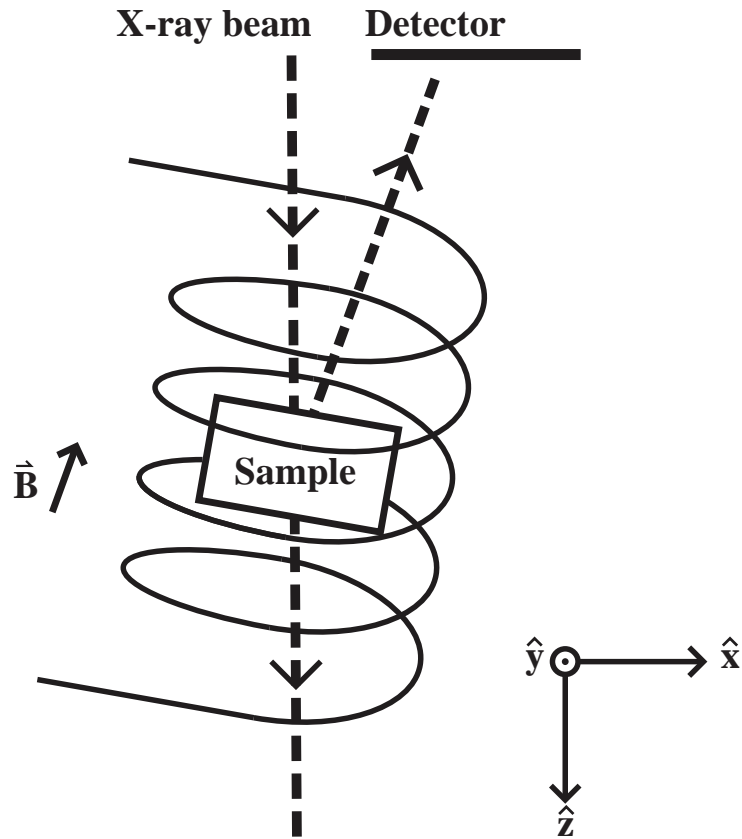


Figure 3.1: The sample is mounted in the magnet and diffraction is collected by the detector in back-scatter geometry. Note that the sample does not rotate independently from the magnet.

Mapping the detector pixels to 2θ values was performed with a silicon calibrant as described in the next section. Compiling the diffracted intensity as a function of 2θ at each sample θ angle, we obtain a map of the intensity in reciprocal space of the sample's electron density throughout the region of interest. The angular shift in the $\langle 888 \rangle$ peak observed between 40 K and 14 K indicates lattice contraction consistent with bulk measurements.

These zero field measurements were taken in a manner intended to mirror the measurements subsequently taken with an applied magnetic field. A Hall effect current sensor measures the current flowing through the magnet, which

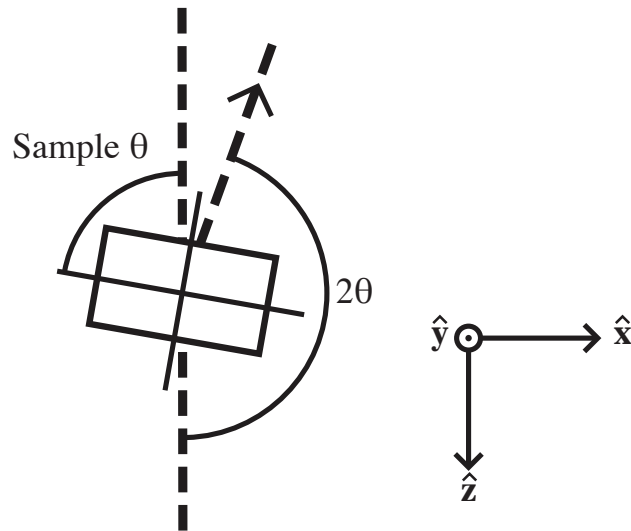


Figure 3.2: Sample θ measures the rotation of the sample relative to the incident beam. 2θ measures the angle of diffraction relative to the transmitted beam.

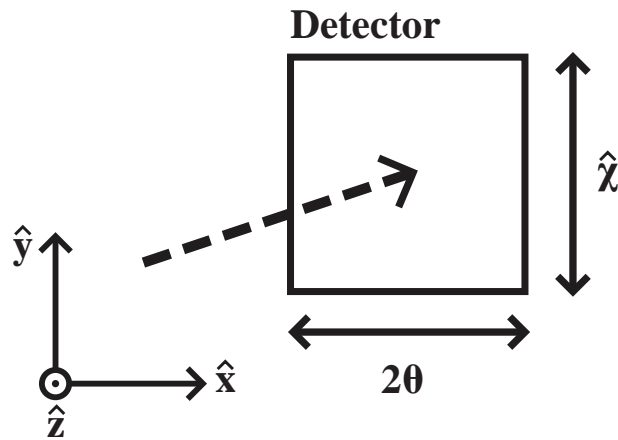


Figure 3.3: Detector pixels are mapped horizontally to diffraction angles (2θ). Detector pixels are summed in the vertical direction (χ) to create the $\theta - 2\theta$ plots referred to throughout this chapter. Due to sample orientation, diffraction primarily occurs in the y-x plane.

is recorded by an oscilloscope. The oscilloscope also monitors the framing of the MM-PAD. In this way, images are mapped to magnetic field values. The MM-PAD recorded images at a rate of 1kHz with an exposure time of $140 \mu\text{s}$. Note that because the magnetic field is constantly changing, each image is a sum

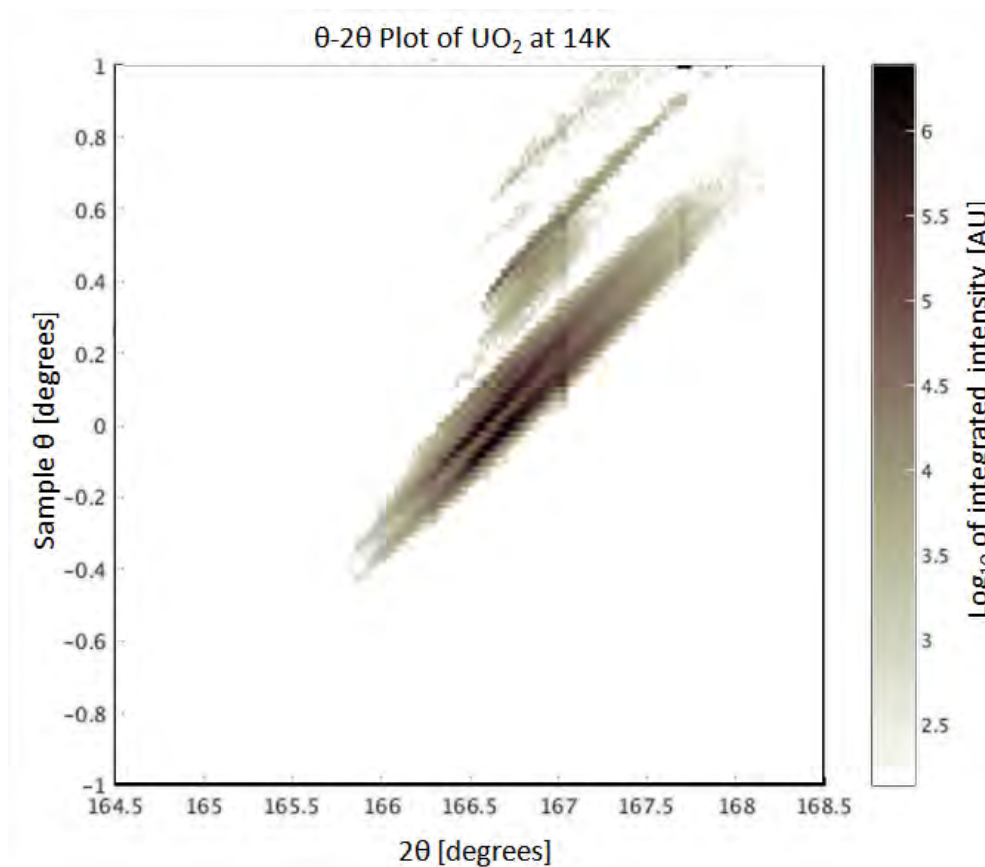


Figure 3.4: Uranium dioxide $\theta-2\theta$ plot measured at zero field and 14 K. The vertical lines in the intensity are artifacts resulting from gaps between the MM-PAD detector modules. This plot serves as a baseline for comparison of diffraction from the sample with magnetic fields applied.

of diffraction from all of the magnetic field values visited during the exposure. In analysis, frames were assigned to the time-averaged magnetic field applied throughout the exposure.

Figure 3.6 plots one magnet pulse versus time with MM-PAD exposures highlighted. Because the gaps in time between frames is large relative to the exposure time, measurements were repeated with an altered delay between the triggering of the magnetic field pulse and the start of MM-PAD framing, sampling more intermediate magnetic field values.

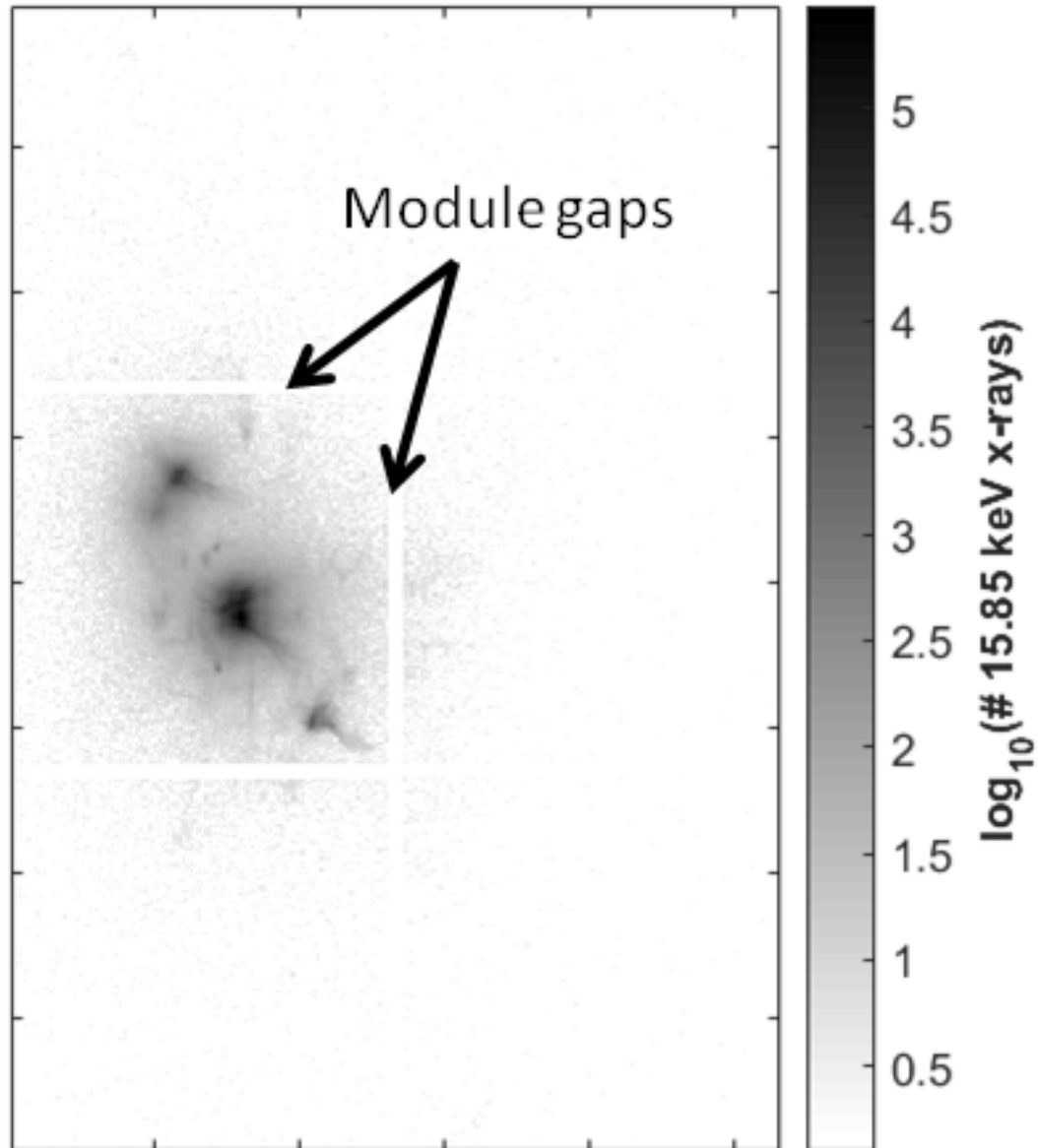


Figure 3.5: Sample frame of uranium dioxide diffraction peak $\langle 888 \rangle$ at room temperature. The color scale is logarithmic and the exposure time was 10 ms. The peak flux is close to the maximum measurable by the MM-PAD. Gaps between the modules of the MM-PAD are also visible.

3.3.3 Azimuthal calibration

To interpret the measured data in this experiment, the detector's position relative to the beam and sample needed to be measured. The calibration process

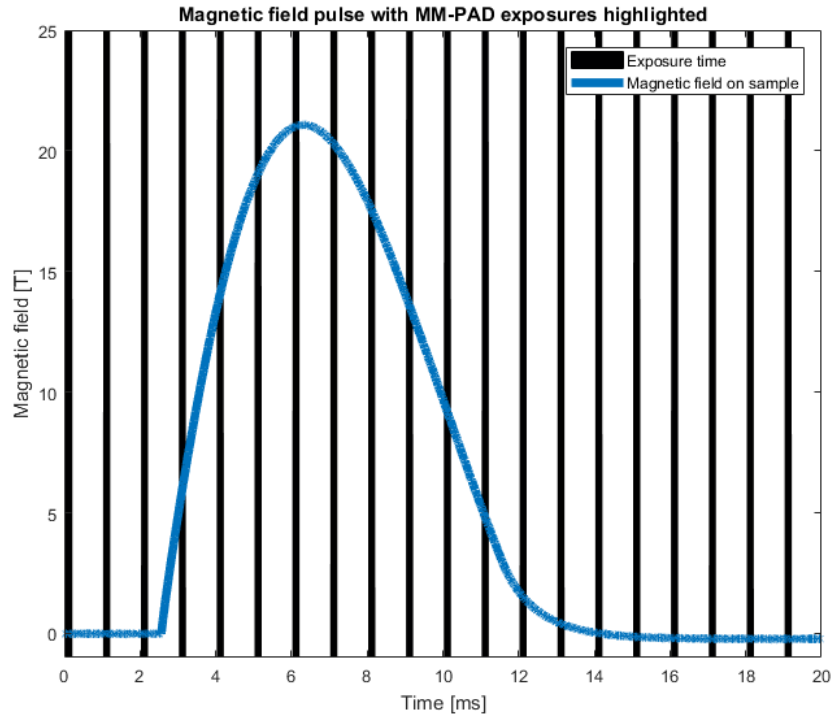


Figure 3.6: Pulsed magnetic field as measured by the Hall current monitor, based on the known inductance of the solenoid. To illustrate magnetic field sampling, MM-PAD exposures are highlighted. Each exposure time was $140\mu\text{s}$.

employed here relies on high quality single crystal silicon. In this case a silicon $\langle 111 \rangle$ monochromator was used. After aligning the sample θ rotation stage's axis of rotation with the x-ray beam, the silicon monochromator was mounted on the rotation stage. The orientation of the silicon is extremely well known, and was rotated such that the $\langle 888 \rangle$ diffraction peak was visible by the MM-PAD with a beam energy of 15.85 keV in back-scatter geometry.

A $\theta - 2\theta$ map of the single crystal silicon was taken through its full rocking curve, and the center of mass of the plot was calculated. The lattice parameter of silicon is well known, and thus the precise angle of diffraction corresponding to the center of mass of the diffraction spot is well known. This can be mapped to a particular point on the face of the MM-PAD to better than a pixel, because

the diffraction spot spans several pixels in the back-scatter geometry.

The energy of the beam was then shifted to 15.99 keV, which also shifts the angle which satisfies the Bragg condition. A second $\theta - 2\theta$ map was taken, and again the center of mass was mapped to a position on the MM-PAD. The spacing between pixels is well known, as this is set by a lithographic process with resolution much smaller than the pixel pitch of $150\mu\text{m}$. With knowledge of the diffraction angles and the points at which the diffraction struck the detector we can obtain very accurate measurements of the distance from the beam to the detector perpendicular to the beam and the distance from the detector to the sample along the axis of the beam, as illustrated in figure 3.7 and calculated below.

The sample to detector distance along the axis of the beam is d_s . The distance between the diffraction spot on the detector and the beam, perpendicular to the beam, is d_1 for the lower energy and d_2 for the higher energy. θ_1 and θ_2 are the complements to the angles of diffraction at lower and higher energy respectively. The distance on the surface of the detector between centers of Si $\langle 888 \rangle$ diffraction is d_p . Note that $d_2 = d_1 + d_p$.

We know that $\tan(\theta_1) = \frac{d_1}{d_s}$ and $\tan(\theta_2) = \frac{d_2}{d_s}$. It follows that

$$\frac{\tan(\theta_1)}{\tan(\theta_2)} = \frac{d_1}{d_2} = \frac{d_1}{d_1 + d_p} \quad (3.1)$$

which allows us to solve for d_1 . Given that the difference d_p was the difference in pixels in only the horizontal direction, this allows us to solve for all of the desired quantities. Furthermore, this provides knowledge of the azimuthal angular coordinate of each pixel on the face of the MM-PAD given the position at which the detector is mounted. Note that by ignoring vertical displacement, we are assuming that the vertical angle of the diffraction is small relative to the

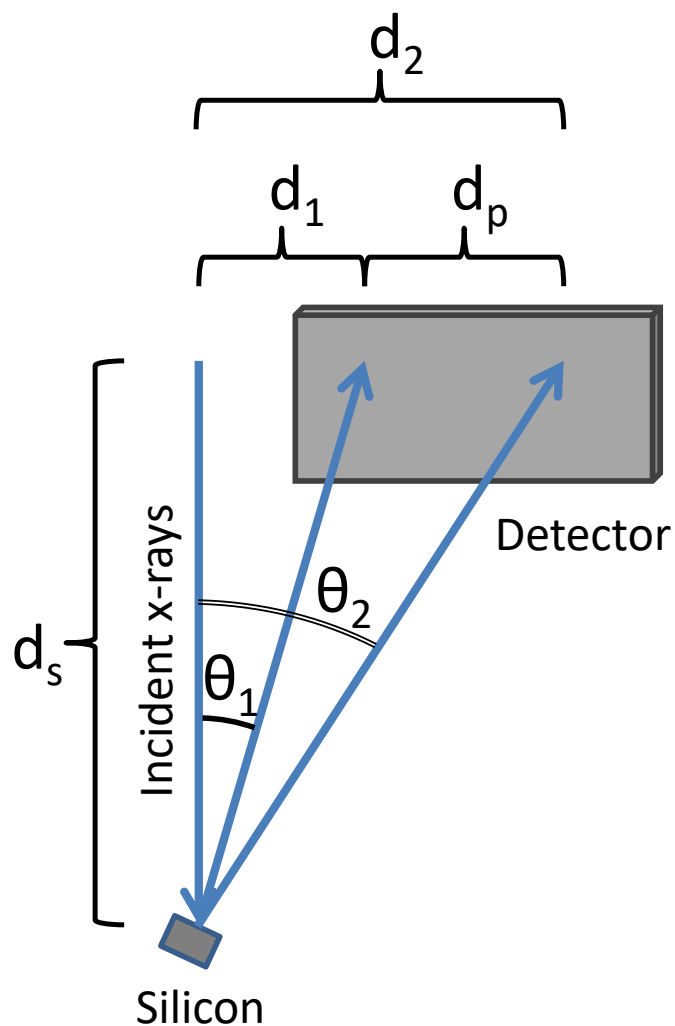


Figure 3.7: Pixel to 2θ calibration geometry. Diffraction from a silicon monochromator is measured with two different x-ray energies and fixed detector position. This allows calculation of the azimuthal angular position of each pixel on the detector surface.

horizontal diffraction, which in this case is true.

This calibration provided an opportunity to verify that the MM-PAD sample-to-detector distance would provide sufficient resolution for the expected measurement. Energies were chosen such that the beam diffracted from Si would shift by the angle expected due to contraction of the uranium dioxide under peak magnetic field. At the sample to detector distance used here (~ 1.5

m) the diffraction center of mass sweeps across forty pixels on the MM-PAD.

3.4 Data analysis

The magnet was pulsed at a set of sample θ positions. Each frame was assigned a magnetic field value according to the oscilloscope measurements discussed above. Sorting frames by magnetic field and sample orientation yields the set of $\theta - 2\theta$ plots in figure 3.8. These plots provide a view of what the uranium dioxide unit cell is doing throughout the magnetic field pulse. Note that more than ten magnetic field values were sampled per pulse, and not all measured magnetic field values are plotted below.

The slight intensity variation in the diagonal direction, along the strips of integrated intensity, are artifacts resulting from much finer sampling in 2θ than sample θ . One sample θ value (position of sample rotation stage) can be sampled per pulse while more than two hundred 2θ values (pixels across the detector) are sampled per pulse. As a result, the axes in figure 3.8 have very different scales and the intensity in reciprocal space appears to jump in 2θ with each step of sample θ .

To more readily interpret this behavior, the $\theta - 2\theta$ plots were collapsed to the sample $\theta = \theta$ line. Bins were drawn with boundaries perpendicular to a line with slope 1/2 in the $\theta - 2\theta$ plots and the sum of integrated intensity in each bin forms one point in the plot in figure 3.9. Each row of this plot shows the intensity in reciprocal space of the uranium dioxide sample along the reciprocal lattice vector $\langle hhh \rangle$. The plot's vertical axis is magnetic field.

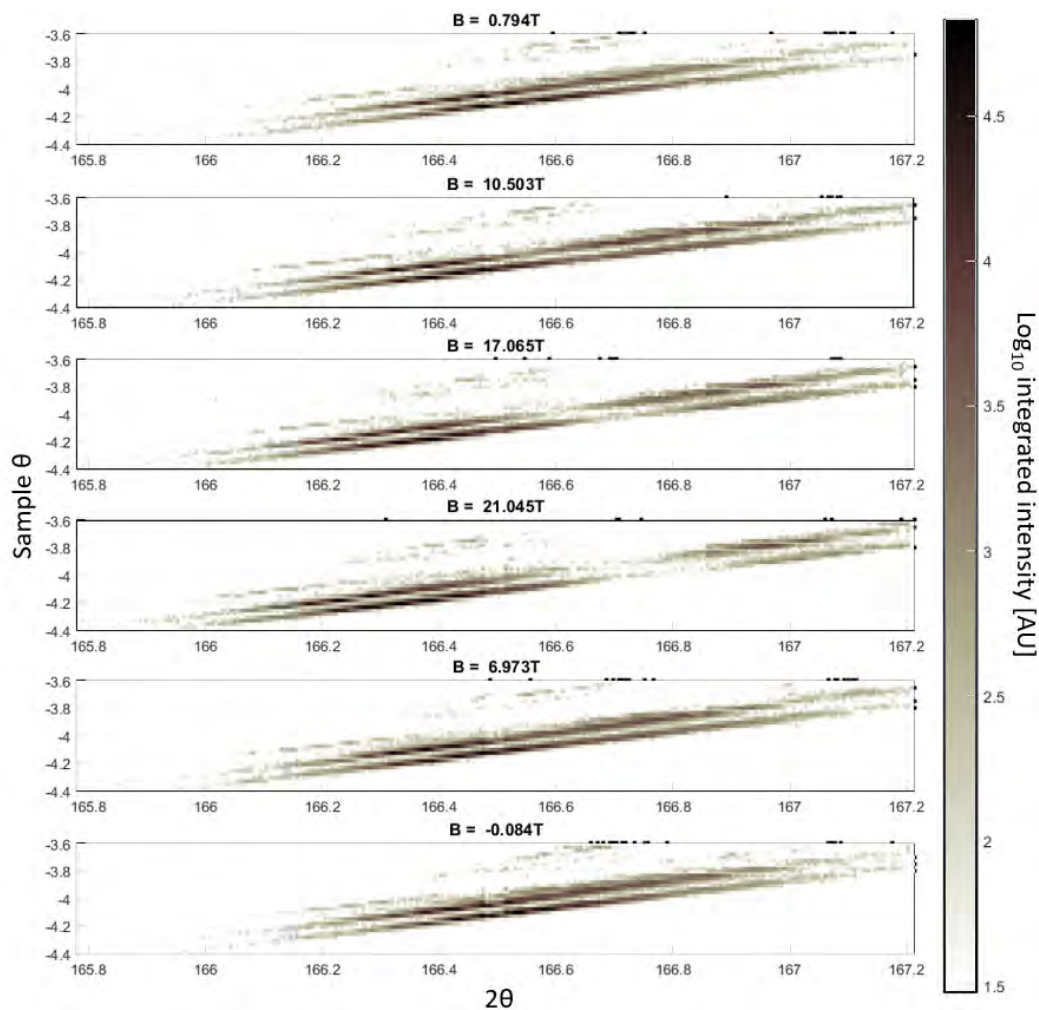


Figure 3.8: A selection of $\theta - 2\theta$ plots of uranium dioxide as a function of magnetic field. Each plot is composed of a separate frame for each sample θ value. Values of 2θ correspond to pixels on the MM-PAD. This depiction illustrates the behavior of electron density in reciprocal space as a function of magnetic field.

Figure 3.9 contains two plots of the same data: the top has a linear scale to illustrate the difference in intensities between what is ultimately two diffraction spots, while the bottom is a log plot in which the dimmer spot is more clearly visible. Both plots illustrate that the majority of diffraction shifts to lower q with higher magnetic field. What was less expected is that the diffracted intensity splits into two separate spots. The less intense of the two spots shifts to higher q , and appears to diminish as magnetic field increases.

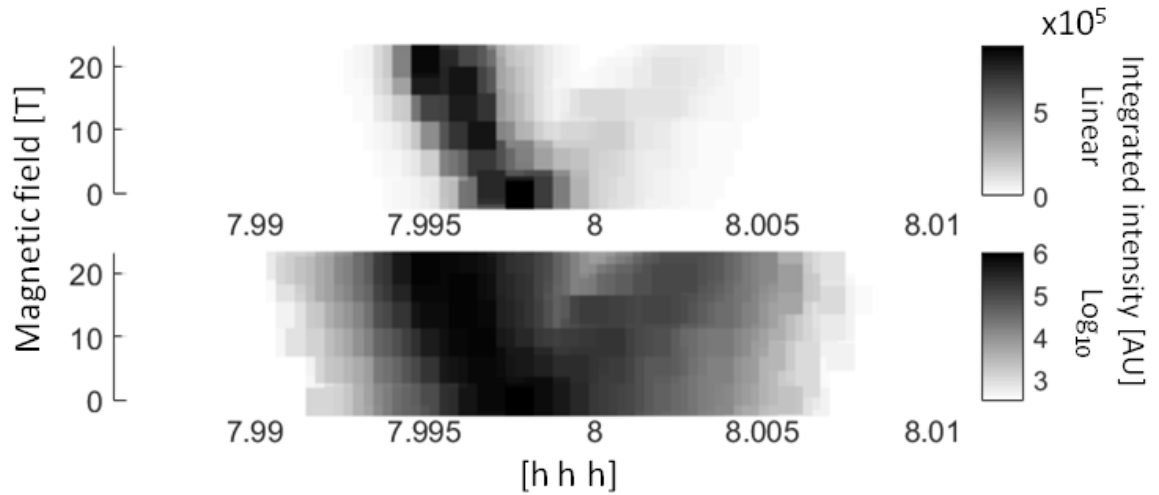


Figure 3.9: Integrated intensity along reciprocal lattice vector $\langle hhh \rangle$ as a function of magnetic field. At zero field a single diffraction peak is seen. The peak shifts as field increases, and a weaker peak diverges from the primary diffraction above 5 T. The plot is formed by dividing $\theta - 2\theta$ plots along the line $\theta = \theta$ into bins perpendicular to this line, spanning the entire dataset. The top and bottom images are the same data. The top plot has a linear scale and the bottom plot has a log scale.

The interpretation of this behavior is not clear, and further studies are needed to discern between possible explanations. One possibility is that two portions of the crystal are behaving differently. This could speak to diverging behavior at grain boundaries. Alternatively, the crystal could be twinning, and the divergent behavior is a result of different orientations of distorted crystal grains. The splitting could also be attributed to a more fundamental structural change. Diffraction is the appropriate tool to differentiate between each of these possibilities, as previous bulk measurements report only the crystal-wide average behavior.

3.4.1 Future work

The experiment described above is ongoing. Recently, high current, high voltage switches have been added to pulsed magnet at the APS experimental hutch 6-ID-C to enable rapid switching of the pulsed magnet polarity. This enables the training of uranium dioxide below 30.8 K with a magnetic field pulse > 18 T in one direction, and subsequently retraining the sample in the opposite direction to investigate potential piezomagnetic effects. Further analysis of the current data, as well as additional data taking to increase the range of 2θ values measured under pulsed fields is being performed.

These techniques are also being applied to new, similar samples. Namely, pulsed magnet work is now being performed on uranium nitride (UN) and uranium antimonide (USb). Each of these samples have shown potential for interesting magneto-elastic behavior of their own. The techniques described above will be expanded on and improved.

3.5 Necessity of high dynamic range

In the experiment described above, greater magnetic field resolution is obtainable through magnetic pulse extension, so that the rate of magnetic field change is lower, or through shorter exposure times. Pulse elongation is possible with a larger choke coil, but this would decrease the maximum magnetic field applied to the sample. Shorter exposure times are also possible, but the measured signal is the exposure time multiplied by flux. The signal to noise ratio must be maintained at a high enough value to resolve the diffraction of interest. Here

the importance of high dynamic range, particularly the ability to measure large instantaneous flux, is clear. In the case of the MM-PAD, the main beam required minor attenuation due to the flux limitation of the detector, as discussed in Chapter 2.

With a higher dynamic range, finer sampling of magnetic field values would be possible resulting in less blurring due to the transient nature of the magnetic field in this experiment. This is related to the case of XFEL experiments on dynamic systems. XFEL pulses with sub-picosecond durations allow dynamic processes to be imaged with commensurate temporal resolution. However, this is only possible if the detector in use can record a sufficient number of x-rays in this time window. In addition to fine magnetic field sampling, high dynamic range is required to perform this experiment in a reasonable time frame. Given that data in this experiment is acquired for 12 milliseconds per 12 minutes, a detector which required more beam attenuation may require multiple pulses to measure a significant signal from each sample orientation. Beam-time at synchrotron sources is a limited resource, and a high dynamic range detector helps to maximize its utilization.

Figure 3.5 depicts a single frame from a zero field scan of the uranium sample. Details in the texture of this Bragg peak can reveal more detailed information about the sample, and is an intriguing direction for future studies. For example, whether separate peaks move together or separately could hint at whether the splitting of diffracted intensity is due to twinning or some other behavior. In any case, these data are only accessible with a high dynamic range detector. Even in the 140 μs exposure times used in this experiment, peak signals of nearly 10^5 x-rays/pixel are measured. Alongside these, the signal from

the secondary diffraction peak are more than three orders of magnitude smaller. While the AGIPD detector could resolve this difference in intensity, it might saturate with the exposure times used here. However, it could utilize shorter exposure times effectively.

On the other hand, a Photon counting detector would experience extreme pileup under these signal rates of $> 5 \times 10^8$ x-rays/pixel/s. To utilize a photon counting detector here, the beam must be attenuated by several orders of magnitude. Note that the dimmer peak in figure 3.9 is more than an order of magnitude weaker than the primary peak. This plot is the sum of many frames, however, and the dimmer peak was often more than three orders of magnitude weaker than the dominant peak in the raw data, depending on sample orientation and magnetic field strength. If the attenuation required to prevent pileup effects in photon counting detectors were used, the dim peak might not be discernible from background scatter at all.

CHAPTER 4

THE HIGH DYNAMIC RANGE DETECTOR CONCEPT

Chapter 3 illustrated the importance of dynamic range to expanding experimental possibilities and fully utilizing synchrotron capabilities. The MM-PAD demonstrates that charge removal circuitry is a valuable tool to extend measurable signal levels when a large, sustained x-ray signal is to be measured. Pushing this metric further would permit better utilization of high brightness storage ring sources. X-ray free electron lasers present a different set of challenges to x-ray detector development.

The AGIPD's adaptive gain, discussed in Chapter 2, is designed to integrate signals from XFELs, which produce high intensity x-ray pulses with durations on the order of femtoseconds. It would seem that charge removal is ill-suited to the problem of integrating large XFEL pulses because no circuitry can respond on femtosecond time scales.

However, the peak photocurrent generated in pixels by XFEL pulses is not quite as dire as femtosecond x-ray pulse durations suggest. While an entire XFEL pulse reaches a detector in the span of femtoseconds, drift, diffusion, and the plasma effect cause the resulting photocurrent to take significantly longer to arrive at pixel integration nodes [62]. Some work has been done in the development of the AGIPD to mitigate this effect. The AGIPD seeks to integrate all of the charge from a single pulse as quickly as possible to achieve higher frame rates [63]. However, it may be possible to utilize the delayed arrival of photocurrent due to the plasma effect in such a way that charge removal circuitry can extend x-ray detector dynamic range at XFEL sources as well as storage ring sources.

This chapter discusses our efforts to characterize the plasma effect and evaluate the possibility of developing an x-ray detector which uses charge removal to integrate very short duration, high intensity x-ray pulses. The detector framework devised and discussed herein is also intended to further extend measurable sustained x-ray flux such that the detector would prove useful at all fourth generation x-ray sources.

4.1 Measuring the plasma effect

The plasma effect refers to the case when a sufficiently large number of electron-hole pairs are generated in a sufficiently small volume of a photo-sensor so as to behave like a plasma cloud. High intensity x-ray pulses can lead to the plasma effect in silicon diodes. An electron-hole plasma expels the photodiode electric field which would ordinarily separate charge carriers and bring them to respective sensor terminals. Instead of the charge cloud being separated in bulk, the surface of the plasma cloud is wicked away by the expelled electric field while the interior of the plasma remains relatively shielded. This slows down the accumulation of photocurrent at pixel integration nodes.

To better understand this process, and to assess the prospect of charge removal operation at XFELs, we have utilized the transient current technique to measure photocurrent transients from a pixelated silicon diode illuminated by a focused infrared laser.

Infrared laser wavelengths were chosen to match the attenuation length of x-ray photons in silicon. For example, 950 nm infrared light has the same attenuation length in silicon at room temperature as 8 keV x-rays. As a result, absorp-

tion of an intense 950 nm laser pulse in a silicon diode produces an electron-hole pair distribution in the sensor which is similar what would be expected from a pulse of 8 keV x-rays. Table 4.1 enumerates several x-ray energies along with their attenuation length in silicon and the IR wavelength with the same attenuation length in silicon. Figure 4.1 is a graphical comparison.

X-ray Energy	Attenuation Length in Silicon	IR Wavelength
2 keV	1.53 μm	547 nm
4 keV	9.68 μm	780 nm
6 keV	30.3 μm	893 nm
8 keV	67.8 μm	950 nm
10 keV	130 μm	992 nm
12 keV	224 μm	1016 nm
14 keV	353 μm	1033 nm
16 keV	521 μm	1046 nm
18 keV	734 μm	1055 nm

Table 4.1: Table listing some x-ray energies, their attenuation length in silicon, and the IR wavelength with a matching attenuation length in room temperature silicon. X-ray attenuation lengths were drawn from the NIST database [64], and IR photon attenuation lengths were drawn from [65].

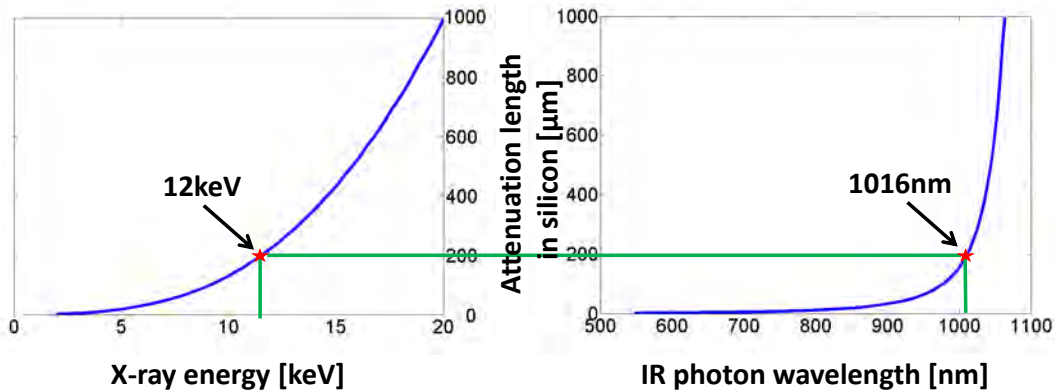


Figure 4.1: Attenuation length in silicon of x-rays (left) matches attenuation length in silicon of IR photons (right). The green line highlights the correspondence of 12 keV photons to 1016 nm photons. In this way, IR laser pulses can simulate XFEL pulses.

We built on previous studies [66], increasing the laser intensity employed by two orders of magnitude, to investigate the delay of photocurrent collection due

to the so-called plasma effect. We hope to maximally exploit this mechanism, extending charge collection times of femtosecond XFEL pulses to microseconds. This extended pulse duration may allow for charge removal techniques, perhaps modifications of the technique employed in the MM-PAD, to be used at XFELs.

4.1.1 Experimental apparatus

¹ Data was collected by focusing a tunable, pulsed IR laser (EKSPLA PT259-AO-H) to a $5 \pm 1 \mu\text{m}$ rms spot on a custom diode modeled after the variety intended for use with the HDR-PAD which is described in the next subsection. Figure 4.3 depicts the experimental apparatus and beam path. The laser pulse duration was 10.5ps FWHM as measured by the manufacturer. The laser was equipped with a pulse picker which enables a user defined pulse repetition rate below the laser's natural 1MHz rate. The tunable wavelength range was 700 nm – 1050 nm with a line width between 0.18 nm – 0.36 nm. The precise line width varies throughout the wavelength range of the laser.

As mentioned above, the purpose of a selectable wavelength is to simulate x-rays of different energies. Computational simulations were performed to ensure that the finite line width (FWHM of the power spectral density) of the laser would be sufficiently small, assuming a Gaussian distribution of wavelengths in the pulse. Figure 4.2 plots the generated hole density of a simulated laser pulse in one micron slices of a silicon sensor versus sensor depth for a 1016 nm laser pulse. A larger line width, particularly at longer wavelengths where the

¹Dr. Julian Becker provided invaluable assistance in developing this apparatus and performing these measurements.

attenuation length in silicon of IR photons changes more rapidly as a function of wavelength, leads to electron-hole pairs being created at different depths in the sensor than intended. Based on these simulations it was determined that a sub-nanometer line width had a negligible effect on the distribution of electron-hole pairs in the sensor.

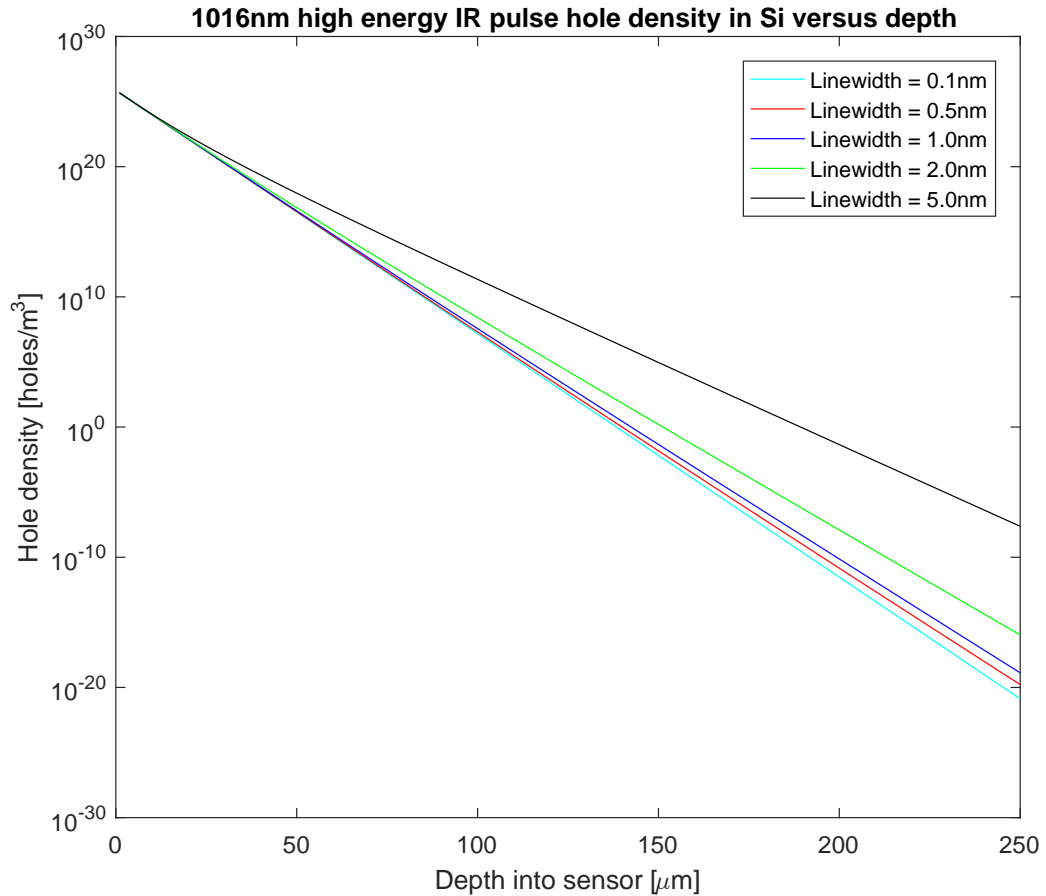


Figure 4.2: Simulated hole density created in one micron slices of a silicon sensor as a function of depth into the sensor for a laser pulse of 1016 nm wavelength photons with various spectral distributions at normal incidence. The laser pulse was simulated with 6 μ m pulse radius and 10¹¹ eV pulse energy at room temperature.

The maximum pulse energy was > 10⁷ keV. Pulse-to-pulse energy variations were measured with a 1% silvered mirror which directed a fraction of pulse energy to an ancillary diode, hereafter referred to as the beam-split diode. The

beam-split diode read out its measured transient alongside the main pulse signal transient to a DPO 7254C oscilloscope with a 2.5GHz bandwidth. The beam-split diode was calibrated with J-10GE-LE Quantum EnergyMax pyroelectric laser pulse energy meter. The pyroelectric pulse energy meter produces a voltage pulse in response to a change in sensor temperature due to incident laser pulses. The energy meter selected is NIST calibrated and serves to pair beam-split diode measurements with absolute pulse energies. During calibration, the pyroelectric energy meter was placed at the sample diode location. By taking a series of measurements with both the beam-split diode and the energy meter, the correspondence between beam-split measurements and actual pulse energy arriving at the sample was measured.

The beam path consists of the aforementioned 1% silvered mirror followed by a filter wheel. The filter wheel allowed larger variations in pulse energy to be explored, but no filter was used when measuring peak pulse energy photocurrent transients. The filter wheel is followed by a Galilean telescope to expand the pulse to the subsequent achromatic doublet lens's full aperture to maximize beam focusing. The target diode and support electronics were mounted on translation stages which were controlled by the same computer which controlled the laser, permitting parametric scans.

Target photodiode

A custom diode array was designed to read photocurrent transients directly to an oscilloscope while mirroring the sensors used in previous x-ray detectors built by our group as closely as possible. The diode array is 500 μm thick n-type high resistivity silicon with a 120V depletion voltage and 150 μm \times 150 μm pixel

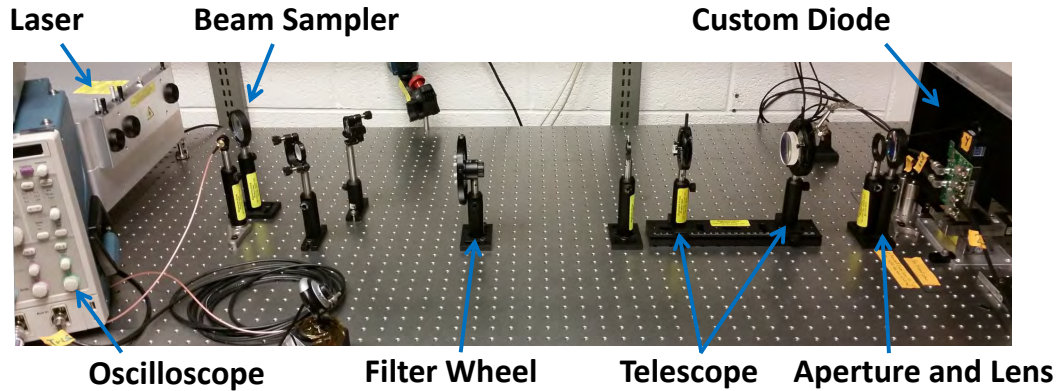


Figure 4.3: Laser beam path for transient current technique studies. The pulsed infrared laser is controlled by a computer (not shown) which coordinates the oscilloscope readings. Laser pulses pass through a beam sampler which consists of an 1% silvered mirror at 45 degrees to the beam path. A dedicated diode reads the fractional pulse to record pulse-to-pulse energy variations. The main pulse then passes through a filter wheel which enables large scale pulse intensity variation. The pulse is subsequently expanded through a Galilean telescope to permit tighter focus by the achromatic doublet lens. The focused pulse is absorbed by a custom silicon photo diode and the photocurrent transient is routed to the oscilloscope through a custom PCB. The main pulse transient and split pulse transient are read by the oscilloscope to the data acquisition computer.

pitch. The pixelated structure of the diode enabled measurement of the lateral diffusion of the charge cloud.

The diodes employed in Gruner group x-ray detectors are biased by application of a high voltage via an aluminum layer on the x-ray entrance side. This layer is essentially transparent to x-rays, but would be significantly more opaque to infrared photons. As such, an opening in the aluminum above target pixels was required. The diode included four target pixels below the aluminum opening in a 2x2 square. These target pixels were surrounded by several rings of non-target pixels. In a pixelated sensor, the uniformity of voltage across adjacent pixels is essential. If adjacent pixels are held at different biases, charge deposited above one pixel may enter another, resulting in image distortion. In this customized diode, it was necessary to maintain voltage control of

non-target pixels. Non-target pixels were ganged together by uniform back-side aluminization which could be biased by a single wire bond. Because no ASIC layer was being designed to accompany the sensor, photocurrent of interest was to be routed through wire bonds to support electronics. Each of the four target pixels was individually wire bonded.

Wire bonds were made to a custom printed circuit board (PCB). The PCB to which the sensor was wire bonded also provided the high voltage bias. The PCB was designed by Dr. Julian Becker with a metal lined hole to which the entrance window of the target diode was attached with silver paint. The high voltage bias was supplied through the hole's metalization and laser pulses struck the target pixels through the hole in the PCB. Circuitry on the PCB capacitively coupled target pixels to an amplifier which fed measured transients to an oscilloscope. Schematics for the PCBs employed in this work are contained in Appendix A.

While measuring the incident photocurrent, slight variation in the target pixels' voltages were unavoidable, but a bias-tee, consisting of a connection to the bias voltage through an inductor, and a connection to the readout amplifier through a capacitor, ensured that the pixel would quickly return to an AC ground. Similar bias-tees were used to bias non-target pixels and the sensor. These signals were also measured. Photocurrent transients were terminated with 50Ω and measured by a Tektronix DPO 7254C oscilloscope. All lines were terminated with 50Ω to minimize the impact of reflections on signal lines.

4.1.2 Transient current analysis

A single IR photon in the wavelength range studied here does not have sufficient energy to create an electron-hole pair in silicon. As a result, absorption of IR photons in silicon is phonon assisted, and in subsequent analysis, it is assumed that each IR photon creates one electron-hole pair. Studies of high intensity sub-band gap radiation incident on silicon have noted a power dependence in the absorption of photons in silicon and the onset of significant nonlinear effects such as two-photon absorption [67]. Optical nonlinearities are often characterized by the Kerr coefficient, in silicon for IR photons is on the order of 10^{-18} m²/W [68]. The present experiment utilizes a peak laser power on the order of 40 watts with a spot size of roughly 36 μm^2 . This suggests that changes in the index of refraction of silicon during absorption of the laser pulses used here are on the order of 10^{-6} and so these nonlinear effects should be negligible.

In comparing IR pulse energy to x-ray pulse energies, it is thus necessary to calculate the number of IR photons in a given pulse. This is done by first assuming that the pulse is monochromatic. Given the small line width of the laser employed, this is a reasonable assumption. The absolute energy of the laser pulses used here were calibrated as described in the section above. With the absolute energy known and monochromaticity assumed, the number of photons in a given pulse is simply the pulse energy divided by the energy of a single photon, $\frac{hc}{\lambda}$. We then assume that this is the number of electron-hole pairs created in the silicon diode by this pulse. By matching the attenuation length of the IR pulse wavelength to that of an x-ray energy, we divide the x-ray energy by 3.6eV (the energy required to create an electron-hole pair in silicon), and divide the number of electron hole pairs created by the IR pulse by this number

to arrive at the equivalent x-ray pulse energy.

Because the plasma effect is a function of illuminated volume, laser spot size needed to be measured. The opening in the target diode high voltage biasing aluminization which allowed IR pulses to strike target pixels, described in the previous section, provided a convenient knife edge with which to measure the laser pulse profile. By translating the target diode perpendicular to the incident beam while collecting pulse data from target pixels, such that the aluminization blocks part of the incident pulses, we can plot a curve which is the signal measured by the target pixels as a function of pulse position. The derivative of this curve tells us the laser intensity that is cut off from the target pixels by the high voltage aluminization with each translation step. This provides a reconstruction of the lateral pulse profile. Figure 4.4 is a plot of one of these scans with a one micron step size and a Gaussian fit to the data. The fitted standard deviation is $< 6\mu\text{m}$. To obtain information longitudinal to the beam, which includes information about pulse focusing, this procedure was performed at various lens-to-diode distances.

Photocurrent transients from XFEL-like pulses have the characteristic shape illustrated in Figure 4.5, which is an average of one hundred 950 nm photocurrent transients from laser pulses which create electron-hole pair distributions similar to 10^6 8 keV photons, measured with 200V sensor bias. Generally speaking, photocurrent arrives in two phases: an initial spike arising largely from induced current [69] followed by a long tail as charge carriers drift to the sensor terminals. In the transient plotted, roughly 10% of total deposited charge arrives in the spike followed by a tail photocurrent roughly equivalent to that produced by 10^{11} 8keV x-rays/s. However, these numbers vary significantly based on fac-

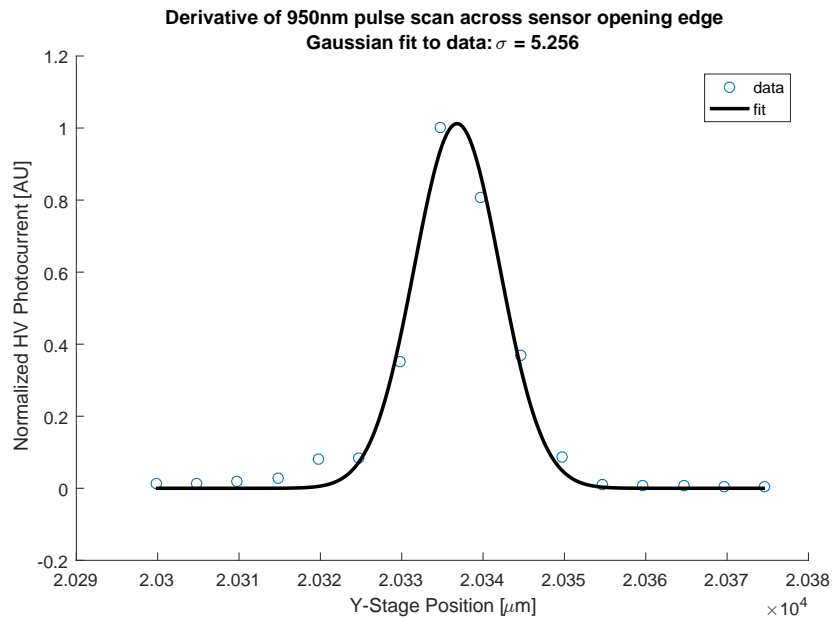


Figure 4.4: Gaussian fit to derivative of lateral translation scan of target diode with 950nm laser incident. The fitted line describes the laser pulse profile in one dimension perpendicular to the beam path.

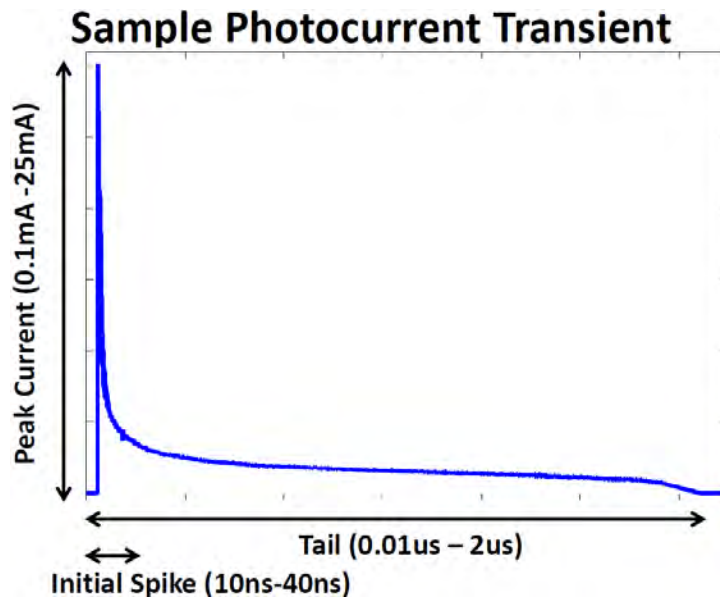


Figure 4.5: Characteristic shape of photocurrent transients produced by high intensity pulses ($> 10^4$ x-rays). The transient above is an average of one hundred 950 nm pulses (equivalent to 8 keV attenuation length) with a mean single pulse energy equivalent to 10^6 8 keV x-rays. The sensor was bias was 200 V.

tors including photon energy, area illuminated, and sensor bias, among others. Pulses of lower energy x-rays and higher intensities create denser electron-hole pair clouds leading to a larger fraction of deposited photocurrent arriving in the tail portion. Lower diode bias voltages extend charge collection times further. The charge collection times measured are still significantly shorter than recombination times in silicon. Pulses equivalent to $< 10^3$ x-rays are collected completely in 10-40 ns, appearing as only a spike, while focused pulses equivalent to $> 10^4$ x-rays produce photocurrent tails that can take microseconds to be collected by pixels.

Figure 4.6 is a plot of the normalized integral of photocurrent arriving at a pixel versus integration time for three pulse energies with wavelength 1016 nm (12 keV equivalent attenuation length). For reference, the integrated charge versus time of a low intensity pulse (equivalent to $< 10^3$ x-rays, simulated from previous work [66]) with negligible plasma effects is plotted alongside the data. Integrals are normalized to the total charge integrated by the monitored pixel, which differs from the total charge created by the pulse due to lateral charge spread. Pink dots denote the point at which charge equivalent to 10^4 x-rays has been integrated. Even for a pulse equivalent to only 6×10^4 12 keV x-rays, charge equivalent to 10^4 x-rays is integrated within 5 ns of pulse onset.

Figure 4.7 demonstrates how durations of transient tails increase as a function of total pulse energy for three x-ray energy equivalents. Charge collection of 8 keV x-ray equivalent pulses occurs over significantly longer time scales than higher x-ray energy equivalent pulses. This is because the attenuation length of 8 keV x-rays in silicon is significantly shorter than that of 10 keV or 12 keV x-rays. As a result, charge is deposited in a much smaller volume of the

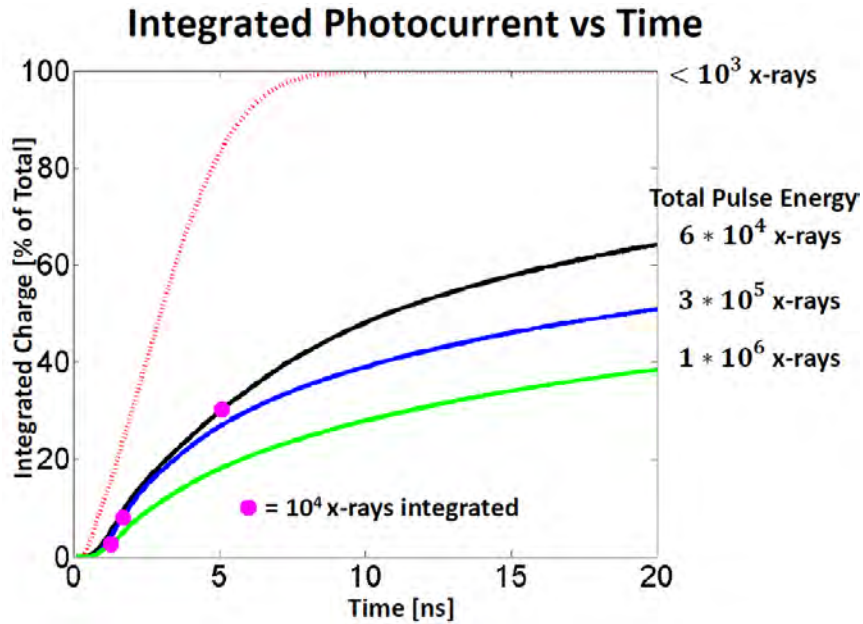


Figure 4.6: Normalized integrated charge versus integration time of 1016 nm (12 keV equivalent attenuation length) pulses at three pulse energies. The red dotted line is a low energy pulse ($< 10^3$ x-rays, simulated from previous work [66]) for reference. Sensor bias was 200 V.

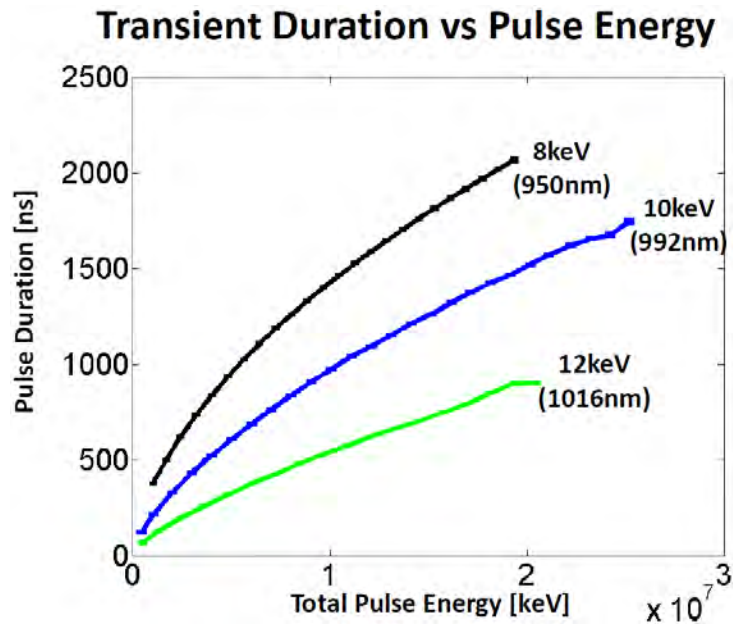


Figure 4.7: Average pulse duration as a function of total pulse energy at three wavelengths. Pulse durations were measured as time above two times the standard deviation of background noise. Sensor bias was 200 V.

sensor, leading to denser electron-hole pair clouds and therefore more persistent plasma effects. Charge collection times of 12 keV equivalent IR pulses do not reach more than 1 μs with the spot size and pulse energies tested here, but the charge collection times measured are still significantly longer than the laser pulse duration.

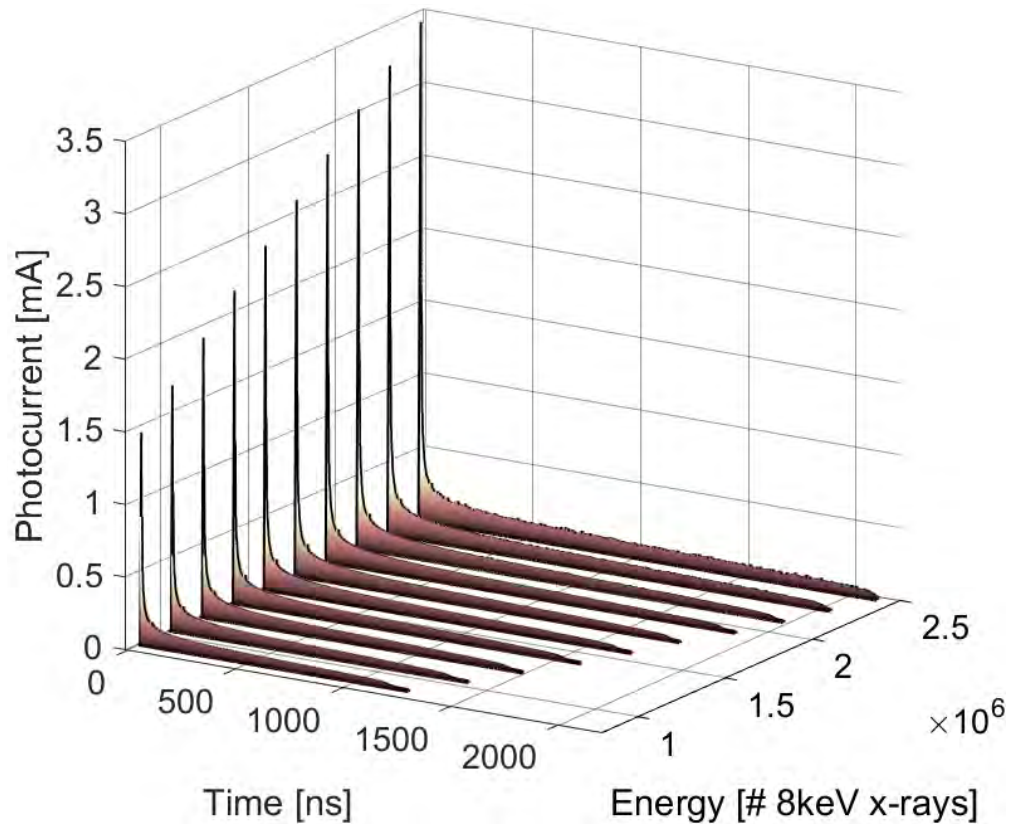


Figure 4.8: Averaged photocurrent traces from 950nm laser pulses focused to 6 μm incident on a 500 μm thick silicon diode. The diode bias was 200 V.

Figure 4.8 shows plots of averaged photocurrent transients from a range of 950 nm pulse energies versus time. The plasma effect is evident in the dependence of charge collection time on pulse energy.

4.1.3 Conclusions

Figure 4.5 is an average of one hundred 950 nm pulse photocurrent transients with a mean pulse energy that produced electron-hole pairs equivalent to 10^6 8 keV x-rays. This profile is characteristic of all measured pulses which exhibited signs of the plasma effect. Overall, the charge collection profile is extremely sensitive to wavelength, spot size, and pulse energy. However, some conclusions can be drawn.

The plasma effect is most pronounced for lower energy x-ray equivalents which produce denser plasma clouds. Thus, the strategy of using plasma clouds to slow charge arrival is more promising for 8 keV x-ray pulses, compared to the other x-ray equivalents tested here. Charge collection times for sufficiently focused pulses do extend to microsecond time scales. Despite the extended charge collection time, significant photocurrent still arrives in the initial spike and may prove problematic for pulse energies greater than 10^6 8 keV x-rays.

A strategy to integrate pulses of this nature may be possible and might involve adaptive gain handling integration of the initial photocurrent spike and charge removal circuitry handling the drawn out tail. While in-pixel charge removal techniques are not fast enough to act on femtosecond time scales, we have shown that photocurrent from large pulses can arrive over microseconds, a time scale on which MM-PAD style charge removal techniques may prove useful.

4.2 Adaptive gain and charge removal combined

The "spikes" measured in the IR laser pulse photocurrent transients above deposit too much charge in pixels too quickly for a charge removal scheme to accurately record signals. An adaptive gain scheme is capable of measuring these signal bursts, but the full well of an adaptive gain pixel is ultimately limited by integration capacitor size, and therefore, pixel size. The full well scales linearly with these quantities. The charge removal of the MM-PAD achieves a full well that is limited by the depth of a digital counter, which doubles with each successive bit added. The tradeoff is of course that photocurrent integration now has a rate limitation.

Combining an adaptive gain scheme with a charge removal scheme similar to that of the MM-PAD provides two primary benefits. First, the "spike" of intense x-ray pulses can be integrated by the adaptive gain circuitry. As seen above, the majority of signal charge arrives over a longer time scale, perhaps long enough for charge removal circuitry to operate. If this tail arrives after adaptive gain circuitry has already activated, it is possible to use a larger charge removal capacitance. The maximum flux measurable by one MM-PAD pixel in its present form is

$$\Phi = \Delta V * C_{rem} * f / q_x \quad (4.1)$$

where Φ is the maximum flux, ΔV is the voltage difference between the front end voltage and V_{low} , C_{rem} is the size of the charge removal capacitance, f is the maximum frequency of charge removal, and q_x is the number of electron-hole pairs created per x-ray. C_{rem} should not exceed C_{int} , the integration capacitance, or charge removal could result in pulling the integrator out of its operating range and produce erroneous measurements. Adaptive gain allows

C_{rem} to be increased by several orders of magnitude by virtue of C_{int} increasing step-wise, thus increasing the maximum flux measurable by a pixel employing charge removal.

In addition to possibly integrating XFEL like pulses studied in this chapter, combining adaptive gain with charge removal allows pixels to integrate a significantly higher sustained x-ray flux. This capability would be exceedingly useful at high brightness storage ring sources. Chapter 5 will outline several pixel architectures which utilize both adaptive gain and charge removal circuitry. An ASIC with pixel test structures pursuant to this strategy was fabricated, and their testing is discussed.

CHAPTER 5

PIXEL SUBSTRUCTURE TESTING

Combining charge removal with adaptive gain could increase the dynamic range attainable by a pixel array detector at XFELs and high brightness synchrotron sources by several orders of magnitude. To roughly estimate the potential gains, consider the performance of the MM-PAD, described in Chapter 2. The MM-PAD is capable of measuring a sustained flux of 10^8 8 keV x-rays per pixel per second. With an adaptive gain front-end increasing the integration capacitance by, say, a factor of 25, the charge removal capacitance can be correspondingly increased, resulting in a factor of 25 higher sustained flux limit. It may also be possible to increase the maximum rate of charge removal, which would further extend this limit. A factor of 4 increase in the rate of charge removal would result in a net sustained flux 100 times higher than the MM-PAD. As seen in the previous chapter, such a pixel could potentially measure high intensity XFEL pulses as well.

Extending the performance of a pixel array detector pixel is not trivial. For example, increasing the maximum rate of charge removal too much will result in incomplete elimination of integrated charge, and thus produce an unreliable measurement. Furthermore, the MM-PAD relies on holding the front-end at a fixed voltage to ensure the uniformity of charge removal operations. To achieve this, the front-end amplifier will have to respond quickly to large signals with a correspondingly high slew rate.

To examine the feasibility of a detector utilizing both adaptive gain and charge removal in the same pixel, an ASIC was fabricated with several prototype pixel front-end architectures in TSMC 180nm mixed signal general-

purpose II 1P6M salicide technology with $2 \text{ fF}/\mu\text{m}^2$ MIM-caps and thick top metal through Europractice.¹ This chapter discusses these prototype pixel designs and their ability to integrate high currents. Chapters 6 and 7 discuss a 16x16 pixel, fully functional pixel array detector constructed with pixel architectures based on the designs discussed below.

The work discussed here was a collective effort. While all team members worked together, the majority of developmental work on particular components can generally be attributed to particular scientists. The MM-PAD 2.0 pixel was developed by Dr. Katherine Shanks, the charge dump oscillator was developed by Dr. Hugh Philipp, and I developed the capacitor flipping pixel. FPGA programming to orchestrate the chip's operation was written by Prafull Purohit and the support electronics were designed and laid out by Darol Chamberlain. Dr. Mark Tate and Professor Sol Gruner were also instrumental in the development of these structures.

5.1 Pixel architectures

This section discusses the concepts and architectures of three pixels that were designed. The test ASIC discussed in this chapter generally featured only the pixel front-ends, excluding components such as digital counters and analog readout chains. In two cases, adaptive gain was not included, but the integration capacitance was chosen to simulate the low gain stage of an adaptive gain system. A full adaptive gain system was omitted in these pixels to test

¹At the time of the writing of this dissertation, all relevant design files are located on the Gruner group server "People" in directory `/us/Detectors-EssentialInformation/HDR-PAD/HDR-PAD_Sub1/`.

new charge removal strategies with minimal extraneous complications. It will be made clear which components were fabricated in each case. The pixel components were connected to probe pads at various points to permit examination of the inner workings of the components. A probe pad on the integration node of each pixel was used to inject current directly into the pixel input, simulating an x-ray photocurrent signal. Pixel performance is discussed below.

5.1.1 MM-PAD 2.0

The first pixel architecture (MM-PAD 2.0) is a scaled version of the original MM-PAD and is depicted in figure 5.1. In contrast to the MM-PAD, the MM-PAD 2.0 incorporates adaptive gain, as demonstrated previously by detectors such as the AGIPD [4]. The MM-PAD 2.0 charge removal circuit will not trigger unless the lowest-gain stage has been engaged. This allows the use of a larger charge removal capacitor than in the original MM-PAD, thereby increasing ΔQ , the charge removed with each execution of the charge removal circuitry. In the readout ASIC discussed here, 6 combinations of total feedback capacitance and charge removal capacitance were tested. Charge removal capacitors ranged from 440fF to 2630fF with equal or greater total integration capacitance in each case. Larger charge removal capacitors allow a pixel to integrate higher photocurrents by increasing ΔQ . The range of capacitance employed allowed examination of the maximum integration and charge removal capacitance which would function adequately.

Charge removal capacitors of 1800fF and 2630fF (with matched integration capacitors) exhibited incomplete charge removal at the maximum oscillator fre-

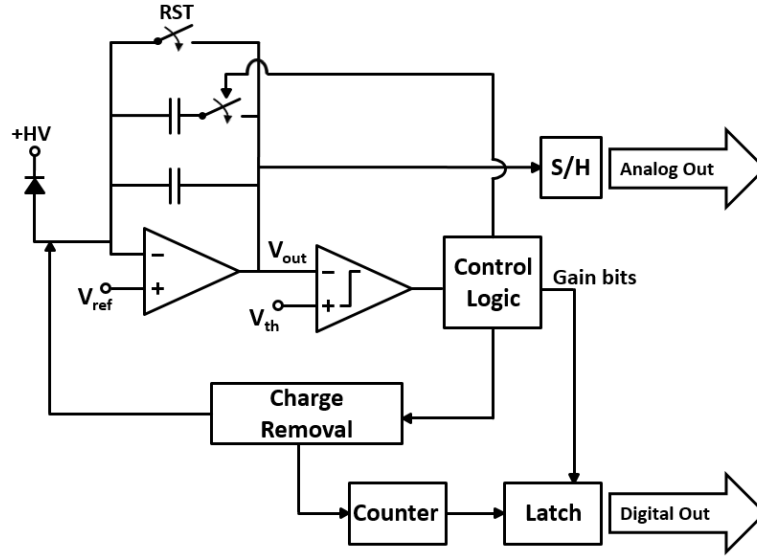


Figure 5.1: Simplified MM-PAD 2.0 schematic. Control logic box engages adaptive gain prior to enabling switched capacitor charge removal.

quency, 100MHz_z . Based on simulations, this is most likely due to the RC constant of the charge removal circuit, which increases with the size of the charge removal capacitor. A version of the pixel with a total maximum feedback capacitance of 2630fF and a charge removal capacitance of 880fF exhibited the most robust performance. The results presented in this chapter are from this variant. The high-gain stage has a feedback capacitance of 40fF , small enough to resolve the signal from one 8 keV x-ray. To increase measurable sustained flux further, the maximum frequency of charge removal has been increased by a factor of 50, to 100 MHz_z .

Integrating high flux signals requires commensurate amplifier slew rates. The integrating amplifier of the MM-PAD 2.0 is a class AB operational transconductance amplifier based on [70]. This topology was chosen for its high current output, boosted by local common-mode feedback, rapid settling time, and relatively low power consumption. Section 5.2 contains a detailed discussion of the amplifier architecture. The comparator employed is asynchronous and opti-

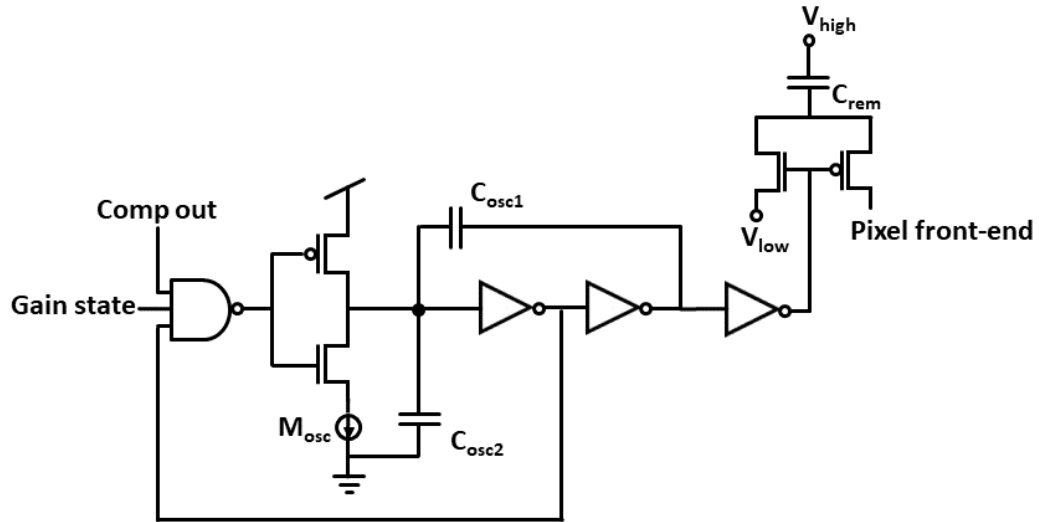


Figure 5.2: MM-PAD 2.0 gated oscillator and charge removal switched capacitor block level schematics.

mized for response time. It is composed of a five transistor differential amplifier driving an inverter. These components varied only slightly between the three pixel architectures discussed in this chapter.

The pixel components fabricated in this test ASIC include the front-end integrating amplifier with full adaptive gain and charge removal circuitry. Charge removal control signals, adaptive gain control signals, and comparator output were connected to probe pads for external measurement alongside the integrator analog output and front-end voltages.

MM-PAD 2.0 charge removal

The charge removal circuitry, depicted in figure 5.2, consists of a gated oscillator which toggles a switched capacitor to remove charge from the integration node (pixel front-end). The gated oscillator pulse width and maximum frequency is set by $C_{osc1,2}$ and the tunable current mirror M_{osc} . C_{osc1} and C_{osc2} are equal sized

capacitors. It is the same topology as the original MM-PAD. When the comparator activates the NAND gate, the C_{osc} capacitors begin charging. Once its voltage passes the inverter threshold, the inverters connect C_{rem} to the pixel integration node and C_{osc} begins discharging. Once the capacitors $C_{osc1,2}$ have discharged, the charge removal signal is brought low again. The charge removed per oscillator pulse is

$$\Delta Q = C_{rem}(V_{ref} - V_{low}). \quad (5.1)$$

The MM-PAD 2.0 can tolerate larger photocurrent spikes (integrating $> 10^3$ x-rays before relying on charge removal) and larger sustained photocurrents than the original MM-PAD.

5.1.2 Charge dump oscillator

The charge dump oscillator (CDO) pixel design aims to scale the rate of charge removal with the rate of charge arrival by combining the charge removal switched capacitor with the oscillator driving it. Depicted in figure 5.3, the frequency of charge removal is set by the propagation of digital signals in the ring oscillator and the charging rate of the removal capacitor, C_{rem} . When a comparator indicates that a threshold has been crossed, the oscillator is activated and C_{rem} connects to the integration node. Once C_{rem} has charged to the switching threshold of the adjacent inverter, the capacitor is detached and the charge accumulated onto it is dumped to ground. The faster C_{rem} charges while attached to the front-end, the faster charge is removed.

In addition to one comparator monitoring the integrator output, as in the MM-PAD, a second comparator monitors the pixel front-end voltage. Charge

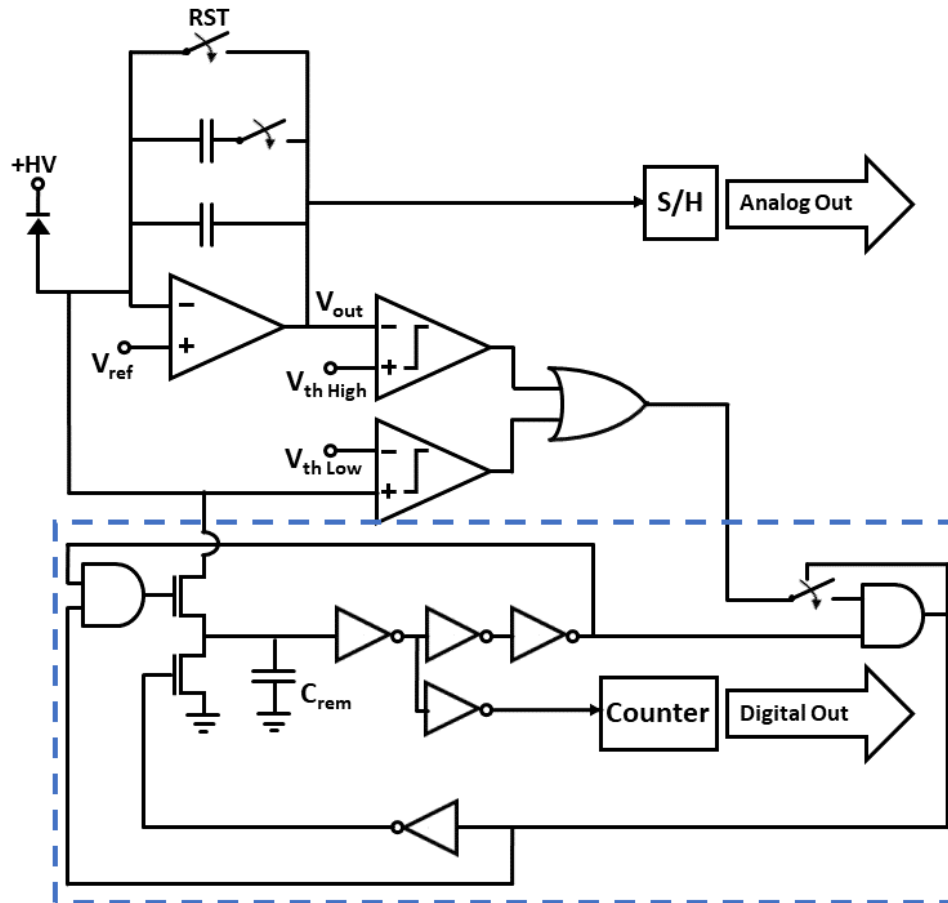


Figure 5.3: Simplified CDO schematic. The ring oscillator charge removal circuitry is enclosed in the dashed box. Selectable gain was replaced with an adaptive gain scheme in a subsequent fabrication.

removal is also triggered by any significant deviations of this voltage from V_{ref} . Deviations from V_{ref} indicate that the integrator is unable to keep up with incident photocurrent, in which case charge removal is needed. If the integration node is unable to be maintained at V_{ref} some error in integration is inevitable.

At low x-ray flux, the circuit operates similarly to the MM-PAD, but the tracking of charge removal rate with incident photocurrent should allow the CDO to continuously integrate larger sustained inputs. As depicted in figure 5.3 the CDO variation tested here utilizes a selectable gain, which was replaced with adaptive gain circuitry in the 16x16 pixel array test ASIC described in

Chapter 6. Additionally, the integrating amplifier studied here is a simple, five transistor differential amplifier. The amplifier is intentionally incapable of high current integration. Its use was intended to ensure that the pixel in this test ASIC would rely more heavily on the charge dump oscillator circuitry. The amplifier has been replaced by a class AB amplifier similar to that of the MM-PAD 2.0 in subsequent pixel iterations. Both comparators in the pixel are asynchronous, composed of a five transistor differential amplifier driving two inverters.

The pixel components fabricated in this test ASIC include the integrating amplifier with selectable gain and the full charge dump oscillator circuitry with comparators monitoring both the front-end voltage and integrating amplifier analog output voltage. Both comparator output signals, the in-pixel OR combination of them, the oscillator output, and the integrating amplifier output voltage were buffered off chip for external measurement.

Charge dump oscillator charge removal

The CDO charge removal circuitry is depicted in the dashed box in figure 5.3. The timing of charge removal is controlled by the charging of C_{rem} , but rather than a current source controlling the rate of charging as in the MM-PAD 2.0, the rate of charging is controlled by the rate at which charge is pulled from the integration node. The charge removal timing capacitor is also the charge removal capacitor. In this way, the charge removal rate can increase when the front-end integration node is flooded with signal charge. The amount of time that C_{osc} is connected to the front-end also depends on the switching threshold of the first inverter in the chain. While the inverter thresholding of the CDO is very fast, it is more susceptible to fabrication process variation than the other

designs presented here. In this case, variation could result in different quantities of charge removed per cycle in each pixel. Although this can be calibrated, it is an additional complication. The charge removed per charge removal execution is

$$\Delta Q = C_{osc} V_{ref}. \quad (5.2)$$

as C_{rem} discharges to ground.

5.1.3 Capacitor flipping pixel

The third pixel front-end fabricated and tested relies on a charge removal method based on the flipped capacitor filter described in [71]. The capacitor flipping pixel integrator uses two equally sized integration capacitors connected in parallel, depicted in figure 5.4. One of the two integration capacitors is connected via a network of CMOS switches so as to allow the capacitor's polarity in the circuit to be reversed. Adaptive gain was not incorporated in the initial fabrication and is not shown in figure 5.4, but it was implemented in the 16x16 pixel array test ASIC described in Chapter 6.

Referring to figure 5.4, the pixel begins integration with the switches labeled "A" closed and the switches labeled "B" open. Charge is integrated onto both equal-sized capacitors in parallel. When the integrator output crosses the comparator threshold, the comparator fires. This activates the control logic which opens switches "A". After a brief delay to prevent shorting the integration capacitors, switches "B" are closed. This reverses the orientation of half of the integration capacitance. As a result, integrated positive charge on each capacitor neutralizes negative charge on the other capacitor. Thus, the integrator is

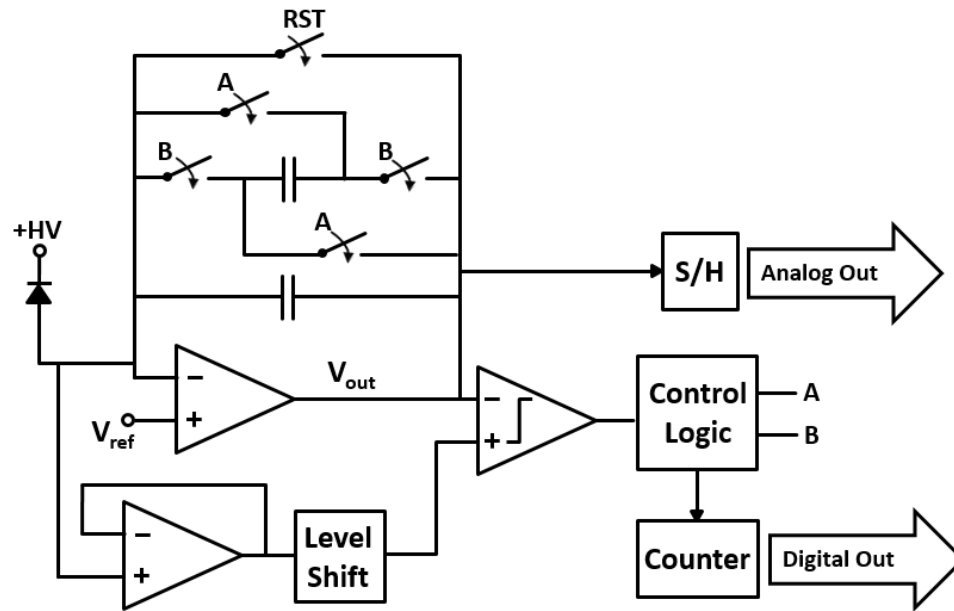


Figure 5.4: Simplified capacitor flipping pixel schematic. Dynamic thresholding circuitry is enclosed in the dotted box. An adaptive gain scheme was implemented in the most recent fabrication.

effectively reset, and can continue integrating photocurrent. Subsequent flipping occurs as needed. Connections to the flipping capacitor are always broken before new connections are made.

As with each other charge removal circuit, ΔQ depends on the front-end voltage of the integrator. To reduce the error introduced by changes in the front-end voltage due to large current spikes, a dynamic thresholding circuit was devised. Control was added such that dynamic thresholding can be toggled externally: the pixel comparator can use an external reference voltage to define the threshold at which capacitor flipping is initiated, or it can be set dynamically. In the dynamic case, a level-shifted copy of the front-end voltage is used to set the capacitor flipping threshold voltage. This ensures that there is a specific voltage across the integration capacitance at the time of the comparator firing, precisely the level shift voltage. However, due to the dependance of ΔQ in this method

on both the integrator input and output nodes, an input rate dependent error is introduced by delays in the capacitor flipping control logic. These errors are investigated in section 5.3.2.

The dynamic thresholding block level schematic is depicted in figure 5.4. The level shift is set by a diode drop within the pixel, though this was changed in subsequent iteration of the pixel. The integrating amplifier of the capacitor flipping pixel is a class AB amplifier similar to that of the MM-PAD 2.0, but optimized independently. The comparator is again asynchronous: a five transistor differential amplifier driving two inverters. The gated oscillator which controls the capacitor flipping is a ring oscillator.

This pixel components fabricated in this test ASIC include the integrating amplifier, capacitor flipping switches and control logic, make-before-break circuitry, and an externally toggled dynamic thresholding circuit. Capacitor flipping signals A and B, comparator output, front-end voltage, integrating amplifier analog output voltage, and the level-shifted threshold voltage were buffered off chip for measurement.

Capacitor flipping pixel charge removal

Make before break circuitry ensures that the integration capacitor to be flipped is disconnected before it is reconnected in reversed orientation. This prevents shorting the integration capacitors, which would neutralize signal charge in an uncontrolled way. Maximum rate of charge removal and charge removal pulse width is set by an inverter chain delay. The duration of this delay was set based on simulation to ensure complete charge neutralization between capacitor flips.

The charge removed per charge removal execution depends on the integrator output voltage:

$$\Delta Q = 2C_{int}(V_{ref} - V_{out}). \quad (5.3)$$

The factor of two accounts for charge on both capacitors being neutralized as C_{int} is half of the total integration capacitance. V_{out} is the output voltage sampled at the time of C_{int} disconnect. Dynamic thresholding aims to keep $V_{ref} - V_{out}$ at a fixed value in each charge removal execution.

5.2 Integrating amplifier

Each of the three pixel architectures tested here utilize similar integrating amplifiers. The integrating amplifier of the CDO in this test ASIC is not the topology discussed below, but subsequent iterations of the pixel do use this architecture.

The design goals of the pixels discussed here are demanding. In general, to measure a large photocurrent with a charge sensitive amplifier, an equal current must be supplied by the amplifier. A flux of 10^{11} 8 keV x-rays absorbed in a silicon photodiode corresponds to more than $35\mu\text{A}$ photocurrent. The integrating amplifier of these pixels must be capable of outputs on this level. However, these pixels should be designed with scaling in mind. Ideally, the pixels would be fabricated in an array of 128×128 pixels, more than sixteen thousand total pixels, so the in-pixel circuitry must have a low average power consumption.

Additionally, an amplifier used with a charge removal system must be capable of high slew rates in both positive and negative directions. The amplifier must have an output that keeps up with incident photocurrent, but also brings the front-end voltage back to its quiescent point quickly after each charge re-

moval execution. For these reasons a class AB topology based on the work of Carvajal et al. was chosen [70].

Class AB amplifiers combine the benefits of both class A and class B amplifiers while attempting to minimize their shortcomings. Class A amplifiers maintain a constantly biased output stage and thus exhibit minimal output distortions for signals in their full range. However, poor power efficiency and current utilization are inevitable in conditions where the full bias current is not required by the load being driven. A class A amplifier in the pixels discussed above would consume far too much power because the maximum drive required is very large. On the other hand, class B amplifier outputs are nearly off in quiescent conditions. The cost of this low power consumption is signal distortion in some input regimes.

Here a two stage AB topology is used in an effort to optimize both gain and output swing, as the full well of an integrator is linearly proportional to its output swing. The disadvantages of a multi-stage amplifier include added complexity, increased power consumption, and reduced bandwidth. These tradeoff can be mitigated and in this case are ultimately worthwhile.

Slight variations of the topology depicted in figure 5.5 were implemented in each of the pixels discussed in this dissertation. The amplifiers were individually tuned in each pixel, but the general operating principals are the same. To understand the architecture, we can break the schematic into several parts. Transistors M_1 and M_2 are the input transistors. The output stage is composed on transistors M_4 and M_8 . Transistors symmetric about a vertical line down the middle of the schematic are matched in size.

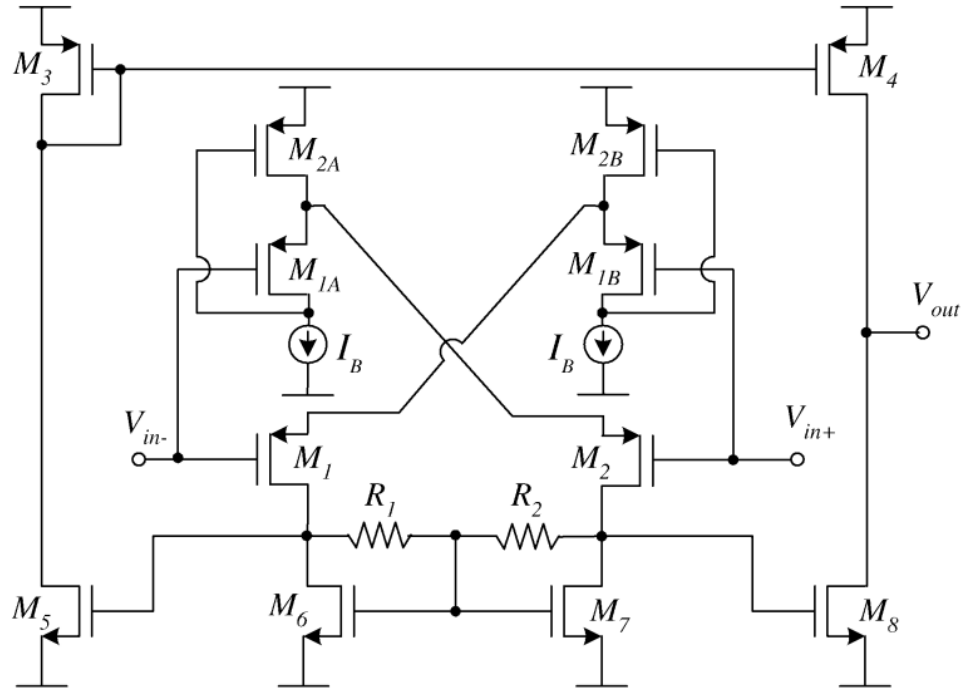


Figure 5.5: Class AB amplifier topology utilized in pixel prototypes. Architecture adapted from [70].

5.2.1 Flipped voltage follower

Transistors M_{1A} , M_{2A} , and the current source I_B form a flipped voltage follower, as do their counterparts M_{1B} , M_{2B} , and the second I_B . The architecture is discussed in detail in [72] and is named by Carvajal et al. the flipped voltage follower (FVF). Consider the transistors M_{1B} , M_{2B} , and their current source I_B . Together these transistors form a DC level shifter with very low output impedance, which permits high current draw.

The current source I_B is a single transistor with an external bias which sets the minimum current draw of the FVF. The current through M_{1B} is I_B . Assuming that the transistors are operating in saturation and channel length modulation

is negligible,

$$I_B = I_{1B} = \frac{1}{2}\mu_p C_{ox} \frac{W_{1B}}{L_{1B}} (V_{s1} - V_{in+} - V_{thp})^2, \quad (5.4)$$

where μ_p is the hole mobility, C_{ox} is the gate-oxide capacitance per unit area, $\frac{W_m}{L_m}$ is the width to length ratio of transistor m , V_{sm} is the source voltage of transistor m , and V_{thp} is the PMOS threshold voltage. For the sake of concision in this chapter, the term $\mu_{n,p} C_{ox} \frac{W_m}{L_m}$ will be defined

$$\beta_m \equiv \mu_{n,p} C_{ox} \frac{W_m}{L_m} \quad (5.5)$$

for transistor m , where the applicable mobility can be inferred from the schematics referenced.

Given equation 5.4, we know that

$$V_{s1} = \sqrt{\frac{2I_B}{\beta_{1B}}} + V_{in+} + V_{thp}, \quad (5.6)$$

which is a level shifted copy of V_{in+} . Similarly,

$$V_{s2} = \sqrt{\frac{2I_B}{\beta_{1A}}} + V_{in-} + V_{thp}. \quad (5.7)$$

The input of one half of the amplifier linearly shifts the source voltage of the input transistor in the other half. This adaptive biasing applies differential inputs to both the gate and source of the input transistors, doubling the transconductance of the differential pair. As a result, the amplifier can be biased such that the quiescent current is low, but a differential signal will still initiate a strong response.

The current through the input transistor M_1 is then

$$I_1 = \frac{\beta_1}{2} \left(\sqrt{\frac{2I_B}{\beta_{1B}}} + V_{\Delta} \right)^2 \quad (5.8)$$

where $V_{\Delta} \equiv V_{in+} - V_{in-}$. The current through the input transistors flows to the current sinks M_6 and M_7 and sets the output voltages which serves as the input voltages for the second stage of the amplifier. Before examining the output stage however, we must address resistors R_1 and R_2 which set the bias on the current current sinks and provide common mode feedback.

5.2.2 Local common mode feedback

The bias of M_6 and M_7 could be set externally, making them simple current mirrors. In this case, the maximum downward slew rate of the first stage would be limited by this bias current. Matched resistors R_1 and R_2 are added to provide local common mode feedback (LCMFB) as demonstrated in [70] and discussed in [73]. For $V_{in+} = V_{in-}$ the current across these resistors is zero. If the voltage of the first stage output nodes, V_{d1} and V_{d2} , rise in unison, the gate voltage of the current sources rises as well, and they sink more current to combat the change. Similarly, decreases in the gate voltage are resisted. Transistors M_6 and M_7 behave like diode connected transistors for common mode signals. As such, they have low output impedance

$$R_{out} \approx 1/g_{m6} \quad (5.9)$$

where g_{m6} is the transconductance of transistor M_6 . The gain of the first stage in common mode conditions is therefore low. With $V_{\Delta} = 0$, $I_{1,2} = I_{6,7} = I_B$ and the gate voltage of $M_{6,7}$ is equal to the drain voltage of $M_{1,2}$,

$$V_{d1,2} = V_{thm} + \sqrt{\frac{2I_B}{\beta_{6,7}}}, \quad (5.10)$$

assuming saturation of $M_{6,7}$ and matching of transistors $M_{1,2}$ with $M_{1B,1A}$.

However, when a differential signal is applied R_1 and R_2 maintain the gate voltages of M_6 and M_7 at a common voltage, so the transistors behave more like current sources. The first stage exhibits a higher output impedance:

$$R_{out} \approx R_1 \parallel r_{o1} \parallel r_{o6}, \quad (5.11)$$

where r_{om} is the drain-source impedance of transistor m and $R_n \parallel R_m$ indicates the resistance of R_n and R_m in parallel.

More quantitatively (following the work in [70]), for a differential signal $V_\Delta = V_{in+} - V_{in-}$ a current flows through the feedback resistors $R_{1,2}$. If channel length modulation is negligible, M_6 and M_7 sink equal currents because they have equal V_{gs} , so the current through the resistors is half the difference between branches, $I_R = (I_1 - I_2)/2$. The current through M_6 and M_7 is the common mode current, $I_{cm} = (I_1 + I_2)/2$. The common gate voltage of M_6 and M_7 is

$$V_{g6,7} = V_{thn} + \sqrt{\frac{2I_{cm}}{\beta_{6,7}}} \quad (5.12)$$

and the drain voltages of M_1 and M_2 respectively are

$$V_{d1} = V_{g6} + R_1 I_R \quad (5.13)$$

and

$$V_{d2} = V_{g7} - R_2 I_R \quad (5.14)$$

assuming $V_{in+} > V_{in-}$ and therefore $I_1 > I_2$. For $V_{in+} < V_{in-}$ the signs of the second term in equations 5.13 and 5.14 are reversed.

Relative to externally biased current sources, the maximum downward slew rate can be increased by the LCMFB, yet the first stage of the amplifier can be designed with a low quiescent current $\approx 2I_B$. The adaptive action of the FVFs

and LCMFB aid in accomplishing the goal of low quiescent power consumption with high gain. High slew rate in the first stage is important for a rapid amplifier response. R_1 and R_2 can be implemented with externally biased MOS transistors.

5.2.3 Amplifier output

Assuming that the output transistors operate in saturation and channel length modulation is negligible, using equations 5.13 and 5.12, the current through transistor M_5 is

$$I_5 = \frac{\beta_5}{2}(V_{d1} - V_{thn})^2 = \frac{\beta_5}{2} \left(\sqrt{\frac{2I_{cm}}{\beta_6}} + R_1 I_R \right)^2. \quad (5.15)$$

This current is mirrored to M_4 . If we assume that the differential signal is large and positive, $I_R \approx I_1/2$ and $I_{CM} \approx I_1/2$. Under these conditions M_8 is effectively off and the output current is

$$I_{out} \approx I_5 = \frac{\beta_5}{2} \left(\sqrt{\frac{I_1}{\beta_6}} + \frac{R_1 I_1}{2} \right)^2. \quad (5.16)$$

Referring to equation 5.8 for the value of I_1 we see that

$$I_{out} \approx \frac{\beta_5}{2} \left[\frac{R_1 \beta_1}{4} V_\Delta^2 + \left(\sqrt{\frac{\beta_1}{2\beta_6}} + \frac{R_1 \beta_1}{2} \sqrt{\frac{I_B \beta_1}{\beta_{1B}}} \right) V_\Delta + \left(\sqrt{\frac{I_B \beta_1}{\beta_{1B} \beta_6}} + \frac{R_1 \beta_1 I_B}{2\beta_{1B}} \right) \right]^2. \quad (5.17)$$

If I_B is small, this reduces to

$$I_{out} \approx \frac{\beta_5}{2} \left(\frac{R_1 \beta_1}{4} V_\Delta^2 + \sqrt{\frac{\beta_1}{2\beta_6}} V_\Delta \right)^2. \quad (5.18)$$

I_B in the pixels discussed here is between 5-15 μ A. To leading order the output current is proportional to V_Δ^4 . Conversely if V_Δ is large and negative, the output

current is the current through M_8 ,

$$I_{out} \approx \frac{\beta_8}{2} \left[\frac{R_2 \beta_2}{4} V_{\Delta}^2 - \left(\sqrt{\frac{\beta_2}{2\beta_6}} + \frac{R_2 \beta_2}{2} \sqrt{\frac{I_B \beta_1}{\beta_{1A}}} \right) V_{\Delta} + \left(\sqrt{\frac{I_B \beta_2}{\beta_{1A} \beta_6}} + \frac{R_1 \beta_2 I_B}{2\beta_{1A}} \right) \right]^2. \quad (5.19)$$

Again, if I_B is small, we have

$$I_{out} \approx \frac{\beta_8}{2} \left(\frac{R_2 \beta_2}{4} V_{\Delta}^2 - \sqrt{\frac{\beta_2}{2\beta_6}} V_{\Delta} \right)^2, \quad (5.20)$$

where now we make the assumptions that $I_R \approx I_2/2$ and $I_{CM} \approx I_2/2$. Note that V_{Δ} is negative in equation 5.20 and the current here is flowing into the amplifier through M_8 .

When V_{Δ} is small, the current through the resistors is

$$I_R = \frac{I_1 - I_2}{2} = V_{\Delta} \beta_1 \sqrt{\frac{2I_B}{\beta_{1B}}} \quad (5.21)$$

from equation 5.8 and its M_2 counterpart, noting that M_1 and M_2 are matched transistors, as are M_{1A} and M_{1B} , so their β values are equal if we ignore process variation. The common mode current is then

$$I_{CM} = \frac{I_1 + I_2}{2} = \frac{\beta_1 I_B}{\beta_{1A}} + \frac{\beta_1 V_{\Delta}^2}{2}, \quad (5.22)$$

and the output current is

$$I_{out} = I_4 - I_8 = \beta_5 R_1 I_R \sqrt{\frac{8I_{CM}}{\beta_6}}. \quad (5.23)$$

The small signal differential voltage gain of the first stage is

$$\frac{V_{d1} - V_{d2}}{V_{in+} - V_{in-}} = 2g_{m1}(r_{o1} \parallel r_{o6} \parallel R_{1,2}), \quad (5.24)$$

noting that transistors on either side of the schematic in figure 5.5 are matched and $R_1 = R_2$. The small signal gain of both stages combined is

$$\frac{V_{out+} - V_{out-}}{V_{in+} - V_{in-}} = 2g_{m1}g_{m8}(r_{o4} \parallel r_{o8})(r_{o1} \parallel r_{o6} \parallel R_{1,2}). \quad (5.25)$$

Based on simulations, the gain of the implemented amplifier is 44.0dB. The phase margin is 72.2°. The bandwidth, described by the amplifier 3dB point, is 5.67MHz. Quiescent power consumption is 108μW with a 1.8V power supply. Peak output current is on the order of 500μA. Output swing is nearly rail-to-rail, but in practice the output is kept between 0.3V and 1.1V by feedback and charge removal.

5.2.4 Noise properties

5.2.5 Pole splitting

Negative feedback is intended to ensure stability. In differential amplifiers, negative feedback implies that a scaled copy of the output signal is subtracted from the input and the output is proportional to this difference. Consider the simple model in figure 5.6 to see that an equilibrium is possible.

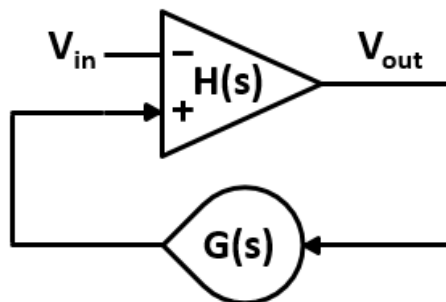


Figure 5.6: Example of negative feedback.

The amplifier has the transfer function $H(s)$. The tear drop represents an arbitrary feedback element with transfer function $G(s)$ from the amplifier output to input. The output of the amplifier is the input to the positive terminal minus

the input to the negative terminal multiplied by the transfer function:

$$V_{out} = H(s)[V_{in} - G(s)V_{out}] \quad (5.26)$$

Therefore the gain of the amplifier with feedback is

$$\frac{V_{out}}{V_{in}} = \frac{H(s)}{1 + G(s)H(s)}. \quad (5.27)$$

For large $H(s)$, equation 5.27 is approximately equal to $\frac{1}{G(s)}$. The transfer function of a high gain amplifier with negative feedback can be set by selection of the feedback elements. This is because negative feedback functions similarly to a restoring force in a stable physical system. If the output of the amplifier is greater than the level dictated by the feedback elements, the subtraction of the output at the amplifier's input will bring the output back down. Similarly, if the output is too small, a larger signal results from the subtraction operation. An equilibrium is eventually reached as long as the feedback is subtracted from the input. What would happen if the feedback was instead added? We would find that

$$\frac{V_{out}}{V_{in}} = \frac{H(s)}{1 - G(s)H(s)}. \quad (5.28)$$

In this case, if $G(s)H(s) = 1$ the gain of the system is infinity. Note that both G and H are functions of s , a frequency dependent term. This is because in practice, the transfer function of circuit elements is frequency dependent. Circuit elements not only alter the voltage level of signals, but also induce a phase shift. If this phase shift reaches 180° , the negative feedback becomes positive feedback, and the system is no longer stable.

Op-amps generally induce a phase lag with an absolute value that increases from zero with increasing frequency. To ensure stability, the gain of a system must be less than one for frequencies at which the phase shift is greater than

180°. If it is not, the system will amplify the signal and oscillate at this frequency indefinitely. An amplifier's phase margin is defined as 180° minus the absolute value of the phase shift imparted to signals at the unity gain frequency in open-loop. The unity gain frequency is the frequency at which the amplifier's open-loop gain has dropped to one. The phase margin is a metric used to gauge whether an amplifier will be stable in practice. Generally the value should be kept greater than 45°.

To ensure stability in some iterations of the amplifier in figure 5.5, pole splitting was employed. For a more detailed discussion of poles see [30]. The dominant pole in the first stage of the class AB amplifier discussed here is the output pole with frequency $f = 1/[2\pi(R_1||r_{o1}||r_{o6})C_{gs5}]$. Note that the gates of transistors M_6 and M_7 are at virtual ground, so they do not contribute to this pole. The dominant pole of the amplifier's second stage is formed by the load capacitance and the output impedance, $R_{out} = r_{o4}||r_{o8}$. By connecting a capacitor between the amplifier output and the gate of M_8 , we accomplish Miller compensation [30]. The Miller effect enhances the impact of this capacitance, and the dominant poles are shifted. The input pole is brought closer to the origin, while the output pole is pushed to higher frequencies. The poles are "split."

The effect of pole splitting is to bring the unity gain frequency to a lower frequency while pushing the frequency at which feedback signals are phase shifted by 180° to higher frequencies. This reduces the overall amplifier bandwidth but increases the phase margin to ensure stability.

5.3 Current injection tests

The three pixel front-ends were fabricated with several means of injecting a test charge to emulate an input x-ray signal. A PMOS current source in each pixel provided simple functionality tests. For higher currents and quantitative results, a copy of each pixel with a probe pad attached to its input was included in fabrication. Current was injected into pixels through a tungsten needle with a 10k Ω resistor between the needle and an external current source. The current was generated and regulated by a Keithley 2400 Sourcemeter. Output signals were buffered off chip to a DPO7254C Tektronix oscilloscope.

Parasitic capacitance of the needle probe was estimated to be ~ 10 pF. This estimate is based on the change of V_{out} in the MM-PAD 2.0 pixel during a charge removal event. The integrating amplifier output voltage jumps during charge removal to maintain V_{ref} on the front-end. The jump is smaller with the needle contacting the front-end because the needle's parasitic capacitance reduces the charge transfer efficiency of the integrating amplifier, i.e. charge removal pulls some charge from the parasitic capacitance rather than the integration capacitance. This parasitic capacitance is significantly larger than the contribution expected from a bump bonded sensor, which is closer to 200fF. Based on calculations of charge transfer efficiency and simulation results, this increased parasitic capacitance reduces the maximum signals which can be properly integrated as a result of reducing ΔQ . The capacitance also has a damping effect on pixel front-end transient signals. Consequently this method is not suitable for testing pixel performance under pulsed input, but these results do indicate the magnitude of average input signal rates which can be integrated by the pixels under investigation.

5.3.1 Probe pad current injection

To evaluate the linearity of integration for each pixel architecture, pixel output was monitored with a constant current input. The measured output, charge removal frequency, was multiplied by nominal ΔQ values (the quantity of charge removed per removal execution) to calculate an inferred input current. This inferred input current can then be compared to the actual, known input current. These values are plotted against each other in figure 5.7. To measure the charge removal frequency, buffered charge removal control signals were measured on an oscilloscope, and edge finding algorithms were used to determine the time of each charge removal cycle. Linear fits to the time of each charge removal versus the number of charge removals preceding it yielded the charge removal period as the slope of the fit. From this, frequency and uncertainty in the determination of the frequency were extracted. Variations in frequency between traces at a given input current were larger than the uncertainty in the determination of the frequency in a single trace, but both measures of uncertainty are smaller than the data points plotted in figure 5.7. Voltages used in the calculation of charge removal quantities were taken at their nominal values, e.g., $V_{front-end}$ was taken as V_{ref} , which is set externally. Throughout this section, current is specified in units of equivalent 8 keV x-rays/s. This is the flux of 8 keV x-rays that, when absorbed in a reverse biased silicon photo diode, would produce an equivalent photocurrent.

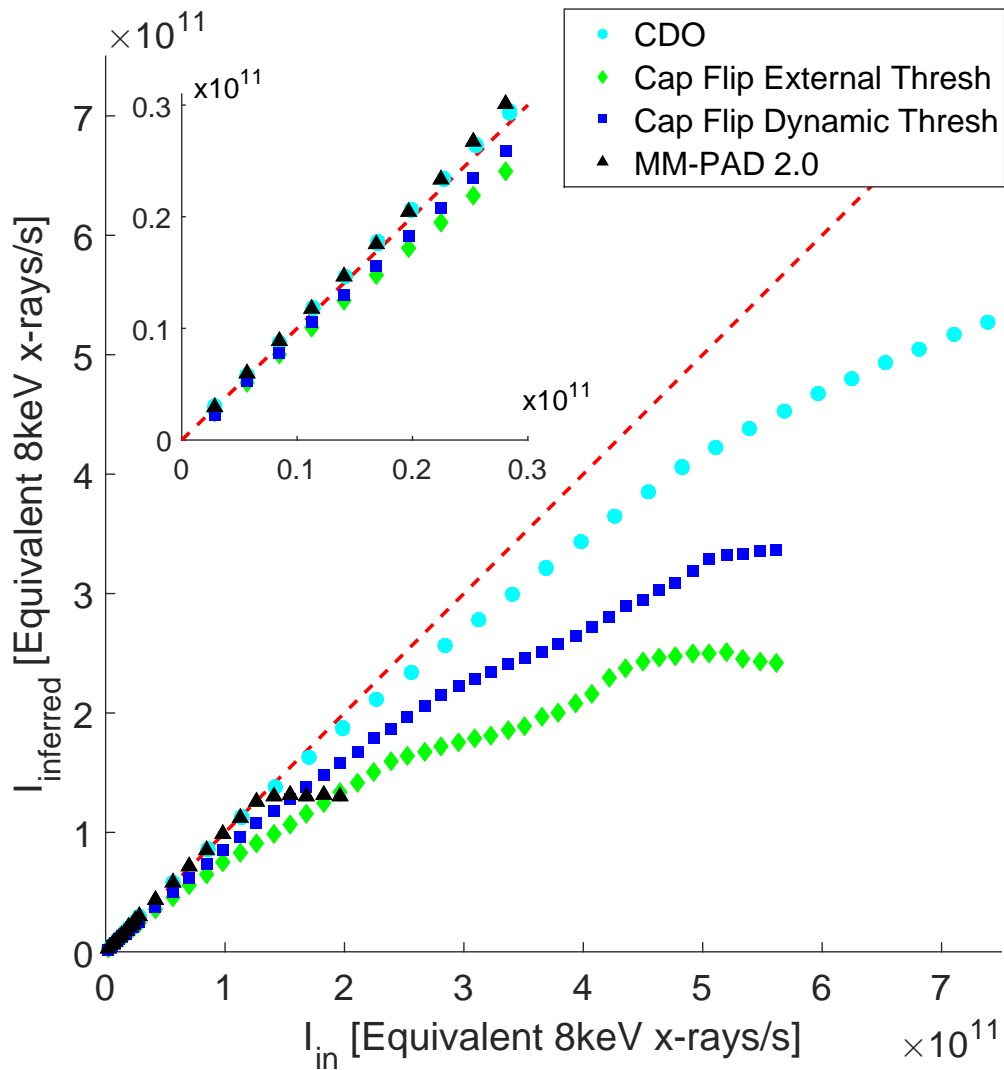


Figure 5.7: Inferred input currents based on pixel outputs versus actual input current. The dotted line represents an ideal response (inferred input equals actual input). The charge dump oscillator is plotted with circles, the MM-PAD 2.0 with triangles, the externally thresholded capacitor flipping pixel with diamonds, and the dynamically thresholded capacitor flipping pixel with squares. Input and inferred current values are converted to the number of 8 keV x-rays absorbed in silicon per second which would produce an equivalent photocurrent. Inset: Magnification of the same data.

5.3.2 Performance and analysis

The MM-PAD 2.0 results are shown as triangles in figure 5.7. Good performance is seen with inputs up to 1.3×10^{11} 8 keV x-rays/s equivalent. The inferred current measurement abruptly plateaus, indicating that the pixel oscillator is operating at its maximum frequency. These values are consistent with simulation. Deviation from linearity is likely a result of process variation in charge removal capacitor size and $V_{front-end}$ not being held precisely at V_{ref} . This can be calibrated.

The CDO results are shown as circles in figure 5.7. At low input currents, the inferred input is greater than the actual input, which implies that ΔQ is less than what is expected based on the value of V_{ref} . This could be a result of process variation in capacitor size. Alternatively, incomplete charge removal may occur because signals in the ring oscillator propagate quickly compared to time constants associated with the charge dump process. If the dump is repeatable, the digital gain of each pixel can be calibrated. However, because the switching of the CDO is regulated by the threshold of an inverter, the stability of any calibration is threatened over time by radiation damage which can result in device threshold shifts.

As the input current increases, the CDO's inferred input current drops below the actual input current. In this regime, above 10^{11} x-rays/s, the quantity of charge removed per charge removal execution exceeds the expected value. A likely cause of this error is a significant rise in the pixel front-end voltage above V_{ref} . This would cause more integrated charge to be removed from the integration node than intended.

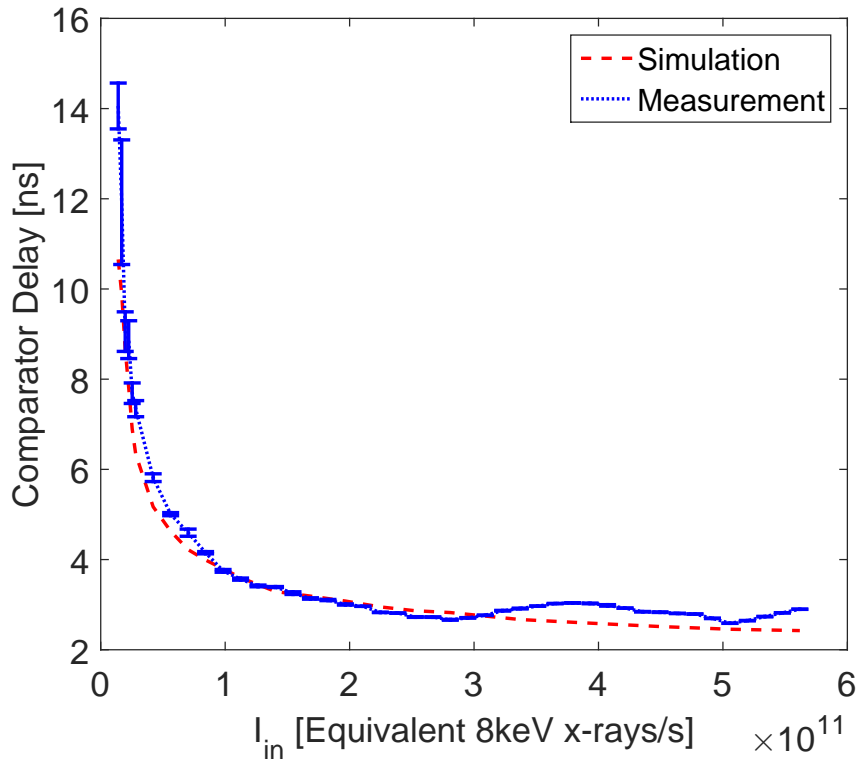


Figure 5.8: Measured comparator delays from the capacitor flipping pixel with dynamic thresholding are plotted. Measured values assume that all deviations from linearity in the capacitor flipping pixel’s output are a result of charge integrated during switching delays. Values from simulation are plotted as a dotted line.

Capacitor flipping pixel data was taken with both dynamic thresholding and a fixed, external threshold. These data are plotted in figure 5.7 as squares and diamonds, respectively. Some error in externally thresholded operation is a result of the integrator front-end voltage drifting upwards with higher input currents. This drift was observed directly in testing. The decrease of inferred current above 5×10^{11} 8 keV x-rays/s equivalent input in the externally thresholded case is likely a result of the front-end voltage being pushed outside of the integrating amplifier’s range of optimal operating conditions.

A clear improvement in performance is seen with the dynamic thresholding enabled. However, there is still substantial error in the input reconstruction:

less than 70% of the input is accounted for above 3.5×10^{11} x-rays/s equivalent input. This error can be explained by noting that the quantity of charge neutralized per capacitor flip, ΔQ , depends on the voltage across the integrator, not just the front-end voltage as in the other pixel designs. This means that any delay between when the capacitor should be disconnected and when it actually does disconnect can introduce error. Specifically, if photocurrent continues to be integrated during this delay, the output voltage of the integrator will continue to drop and the charge neutralized will be greater than anticipated.

From these data we can extract the error per capacitor flip. This is the difference between actual and inferred input currents divided by the frequency of capacitor flipping. Put another way, this is the charge removed per capacitor flip beyond what is expected based on the value of the level shift. Simulations of the comparator employed in this particular pixel front-end show that its firing delay varies with input falling edge slope, or equivalently in this case, input current. If we assume that all of this deviation from linearity is a result of photocurrent accumulation during the switching delay, dividing the error per capacitor flip by input current yields a measurement of this delay. Figure 5.8 plots the measured delays (assuming that all error comes from the delay) on top of the switching delays from simulation, both as functions of input current.

The measurement appears to follow the simulated values. This highlights a problem inherent to the capacitor flipping charge removal design. Any delay between when the capacitor should flip and when it actually does creates a window in which integrated charge will not be accounted for. Some of the calculated error may be due to an offset in the comparator threshold, but potential for input rate dependent error is ultimately inherent to the design.

Table 5.1: Pixel Average Power Consumption From Simulation

		MM-PAD 2.0	CDO	Cap Flip
Active Power (Integrating 10^{11} 8 keV x-rays/s)	Analog	146 μ W	52.7 μ W	158 μ W
	Digital	79.8 μ W	130 μ W	27.2 μ W
	Total	226μW	183μW	185μW
Quiescent Power	Analog	102 μ W	52.7 μ W	194 μ W
	Digital	3.63nW	775nW	0.563nW
	Total	102μW	53.5μW	194μW

Power consumption

While maximizing the input range of pixels, it is essential to keep power consumption manageable. Power consumption was measured in simulation for each pixel substructure and is listed in Table 5.1. Performance of the pixels in simulation was commensurate with their measured performance. These power consumption figures have been deemed suitable for scaling to full arrays with a planned 150 μ m pixel pitch in a 128x128 pixel array. Based on experience with previous detectors such as the MM-PAD, the temperature of a single ASIC can be sufficiently regulated by a water cooled peltier module providing 3-5 W cooling power.

The capacitor flipping pixel exhibits decreased analog power consumption under high loads. This is because the integrating amplifier in this pixel is a class AB amplifier, and after triggering a charge removal event, it is not required to slew back up to achieve its quiescent voltage. Instead, integrated charge is transferred to the integrator output by the capacitor flipping, and voltage is restored with minimal current supplied by the amplifier. This is not the case in the other pixel architectures.

5.4 Summary

The performance of the pixel substructures discussed above demonstrates that each is capable of integrating large quantities of photocurrent. The MM-PAD 2.0 exhibits robust performance up to the design goal of 10^{11} 8 keV x-rays/pixel/s and has demonstrated the viability of adaptive gain in conjunction with charge removal.

The CDO appears to handle very high input currents better than the other pixel prototypes, but the CDO also presents a number of development risks. Since the CDO pixel relies on the threshold voltage of a digital inverter to regulate the removal of charge, pixel-to-pixel variation and calibration stability are potential weaknesses of the design. As a practical matter, small, static pixel-to-pixel variations in charge removal amounts can be accounted for with detector calibration. A greater concern is calibration stability because radiation exposure can induce threshold shifts. As a general scheme, the CDO does offer a possible avenue for the development of high-speed charge removal and in-pixel analog-to-digital conversion, but the trade-offs are not well known and the degree of pixel to pixel variations in the CDO have not yet been studied.

The capacitor flipping pixel exhibits a systematic deviation from linearity which is ultimately undesirable for scientific work, but the effectiveness of the dynamic thresholding concept is demonstrated. This dynamic adjustment for deviations of the pixel front-end voltage from V_{ref} could be utilized in other ways. For example, in the MM-PAD ΔQ is set by the difference between $V_{front-end}$ and V_{low} . V_{low} could be dynamically adjusted relative to $V_{front-end}$. In this way, a constant ΔQ can be enforced in the face of changing front-end voltages.

CHAPTER 6

THE HIGH DYNAMIC RANGE PIXEL ARRAY DETECTOR

6.1 Introduction

The pixel front-ends described in the previous chapter were developed into fully operational pixels with mixed analog and digital readout. The pixels were tiled to form a 16x16 pixel array and fabricated in TSMC 180nm mixed signal general-purpose II 1P6M salicide technology with 2 fF/ μm^2 MIM-caps and thick top metal through Europractice. Support electronics were developed and a software interface was implemented to control the PAD. A 500 μm silicon sensor was bonded to the array. The chip was set on a thermally regulated heat sink inside a vacuum enclosure with a thin window made of aluminized mylar. All together, the system is a fully functional x-ray hybrid PAD.

This chapter will describe the system and its functionality. Throughout the chapter, this system will be referred to as the high dynamic range pixel array detector (HDR-PAD).¹

6.2 System overview

Figure 6.1 is an image of the HDR-PAD detector fully assembled. The primary components of the detector unit are labeled. The field programmable gate array (FPGA) handles all communication between the controlling computer and

¹At the time of the writing of this dissertation, all ASIC and PCB schematics, mechanical drawings, and FPGA codes relevant to the HDR-PAD are located on the Gruner group server "People" in directory /us/Detectors-EssentialInformation/HDR-PAD/HDR-PAD_Sub2/.

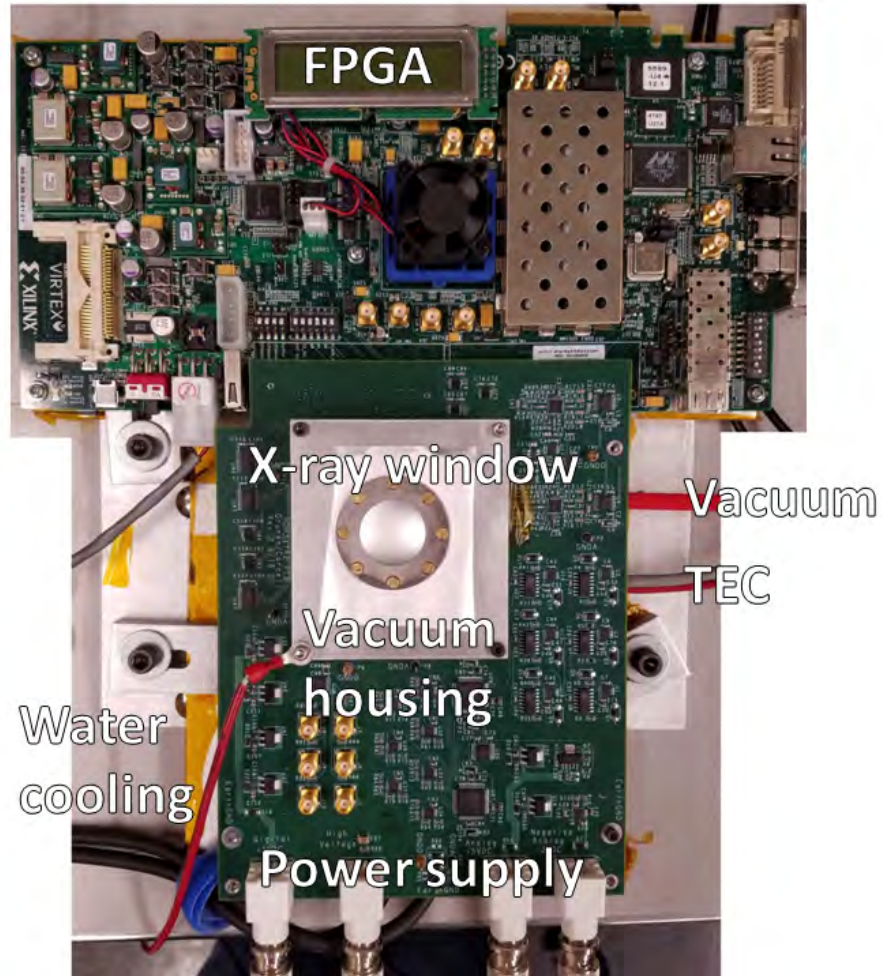


Figure 6.1: Photograph of the high dynamic range pixel array detector (HDR-PAD) unit with FPGA, vacuum enclosure, and PCB support electronics shown. Not shown are power supply units, controlling computer, vacuum, water chiller, and thermoelectric controller. The vacuum housing is roughly four inches along each edge.

the detector ASIC. The FPGA also programs digital to analog converters on the support electronics printed circuit board (PCB) and issues all clocking signals. The FPGA receives data output from the ASIC through the PCB and assembles the data into packets which are sent to the control computer via Ethernet.

The aluminum block in figure 6.1 is a vacuum clam shell enclosure which sandwiches a metalized ring on the PCB, making an o-ring vacuum seal. There

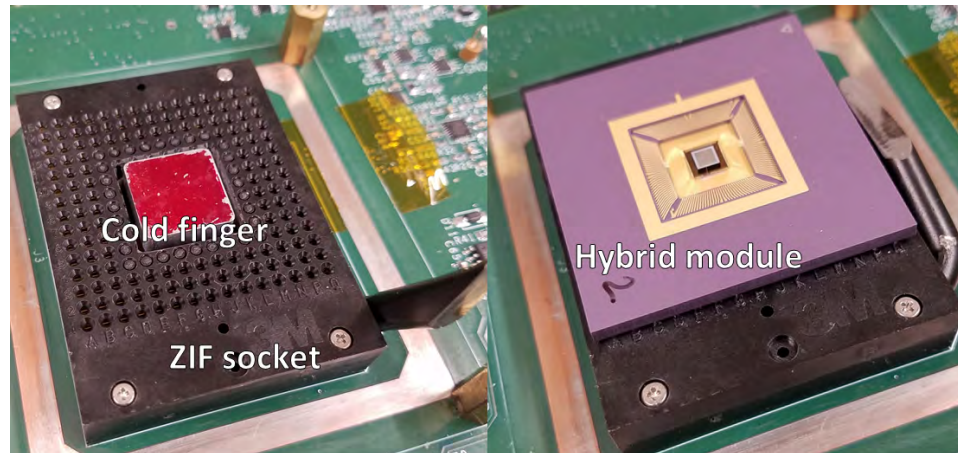


Figure 6.2: LEFT: ZIF socket on the support electronics PCB with thermally regulated cold finger protruding. The PCB metalization which is sandwiched by the clam shell assembly is visible. RIGHT: Hybridized module wire bonded to a ceramic pin grid array (PGA) package, seated in the ZIF socket. The cold finger makes contact with the backside of the packaging.

is a hole in the center of the PCB through which the thermally regulated heatsink, connected to the bottom half of the clam shell, protrudes. Figure 6.2 shows the cold finger protruding through the zero insertion force (ZIF) socket into which the HDR-PAD module is to be seated, along side an image of the module placed in the socket.

A thermistor is connected to the cold finger which rests on top of a Peltier thermoelectric (TEC) module. The thermistor feeds back to the TEC controller to regulate the temperature of the detector module. The clam shell is water cooled and was constructed by the Gruner group.

The PCB to which the ZIF socket is connected contains several important circuits. Digital to analog converters (DACs) set voltages which in turn determine bias voltages and bias currents which are generated and regulated on the PCB and fed to the ASIC. The ASIC power supplies are fed to the PCB through BNC connections visible in figure 6.1 but are regulated locally on the PCB. Level

shifters buffer digital signals from the FPGA to the ASIC, including clock signals. The PCB also contains analog to digital converters (ADCs) which are controlled by the FPGA. They receive analog data from the ASIC and send digital conversions of the data to the FPGA to be recorded.

HDR-PAD ASICs were bonded to 500 μm thick silicon photodiodes fabricated by SINTEF (Oslo, Norway). The diodes feature gold pad metalization over p+ implantation on the ASIC bonding side. The x-ray entrance side is coated with an aluminum metalization for bias voltage application over n+ implantation. These diodes were originally developed for use with the MM-PAD detector and more details can be found in Lucas Koerner's dissertation in which the same sensors were employed [74]. Because the ASIC studied here is the product of a multi-project wafer fabrication, only diced ASICs could be procured and thus wafer-level bump bonding was not possible. To bond the sensor to the ASIC, silver epoxy bumps were applied via stencil to pixel inputs and gold studs were applied to pixel connections on the sensor. Flip-chip bonding of the sensor and ASIC was then possible.²

Figure 6.3 is a photograph of a hybridized HDR-PAD module. The top most layer is the 500 μm silicon sensor which is bonded pixel-by-pixel to the ASIC. The ASIC is wire bonded to a ceramic pin grid array (PGA) package. All communications to and from the ASIC are transmitted by the wire bonds. A single wire bond can be seen connecting directly to the sensor layer. This wire bond supplies the high voltage necessary to reverse bias the sensor layer. The high voltage supply is connected through the PCB.

²The bonding procedure outlined here was performed by Jim Clayton of Polymer Assembly Technology, Inc. (Research Triangle Park, NC). At the time of the writing of this dissertation, all documentation related to this bump bonding are located on the Gruner group server "People" in directory /us/Detectors-EssentialInformation/HDR-PAD/HDR-PAD_Sub2/stud_bonding_info/.

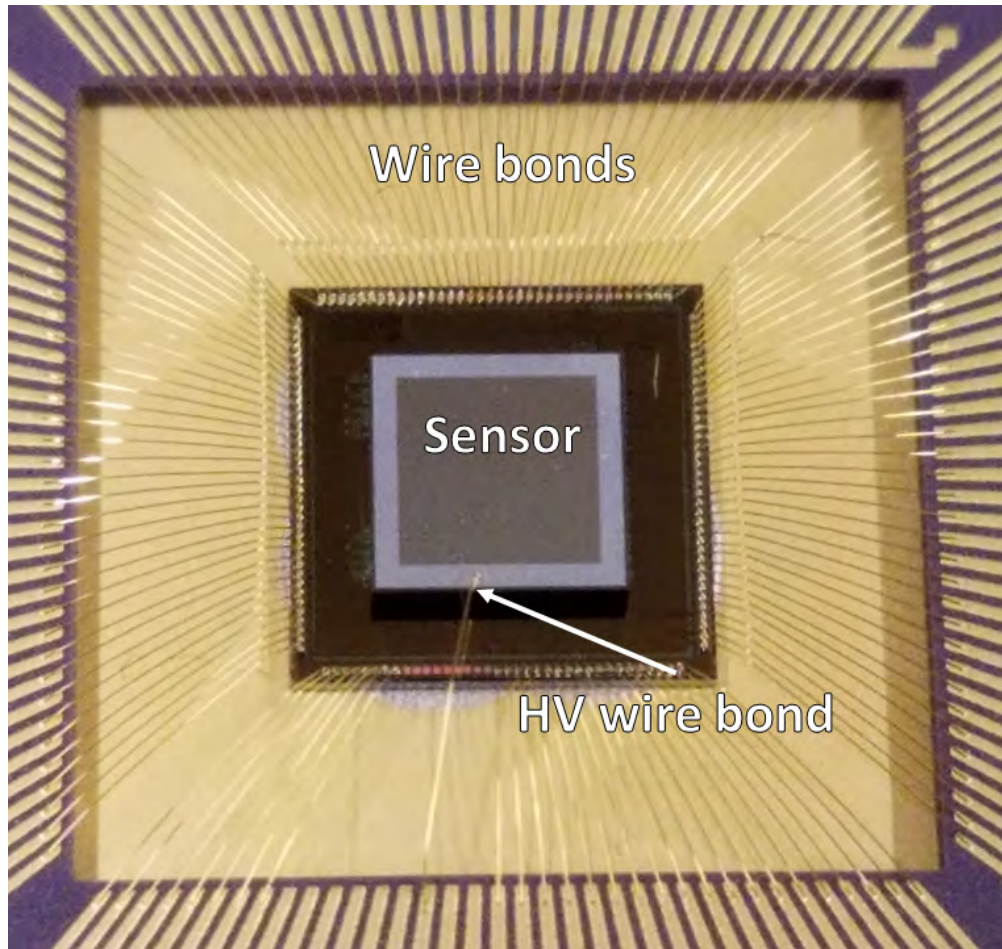


Figure 6.3: Close up image of a HDR-PAD hybrid module wire bonded to the PGA package. A single wire bond connects to the top surface of the sensor layer to supply the reverse biasing voltage. The wire bond is made to a thicker aluminization which is visible along the edge of the sensor.

6.3 HDR-PAD ASIC

The HDR-PAD ASIC contains five pixel front-end variants with identical adaptive gain control circuitry, analog readout chains, digital readout chains, and unified control signals. All pixels image simultaneously. Below the components which are common to all pixels will be discussed after a brief overview of how the pixels differ from the pixel front-ends described in Chapter 5.

6.3.1 Pixel overview

The five pixel variants fabricated on the HDR-PAD ASIC include two MM-PAD 2.0 variants, the charge dump oscillator, the capacitor flipping pixel, and a modification of the MM-PAD 2.0 pixel which will be referred to as the mixed mode low drop out pixel (MM-LDO). The two MM-PAD 2.0 variants differ from each other only in their total low gain integration capacitance. The front-ends of these pixels have not changed substantially from the test structures included in the first small scale fabrication described in Chapter 5. The CDO pixel has implemented adaptive gain and the integrating amplifier has been replaced with the same class AB amplifier as the capacitor flipping pixel uses. The capacitor flipping pixel has implemented adaptive gain as well, and the level shifter utilized in the dynamic thresholding scheme has been modified for lower power consumption.

The LDO pixel is a clone of the MM-PAD 2.0 pixel, but the voltage which determines the amount of charge removed with each charge removal execution is controlled dynamically relative to the front-end. This dynamically adjusted level is maintained by a low dropout regulator circuit which is capable of maintaining a reference voltage over a wide range of input currents. Figure 6.4 is a block level schematic of the LDO pixel. The level shifter used is the same as the updated level shifter in the capacitor flipping pixel. The circuitry added to the MM-PAD 2.0 framework maintains $V_{low} = V_{front-end} - V_{levelshift}$. A current source is required to bias the regulator and prevent V_{low} from dropping to ground. The transistor driven by the amplifier can be thought of as a variable resistor whose impedance is adjusted to keep the input terminals of the operational amplifier equal. The range of possible impedances is very large, and so the voltage on

this node can be maintained over a wide range of currents.

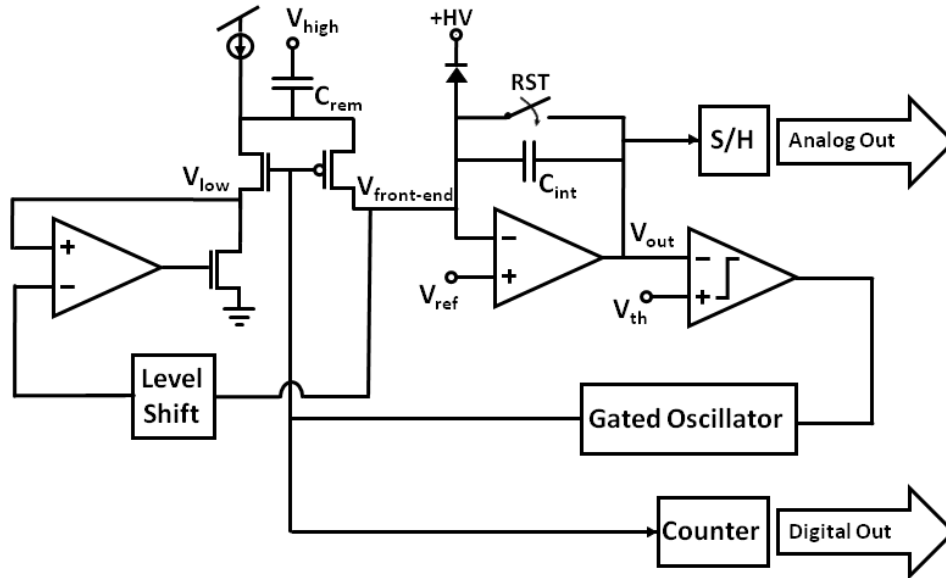


Figure 6.4: Simplified MM-LDO schematic. The pixel is identical to the MM-PAD 2.0, but rather than an externally supplied V_{low} , the voltage is maintained by a low dropout regulator circuit. The level of this voltage is set relative to the front end.

The LDO modification is intended to benefit charge removal during very high instantaneous flux. When the integrating amplifier is unable to maintain V_{ref} on the front-end, the quantity of charge removed from the integration node per capacitor switching execution, $\Delta Q = C_{rem}(V_{front-end} - V_{low})$, will vary from the expected value, $\Delta Q = C_{rem}(V_{ref} - V_{low})$. By setting V_{low} relative to the front-end, the quantity of charge removed should be more consistent: $\Delta Q = C_{rem}(V_{front-end} - V_{low}) = C_{rem}V_{levelshift}$.

Table 6.1 summarizes the front end specifications of all five pixel variants.

Table 6.1: Pixel front-end specifications

Pixel	$C_{highgain}$ [fF]	$C_{lowgain}$ [fF]	C_{rem} [fF]	$V_{ref} - V_{th}$ [V]
MM-PAD 2.0 v1	40	880	880	0.5
MM-PAD 2.0 v2	40	2630	880	0.5
Charge dump oscillator	77	962	342	0.5
Capacitor flip	40	1000	1000	0.5
MM-LDO	40	880	880	0.5

6.3.2 Data readout

For the purposes of data readout, the chip is divided into four banks: MM-PAD 2.0, CDO, capacitor flipping pixels, and MM-LDO. The signals controlling each bank are identical. Each bank uses identical but independent readout circuitry. The banks take frames and read out signals in parallel.

Each pixel reports an analog value and a digital value. The analog value is the output of the integrator, and the digital value is the output of the in-pixel counter concatenated with a bit representing the gain state of the pixel. Analog signals are converted to digital signals off-chip. Digitized analog values and digital counts are sent to the FPGA, which controls all signaling to and from the chip. The FPGA communicates with the controlling computer and sends all of the values readout by the ASIC to the computer via Ethernet. The components common to all pixels in the HDR-PAD, including the analog and digital readout chains, are discussed below.

Digital readout chain

The gated oscillator in each pixel, which drives charge removal circuitry, also connects to the input of an 18 bit in-pixel counter. The counter records the num-

ber of times charge removal occurs during an exposure. A global digital control signal, referred to as STOP, prevents the in-pixel counters from incrementing further and defines the end of an exposure from the perspective of the digital components. The counter in each pixel is a ripple counter. Sufficient time for signals to propagate through the counter is provided between the STOP signal and the LATCH signal. The LATCH signal connects each in-pixel counter to a column-wide shift register. The gain status bit in each pixel, discussed in the next section, is also connected to the shift register and is readout in series with the digital counts. The shift register in each pixel consists of 20 bits, 18 bits to which the counter output is latched, one bit for the pixel gain status, and an extra bit which is tied to the digital supply voltage. The pixel shift registers are daisy-chained together to form one large, 320 bit shift register per column.

Once the digital values have been latched into the shift register, an externally provided column select signal activates a digital multiplexer at the top of each bank. The multiplexer connects the output of one shift register to a digital buffer which transmits signals through a wire bond to a second digital buffer off-chip. Each bank has its own multiplexer and dedicated chip-edge buffer so that all four banks can be read out simultaneously. The banks all share the same column select signal. The FPGA supplies a clock which shifts data out of the selected column shift registers and to the FPGA for temporary storage. Once data from all pixels in the selected column in each bank has reached the FPGA, the column select signals switch and the next column is activated. Once all four columns in each bank have been clocked out, digital readout is complete and all digital data has been sent off chip.

Analog readout chain

All pixels in the HDR-PAD use identical but separate analog readout chains. The analog output from each pixel integrator is monitored by an in-pixel sample and hold circuit. The pixel integrating amplifier drives the sample and hold capacitor which is connected to the integrator output node by a switch. The switch is controlled by a global digital signal. Opening the sample switch defines the end of an exposure from the perspective of the analog data. This signal is timed to coincide with the STOP signal which prevents the counter from incrementing. The switch is closed during integration such that the voltage on the capacitor follows the integrator output. Once the switch is opened, the analog value that will be read out is fixed.

The sample capacitor must be large enough that leakage current will not have a significant impact on its voltage within the time scale of readout (microseconds). The sample capacitor must also be small enough to not have a significant impact on the slew rate of the integrating amplifier. A value of 300 fF was chosen based on the impact of this capacitive load on the integrating amplifier in simulation. A five transistor differential amplifier connected in follower configuration reads the sampled analog voltage and serves as the pixel analog output buffer. The pixel analog output buffer was optimized for slew rate, settling time, and noise. Noise in the analog buffer must be minimized to preserve analog signal integrity. A five transistor differential amplifier topology provided the required specifications while minimizing power consumption. This is a class A topology, so the maximum slew rate in one direction is roughly 10 times the maximum slew rate in the opposite direction. Fixed voltage offsets in the buffer output are not detrimental to the operation of this amplifier as they

are trivially accounted for in calibration, so long as they do not push the analog signal outside the functional range of the analog readout chain. Because each pixel contains a pixel output buffer, power consumption must be kept low. Here, quiescent current was kept below $5\ \mu\text{A}$. Rapid settling ensures that readout time can be minimized and frame rate maximized. The precise capacitive load to be driven by this amplifier depends on the full chip layout, but a range of values were explored to ensure proper performance. The pixel output buffer is connected to a column bus via a second switch.

Figure 6.5 is a schematic of the analog readout chain from the sample and hold to the chip edge. The column bus is a low impedance connection between all pixels in a given column. Each column bus connects to the input of another analog buffer, the column buffer. The column buffer output connects to an analog multiplexer. The analog readout is orchestrated primarily by on-chip circuitry which cycles through a fixed pattern of readout signals. After an externally supplied initialization pulse, the analog readout signals increment with each tick of a clock supplied by the FPGA. The signals cycled through are row select and column select. Again, each bank reads out in parallel. A row select signal connects all pixels in a given row to their respective column buses (closing the in-pixel switches connecting the sample and hold buffers to the column buses), and a column select signal activates each column bus connection to the multiplexer in succession. Once a row has been cycled through, the row select increments and the column select signal repeats its cycle.

At the output of the multiplexer, a large class AB analog buffer sends analog signals off-chip through a wire bond. Several class AB topologies were explored for use at the chip edge. The capacitive load driven by this buffer is often on the

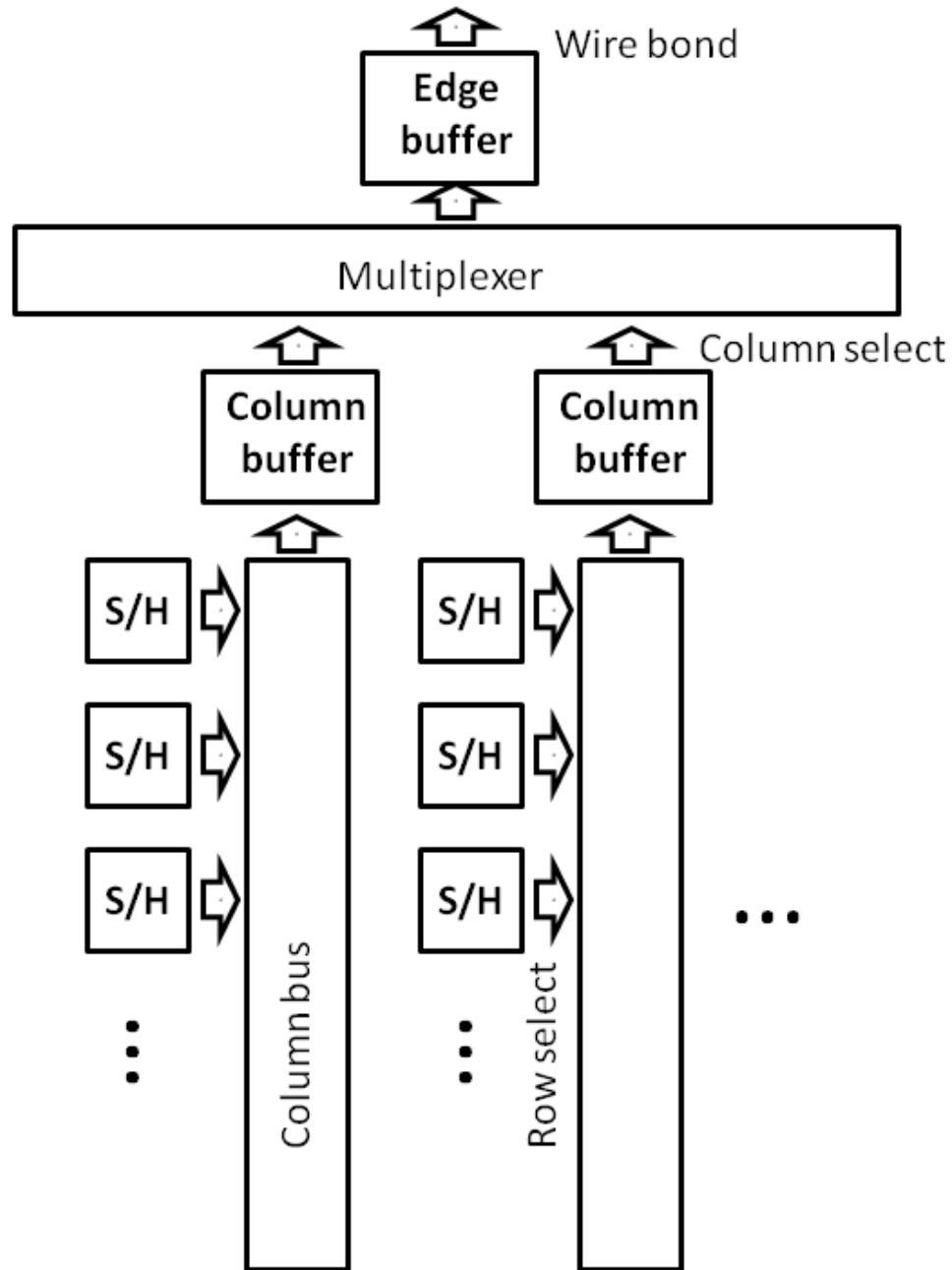


Figure 6.5: Simplified ASIC analog readout chain schematic. Sample and hold circuits in each pixel connect to a column bus through a switch. A row select signal closes this switch and connects all sample and hold circuits in a given row to the column bus. A buffer at the edge of the column bus feeds a multiplexer. A column select signal drives the multiplexer to connect each column buffer to an edge buffer in sequence. The edge buffer sends analog signals off-ship for digitization. Each bank possesses its own copy of the depicted circuitry.

order of picofarads, depending on the wire bond pads, the wire bonds themselves, and the PCB-side analog buffers being driven. 5 pF and 20 pF loads were used in simulation while evaluating various edge buffer designs. Because the chip only contains one edge buffer per bank, performance is generally valued over power consumption. Here we limited edge buffer quiescent current to less than 500 μA . The final design had a quiescent current of 86 μA in simulation. A settling time of 50 ns throughout the range of capacitive loads tested was also required. Stability must be maintained throughout the entire range of loads. Again, a fixed offset in output voltage does not impact performance significantly, but noise added to the buffered signal must be minimized. The chosen topology is based on the AB amplifier used for signal integration in pixels, as described in Chapter 5. The amplifier was modified for enhanced output at the expense of gain. This amplifier provided the necessary slew rate and output swing.

Once analog signals are buffered off chip, they reach another analog buffer. This buffer, on the support PCB, is fully differential and feeds its output to an analog to digital converter (ADC). Each bank has its own off-chip buffer, but all four of the buffers share a common differential reference voltage. The ADCs employed are dual channel, so there are two ADCs on the PCB, and each one is shared by two banks. The analog to digital conversion gain is set by resistors on the PCB. While the resistors are specified with high tolerance, the exact conversion gain must be factored into calibrations. Once analog signals have been digitized, the ADCs are clocked by the FPGA to output the digitized values. The FPGA collects these data and sends them along with the counter output values to the controlling computer via Ethernet.

6.3.3 Adaptive gain implementation

Each pixel's gain state is controlled by an S-R latch circuit. The comparator monitoring the integrator output in each pixel controls the sampling of the latch, and the latch input is always high. When the comparator triggers, the latch samples the input and sets its state to the input level. In this case, sampling closes the adaptive gain switches and the pixel enters the low gain state.

In each pixel, the charge removal capacitor switching is controlled by an AND logic gate. The inputs of the AND gate are the output of the comparator and the output of the adaptive gain latch. A delay element, composed of an inverter chain, sits in series between the latch output and the AND gate input. This ensures that when adaptive gain is triggered by the comparator for the first time in an exposure, the charge removal circuitry is not immediately triggered as well. Rather, the adaptive gain pulls the integrator output above the comparator threshold voltage before the charge removal is executed. Alternatively, if there is sufficient input to keep the integrator output below the threshold voltage in low gain, a charge removal event is required and will be performed shortly after the gain switching.

The latch controlling the adaptive gain is also connected to the 19th bit of the in-pixel shift register which reads out the in-pixel counter output. Because knowledge of the adaptive gain state is required to interpret the analog output, the gain state of each pixel in each exposure must be recorded and readout with the analog and digital data. By tying the adaptive gain control signal to the shift register, the gain state of the pixel front-end is readout along with the count of charge removals and the end of each frame.

6.3.4 Programmable test sources

For functional testing, each pixel contains a programmable current source. The current source consists of a PMOS transistor gated by a second PMOS transistor. The gate voltage of the first transistor is set externally and determines the level of input to the pixel. The source terminal is connected to the analog supply voltage. The second transistor's gate is set by a status bit stored in-pixel. The status bit is set by a specific bit in the pixel's shift register. The shift register bit is written to the in-pixel memory when the digital signal WRITE is high and the digital column select signal is also high. By reading in specific bit patterns to the column shift register and activating column select, arbitrarily specified pixel test sources can be activated.

While reusing the digital readout column select signal for programming in-pixel current sources is efficient in reducing the number of wire bonds required to operate the chip, it was found in testing that digital readout could at times activate in-pixel test sources erroneously. Setting the default level of the WRITE signal to low has helped to address this issue. However, the architecture should be updated in future iterations.

To improve the functionality of the current source, the gate voltage of the PMOS transistor should be set by a current mirror rather than a DAC. That would permit a more controlled and predictable input to pixels. Additionally, as will be seen in Chapter 7, the parasitic capacitance on the pixel front end is quite large. In an effort to minimize this, the transistor gating the current source should be as small as possible.

6.3.5 Radiation hardening

As discussed in Chapter 2, radiation damage in x-ray detectors can lead to long-term, anomalous biasing of transistors. The transistors which are arguably the most sensitive to radiation damage are analog switches. For example, radiation damage in NMOS sample and hold switches leads to leakage current onto or off of the sample and hold capacitor, and therefore a possible inability to properly readout analog signals. In an effort to make the HDR-PAD more tolerant of radiation, enclosed layout transistor topologies were employed in switches deemed most sensitive to radiation damage.

The HDR-PAD is fabricated in TSMC 180 nm CMOS technology (CM018). Thin transistor gate oxides in this technology minimize the risk of long term radiation damage directly beneath transistor gates, but the so-called bird's beak is a vulnerable area that persists in these smaller technologies, as discussed in [75]. Many excellent reviews of enclosed layout transistors exist, such as [76] and [77]. To summarize, by laying out the transistor gate in a ring the regions most vulnerable to radiation damage are drastically reduced. Figure 6.6 demonstrates this layout technique. Note that the gate material can not be confined to the octagonal shape because layout rules dictate that gate contacts cannot be made directly above diffusion zones. Labeled in the figure are additional dimensions required to parametrize the ELT transistor sizing.

Enclosed layout transistors introduce additional geometric considerations which result in transistor sizing constraints. For example, the minimum ELT width is more than four times that of a linear transistor in the same technology. A geometric model similar to the one proposed in [76] was used to predict effective width/length ratios of ELTs in this work. Computed values were com-

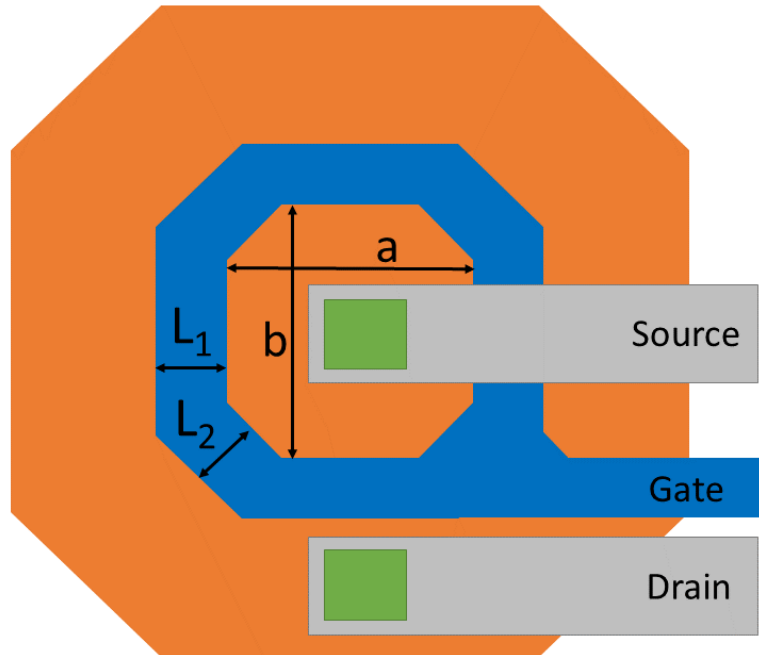


Figure 6.6: Schematic of an enclosed layout transistor (ELT) with source, gate, and drain terminal connections labeled. Additional dimensions are required to parametrize the transistor. Rather than simply a length and a width, two lengths and two widths are required, labeled as L_1 , L_2 , a , and b where L 's are lengths.

pared to widths and lengths of ELTs extracted from layout and agreed well. In this work, NMOS ELTs were used as sample and hold switches, pixel reset switches, and adaptive gain switches. Each of these switches are sensitive to leakage current.

These switches are all connected to capacitors which hold analog values, and are therefore sensitive to charge injection. Charge injection through CMOS switches, sometimes referred to as clock feed-through, can pose a serious problem to the fidelity of analog signals. The topic is discussed and modeled in [78–80]. To summarize, as discussed in Chapter 2, a conductive channel forms beneath the gate of a transistor in saturation, as is the case when a CMOS switch is closed. When the switch is suddenly opened, the charge which formed the channel must go somewhere. Because the channel to drain and channel to source

junctions are effectively forward biased, charge injection into the substrate is negligible and channel charge enters the source and drain nodes. Additionally, the gate overlap capacitance with the source and drain form charge pumps which are activated by switching signals.

If the source or drain are connected to nominally floating nodes, the charge injection will affect the voltage on these nodes. This is a problem for integrating detectors. In an effort to minimize the impact of charge injection, the dummy switch technique was employed as described in [81]. In this scheme, two half-size dummy switches are placed, one on either side of the active switch. The dummy switches are the same type as the active switch and are shorted so that they do not affect conduction in any way. They are driven by the complement of the active switching signal. Because the dummy switches are always making a transition which is opposite the active switch, the charge that they inject is the opposite of the charge injected by the active switch. Because their gate area is half that of the active switch, the injected charge will be canceled provided that the active switch charge injection is split evenly between the source and drain. Figure 6.7 illustrates the concept of dummy switches for charge injection compensation.

Note that the use of ELTs necessitates larger gate areas than would otherwise be dictated by process design rules. This results in larger than average charge injection, and thus the compensation provided by dummy switches is of greater importance. The HDR-PAD uses especially large switches to deal with large signals. How effective the dummy switch compensation is depends on several factors. The ON impedance of the active switch, along with the rate of active switch signal change, dictates the degree to which the two sides of the switch

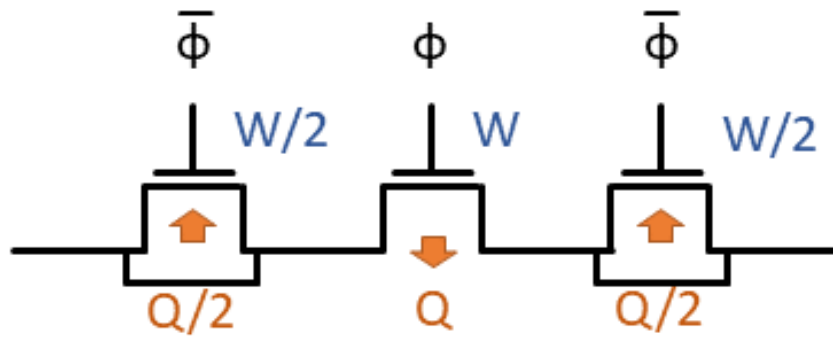


Figure 6.7: Dummy switch compensation schematic. The active switch is flanked by two half-sized switches. The half sized switches are shorted so that they do not control any connections between nodes. They are driven by the complement of the active switching signal which results in opposite charge injection of the active switch. If the charge injected by the active switch is split evenly between the nodes it connects, the net charge injection of each node should be zero.

can equalize their respective voltages through channel conduction. Equal division of injected charge between the source and drain is not guaranteed however. The partitioning of charge between the source and drain of the active switch is dependent on the relative capacitances of these nodes. If sharper clock edges are used however, a more equal partitioning of charge can be achieved.

Perhaps the most confounding factor to be dealt with in regard to dummy switch charge injection compensation in the HDR-PAD is the relative switching times of the active switch versus the dummy switches. This has a strong effect on the ability to cancel injected charge, as discussed in [81]. In the HDR-PAD, digital input signals from off-chip are buffered at the chip edge, and their complement is generated alongside the buffered signal. This introduces an unavoidable delay between the two signals. The effect of charge injection from switches will be examined more closely in Chapter 7. In future detectors, if pin count is not problematic, digital signals and their complement can both be generated off-ship, which would permit tweaking and fine-tuning of delays be-

tween them. If this is not possible, it may be beneficial to add delay circuitry to the chip edge digital buffers which would minimize the delay between the two signals.

CHAPTER 7

HDR-PAD CHARACTERIZATION

7.1 Introduction

Establishing basic functionality of the system takes considerable effort, but once established, system performance must be evaluated. Below, the evaluation of the HDR-PAD is described. Basic operating parameters are extracted from dark current integration measurements and low flux x-ray exposure. Ultimately the detector attempts to measure a direct synchrotron x-ray beam to test high flux signal integration. The HDR-PAD in its present state does not have the sensitivity to small signals that was originally specified by the design goals, and contributing factors to this are examined. The infrared laser used in the work described in Chapter 4 became inoperable shortly after the pulse work concluded, and so no tests of the HDR-PAD with very high instantaneous flux were performed.

Performance of the MM-PAD 2.0 pixels, the capacitor flipping pixels, and the MM-LDO pixels will be examined, but the CDO pixel operated inconsistently and will therefore not be discussed. The analog output of the CDO pixel in any frame with an integration time longer than ~ 1 ms was at or above the highest voltage measurable by the analog to digital converter. This implies that the front-end integration node of the pixel reached a low value. This is supported by the influence that this bank had on adjacent pixel columns. It can be seen that pixels adjacent to the CDO bank received less signal than other pixels in the same bank under constant external input. Some parameters of the CDO pixel could be extracted, but due to lack of performance in most tests, there will

be no further discussion of the pixel in this chapter.

7.1.1 Dark current integration

To get a picture of the pixels' overall performance and functionality, dark current integration is a useful tool. Recall in Chapter 2, dark current from photodiode sensors was discussed. While the signal from the sensing layer itself is often a nuisance, it can serve as a useful diagnostic. The dark current from the sensor is a low level, relatively steady input.

By taking a series of frames with linearly increasing integration times, we can track the pixel output as a function of input. Recall that dark current is exponential in temperature. Here the detector was held above room temperature (at 30°C) and the sensor bias was raised to 110V, roughly 30V higher than the bias required for sensor depletion. These factors increase the total dark current, and therefore decrease the integration time required to initiate adaptive gain and charge removal circuits.

Figure 7.1 depicts the output from an MM-PAD 2.0 pixel as a function of exposure time. Similar plots were obtained for all pixel variants and all look essentially the same. In these measurements, the CDO pixel output begins at the expected level, but rises steadily to a maximum output over the course of 500 μ s, indicating that the front end is approaching ground.

At first glance, the output plotted in figure 7.1 verifies that the pixel is integrating photocurrent as expected. The sensor is biased for hole collection, so the output slews down in time. Once $V_{out} = V_{th}$, roughly 4800 ADU here, the

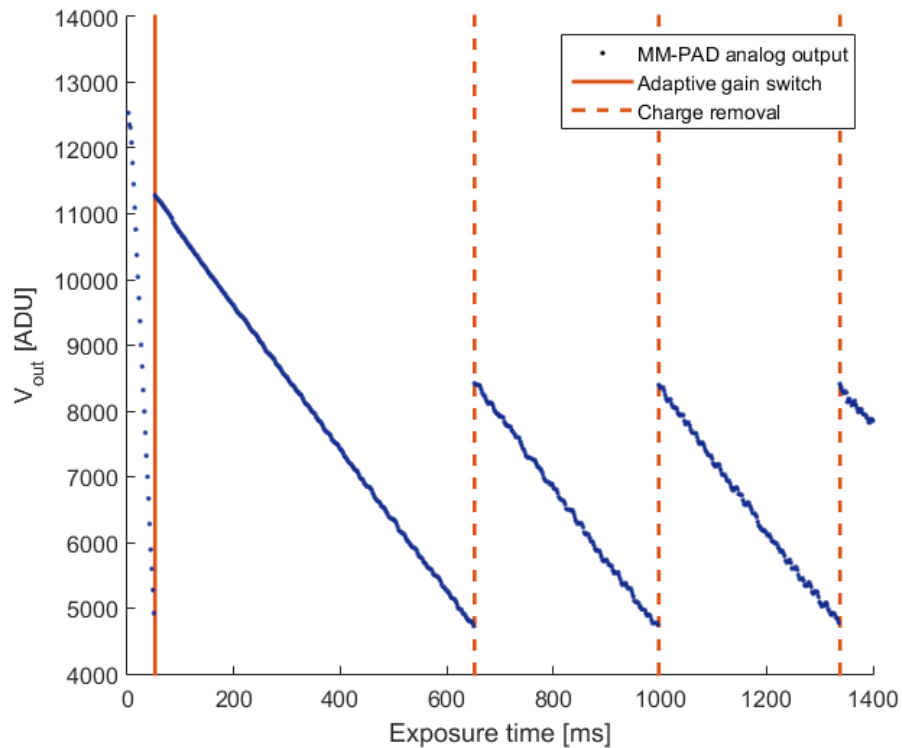


Figure 7.1: Average MM-PAD 2.0 pixel output as a function of exposure time. The pixel input is sensor dark current, which is relatively constant, so exposure time corresponds linearly to total integrated signal. Basic operation of the pixel is evident. Positive charge accumulates on the integration node, causing the integrator output to decrease in voltage. Once $V_{out} = V_{th}$ (roughly 4800 ADU) the adaptive gain is triggered (at 50ms), and the pixel continues to integrate. When $V_{out} = V_{th}$ again, charge removal occurs (first at 650ms).

adaptive gain is triggered. The output jumps back up and the integrator output is pulled away from the threshold voltage. The pixel continues to integrate dark current, but the slope of the line has changed indicating that the gain of the pixel has changed. Subsequent approaches to the threshold voltage by the integrator output result in output jumps which correspond to charge removal events, as verified by the pixel digital output.

Dark current is integrated by all pixel simultaneously, and the measurements provide a broad verification that the pixels are functioning as intended under

non-strenuous conditions. A lot of information can be pulled from these plots. The switching point in ADU of each pixel can be extracted from these measurements. Specifically, the ADU values at which adaptive gain/charge removal is triggered, and the ADU value to which the pixel returns after either of these events are needed to interpret pixel output. This is a direct measurement of ΔV , the change in voltage which occurs on the integration node with each charge removal event, which is essential to interpreting high signal measurements. Note that the value of ΔV is only known in ADU at this point.

Furthermore, the ratio of the slopes of integration in high vs. low gain provide valuable information as well, assuming that the pixel input remains constant in both states. These slopes allow the low and high gain to be calibrated relative to each other. Because the average input current is not a known quantity in these measurements, the absolute gain can not be reliably pulled from these frames. What we wish to know is the change in voltage (or ADU) of the output as a function of input charge. To measure this empirically, we need a known input. This is provided by x-rays as discussed in the next section.

Interestingly, the gain ratios obtained do not correspond exactly to the ratios expected based on total integration capacitance. Instead, the ratios consistently yielded numbers which imply a high gain integration capacitance closer to 60 fF in all pixels, rather than the 40 fF expected. This can be understood as an effect of parasitic capacitance on the front end decreasing the charge collection efficiency of the integrating amplifiers, as discussed in Chapter 2. The HDR-PAD pixels each contain a protection diode which prevent the front end voltage from rising significantly above the supply voltage. The diodes were intended to protect pixels from damage that may occur with very high instantaneous flux

inputs. These diodes are quite large, as the pixels were intended to be tested with XFEL like inputs. They may be contributing much of this parasitic capacitance, along with the detector sensor and bump bonds. Future pixels should consider utilizing much smaller protection diodes to minimize this effect. If the detector in question is not intended for use at XFELs, no protection diode may be required at all.

7.1.2 Photon histograms

Another effective means of assessing a detector's performance is with low fluence exposure to radiation. After confirming that the HDR-PAD responds to radiation as expected (initial tests were performed with exposure to americium radiation), the HDR-PAD was mounted on a beamline in the Gruner lab to be exposed to silver $k\alpha$ x-rays from a tube source. X-rays passed through a graphite monochromator to select for the characteristic 22.16 keV x-rays.

Recall that x-rays absorbed on boundaries between pixels can split the photo-generated charge between pixels. In this calibration, we would like to deposit a known quantity of signal in a pixel. Even with a monochromated source, charge sharing needs to be addressed. Here we used a tungsten mask with an array of 75 μm holes with a 450 μm pitch to shield most pixels from radiation. Pixel pitch on the HDR-PAD is 150 μm , so properly aligning the mask with the pixels ensures that the nearest neighbors of illuminated pixels receive no signal. Signal measured in illuminated pixels is generally not shared with neighbors because the mask was positioned with mask holes centered on pixels, as depicted in figure 7.2.

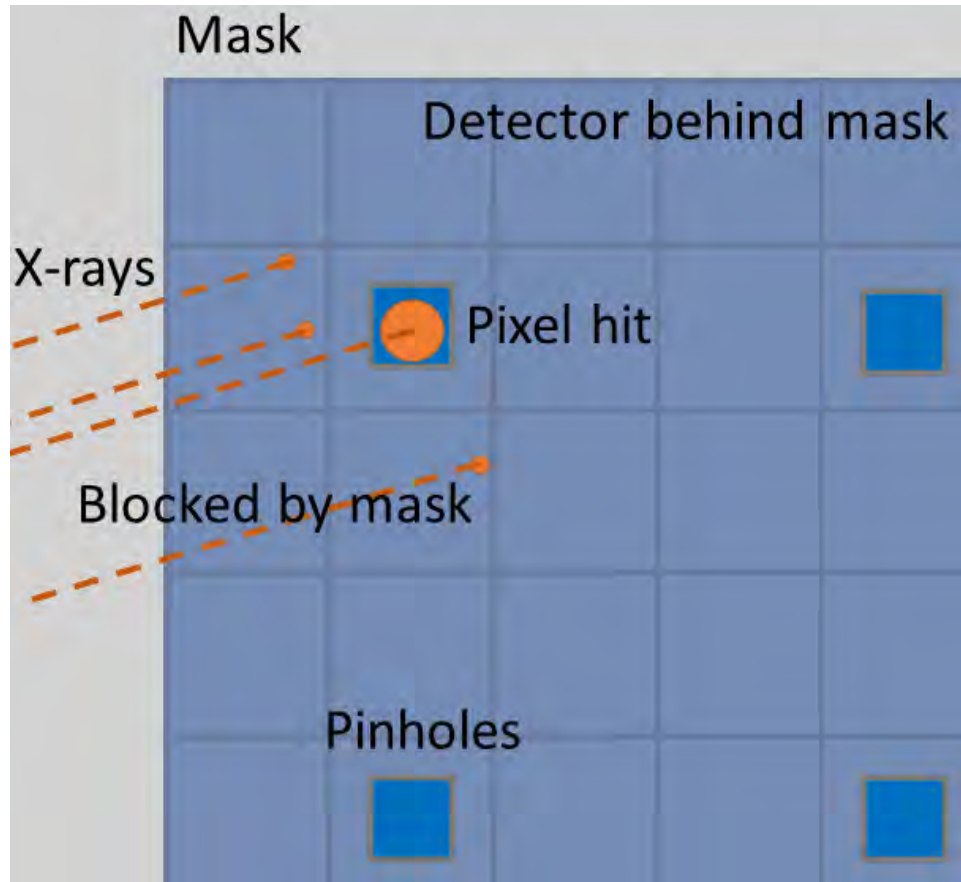


Figure 7.2: Cartoon depiction of pinhole mask alignment. Pin holes are smaller than pixels and spaced more than one pixel width apart. Aligning the pinholes over the center of pixels ensures that the signal from each photon absorbed by a pixel is not shared with neighboring pixels.

In this configuration, the signal received by illuminated pixels should arrive in integer multiples of 22.16 keV, and the relative frequency of each multiple should follow a Poisson distribution. Figure 7.3 is a histogram of 25,000 analog outputs from a single MM-LDO pixel on the HDR-PAD with 1 ms exposure times. The data has been reversed such that decreases in output correspond to increases in ADU. Plotted on top of this histogram is a fit incorporating the constraints indicated by our knowledge of the system.

The fitted function is the sum of some number of Gaussian functions, in this

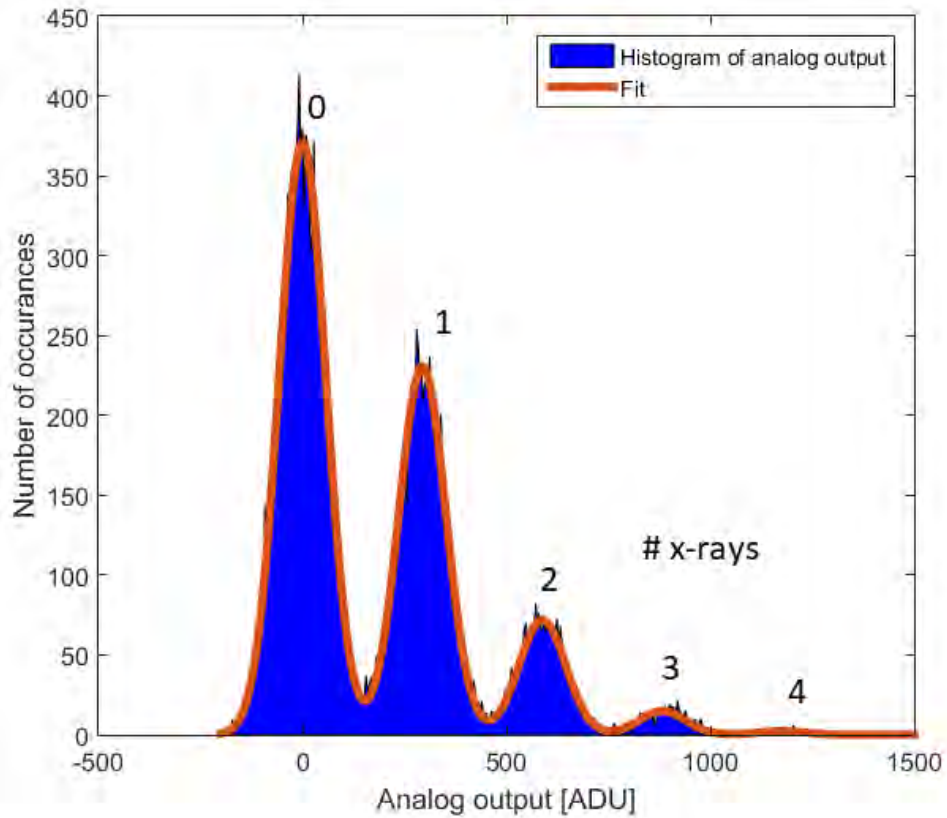


Figure 7.3: Histogram of 25,000 analog outputs from an MM-LDO pixel with low flux silver $k\alpha$ radiation. Exposure time was 1 ms. The histogram is fit by a sum of five Gaussian functions. Parameters from the fit describe the pixel's gain and noise characteristics. Peaks corresponding to integer numbers of photons absorbed by the pixel in the integration window are labeled.

case five:

$$fit = \sum_{n=0}^4 x_4 e^{-x_3} \frac{x_3^n}{n!} \exp\left(\frac{-(nx_2 - ADU + x_5)^2}{2x_1^2}\right). \quad (7.1)$$

Each Gaussian corresponds to an integer number of photons arriving at the pixel within the integration window. Each Gaussian has the same width, which corresponds to the variability in the output of the detector. This width is a fit parameter (x_1) that provides a measure of overall noise in the analog data chain. The Gaussians are evenly spaced. The space between Gaussians is the signal generated by one 22.16 keV x-ray in ADU. This is a fit parameter (x_2) and is an absolute measure of the pixel's analog gain. The relative heights of the Gaus-

sians follow a Poisson distribution described by a fit parameter (x_3). This parameter describes the average flux incident on the pixel in question. Fit parameter x_4 is effectively a normalization corresponding to the number of frames contributing to the histogram, and x_5 is an offset equivalent to background subtraction.

In this case five Gaussian functions were fit to the histogram because there were not an appreciable number of occurrences of more than four photons incident on the pixel within the integration window, but in higher flux data sets the sum extends to higher numbers. The first peak in the histogram corresponds to zero integrated photons. The width of this Gaussian is roughly equal to the others, confirming that the vast majority of analog signal variation originates in the detector itself.

Photon histograms were obtained for pixels in all banks and were analyzed in the manner described above. Table 7.1 summarizes the pixel data extracted from photon histograms. The ADU/keV figure is the total effective gain of the analog signal chain when the pixel is in high gain mode, including effects from the analog buffer chain and the off-chip ADC. This number is the absolute measurement of pixel gain required to utilize the slope ratio discussed in the previous section. For example, in high gain the MM-PAD 2.0 pixel out changes by 13.29 ADU per keV of signal incident, so an 8 keV x-ray will change the output by 106.32 ADU on average. The ratio of high gain to low gain constant current integration slopes from the previous section is 15.1, which implies that an 8 keV x-ray will change the output of the MM-LDO pixel output by ~ 7 ADU on average in low gain.

σ_{fit} is the fit parameter x_1 and characterizes the variability of the analog output. The number is listed in ADU and keV (utilizing the extracted gain). The

Table 7.1: Parameters extracted from photon histograms

Pixel	Gain [ADU/keV]	σ_{fit} [ADU]	σ_{fit} [keV]
MM-PAD 2.0	13.05	72.0	5.51
Capacitor flip	7.67	56.8	7.40
MM-LDO	13.29	72.9	5.48

σ_{fit} in keV indicates that the signal to noise ratio of a single 8 keV x-ray is not much larger than one. While measurements can still be made with 8 keV x-rays, the rate of false positive events in the single photon signal regime is greater than desired, 1.46 in the case of the MM-LDO pixels. For the sake of comparison, the original MM-PAD detector achieves a signal to noise ratio of ~ 6 for 8 keV x-ray inputs, which corresponds to a false positive count rate of less than one in one hundred million. The noise of the HDR-PAD has been improved since these measurements were taken, but the design specifications were not met in this regard. The final section of this chapter is dedicated to exploring this issue.

As an additional verification of pixel functionality, figure 7.4 compiles photon histograms from a set of MM-LDO pixels with progressively higher flux. Individual photon resolution at 22.16 keV is maintained up to the point at which the adaptive gain circuitry activates. The full well in high gain, or the quantity of charge required to initiate the gain switch, matches the expected value.

7.1.3 High flux measurements

Having verified basic functionality of the detector and extracted parameters from the dark current integration and low flux x-ray integration, The HDR-PAD must be tested with a high flux input. Working with Jacob Ruff from CHESS

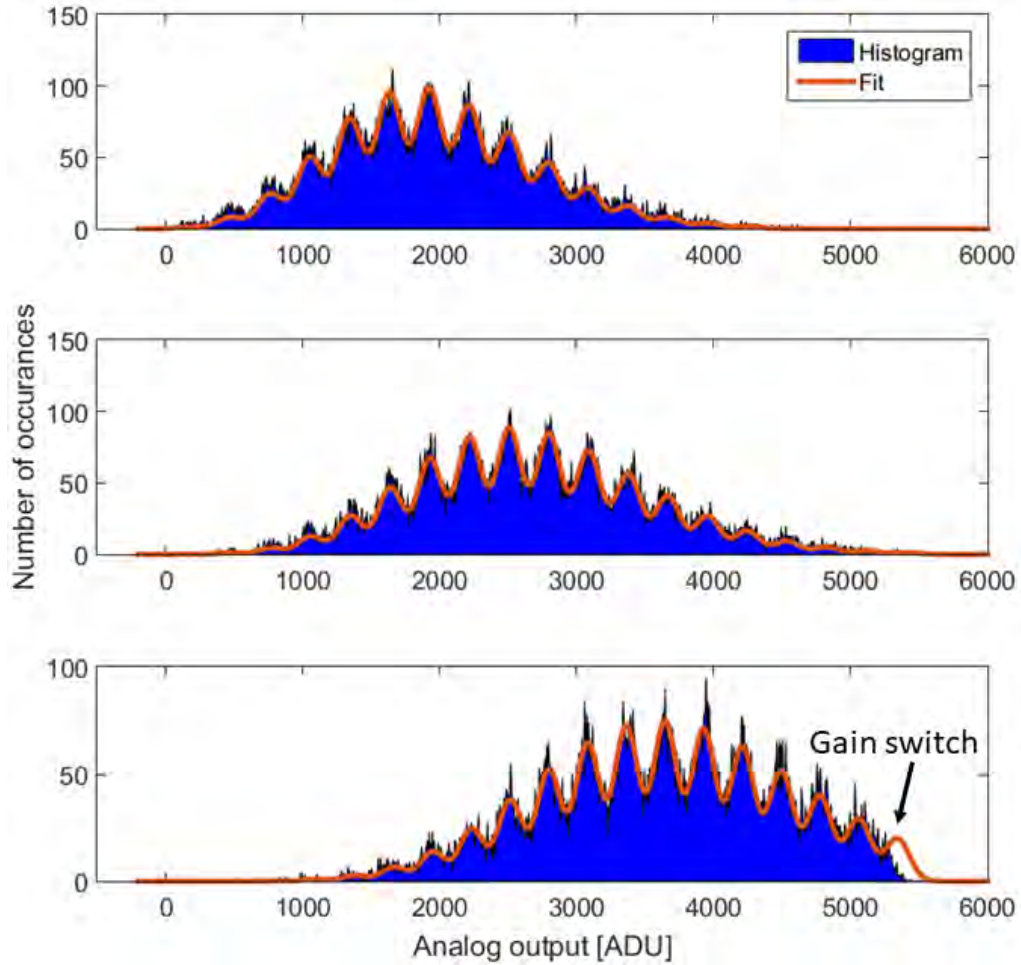


Figure 7.4: Photon histograms of MM-LDO pixels with progressively higher flux. Photon peaks are fit from zero photons up to twenty-one photons. A final peak was added where a twenty-second peak would sit. This signal level triggers the adaptive gain circuitry and brings the pixel integrator output away from the threshold voltage.

at Cornell University, the HDR-PAD was mounted in experimental hutch A2. Beam energy was set to 9.520 keV. The energy was chosen because it provides the highest monochromatic flux from the A2 undulator amongst energies below 12 keV. Higher energies could have provided greater total flux, but the total dose absorbed by the HDR-PAD silicon sensor would have been lower due to the efficiency of silicon at these energies. Beam size was set by beam defining slits to roughly 250 μm by 1500 μm . Total flux was $\sim 7 \times 10^{11}$ x-rays/s as measured

by ion chambers between the beam defining slits and the detector.

Figure 7.5 is a schematic of the experimental layout. IC1 is an ion chamber which monitors the full flux entering the hutch, after the beam defining slits. IC1 feeds back to the silicon monochromator which sets the beam energy. The monochromator adjusts its alignment to maintain constant flux as CHESS beam current changes. A variable aluminum attenuator reduces beam intensity. The attenuator is an aluminum disk with blind slots of various depths bored around the circumference. One slot is a hole cut completely through the disk to permit the full beam to pass with no attenuation. The attenuator is on a rotation stage to allow selection of attenuator thickness. A second ion chamber (IC2) monitors the flux of the attenuated beam. The ion chambers are filled with nitrogen and have kapton windows. Finally, the HDR-PAD is mounted on translation stages in-line with the beam. The translation stages allow positioning of the beam onto different sets of pixels. The rectangular beam was oriented with the long edge along pixel banks. Figure 7.6 is one frame with no attenuation. The full CHESS beam is being integrated for 1 ms. The scale is logarithmic.

Exposure times throughout the measurements ranged between 10 μ s and 10 ms. To ensure activation of the charge removal circuitry at a wide range of beam intensities while minimizing effects of dark current, an exposure time of 1 ms was used in most of the data sets described below. Data sets were acquired as follows: Frames were taken at low flux (high attenuation setting) to align the beam with a desired set of pixels. Once the beam was aligned, the HDR-PAD was set to frame continuously for several minutes. While the detector was taking frames, the attenuator was set to some value, the hutch shutter was opened, and after a delay, the hutch shutter was closed, and the attenuation

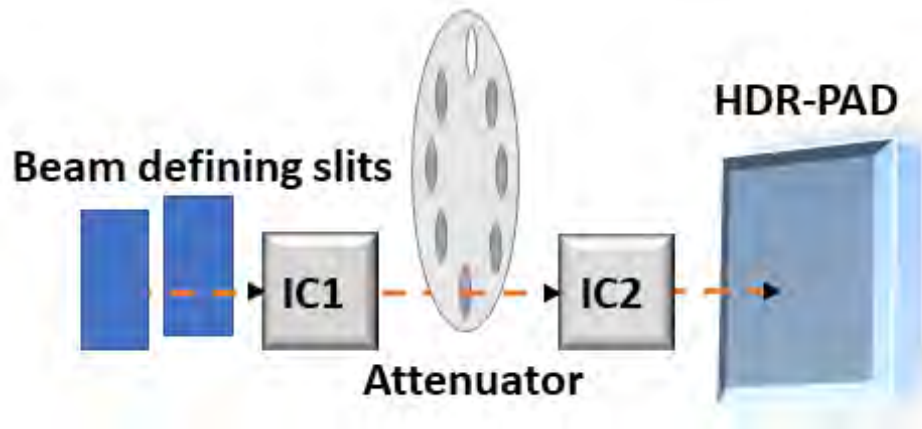


Figure 7.5: CHESS A2 beamline schematic. Beam enters the hutch through beam defining slits and enters the first ion chamber (IC1) which measures the full beam flux. A variable attenuator rotates to place aluminum of various thicknesses in the path of the beam. A second ion chamber (IC2) measures the attenuated flux. The attenuated beam strikes the HDR-PAD directly.

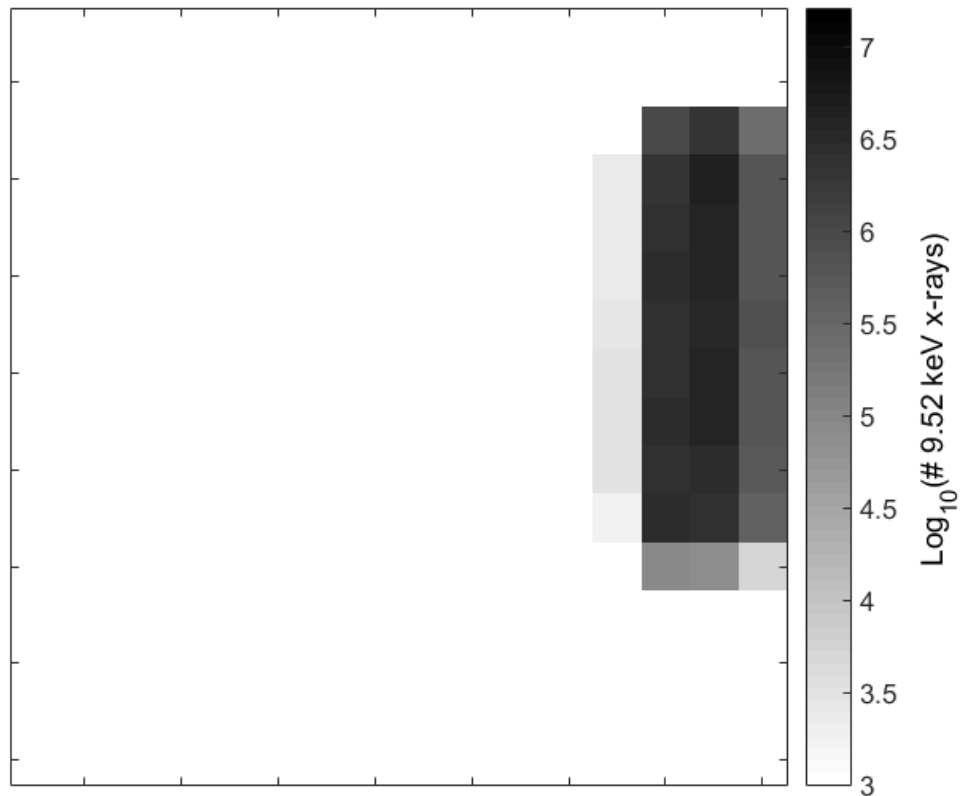


Figure 7.6: Sample image with 1 ms exposure to the full A2 beam. The scale is logarithmic.

setting was incremented. In this way, dark frames are acquired between each set of exposures.

Each bank was subjected to the full range of x-ray flux available, more than five orders of magnitude range. Flux on the peak pixel was calculated. Flux on the entire bank was also calculated. The fraction of total signal measured by the detector versus the signal of the brightest pixel was computed and used to scale the independently measured total attenuated flux incident on the chip. Plotted below are the signals as measured by the HDR-PAD pixels versus the signal as measured by the ion chambers, scaled by the calculated fraction. The error bars are the standard deviation of measurements at each flux based on the frames acquired (generally about 50 frames per data point). An orange dashed line is included for comparison which is the flux as measured by the ion chambers versus itself, a line of slope one, representing perfect performance.

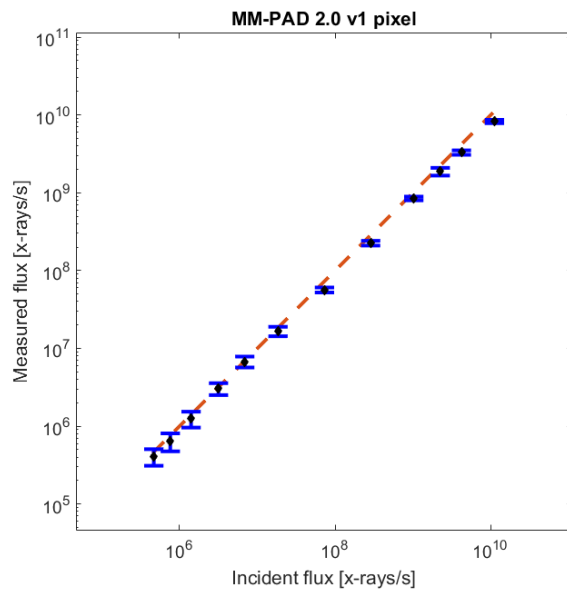


Figure 7.7: Signal measured by the MM-PAD 2.0 pixel with a total integration capacitance of 880 fF versus the signal measured by ion chambers. The dashed line represents perfect performance for comparison.

Figure 7.7 plots the flux measured by the MM-PAD 2.0 v1 pixel (v1 corresponds to $C_{int} = 880$ fF). The pixel performs extremely well, and little deviation from the expected behavior is observed.

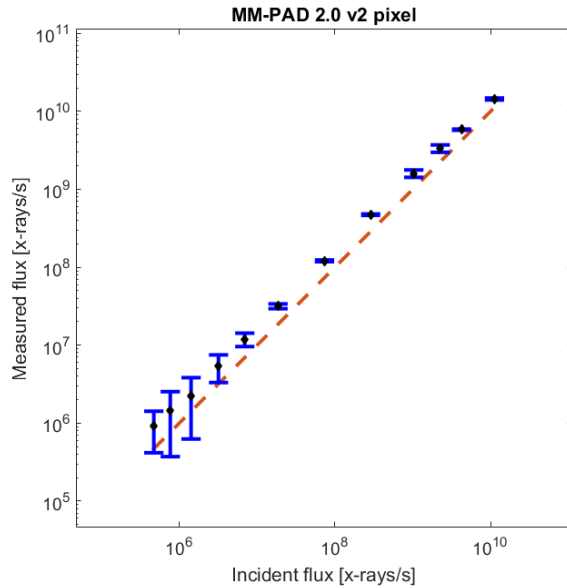


Figure 7.8: Signal measured by the MM-PAD 2.0 pixel with a total integration capacitance of 2630 fF versus the signal measured by ion chambers. The dashed line represents perfect performance for comparison.

Figure 7.8 plots the MM-PAD 2.0 v2 pixel measurements (v2 corresponds to $C_{int} = 2630$ fF). Here the measurements are systematically over estimating the incident flux. The most likely explanation is a slight miscalibration. The ADU to keV ratio used to interpret these data was extracted from the dark current integration and photon histogram measurements discussed above. Because the detector response is so linear, it seems unlikely that the pixels are malfunctioning. The value which represents the number of x-rays removed from the integration node with each capacitor switching event may be less than the original calibration implied. A more careful calibration of the pixel response would most likely yield better agreement between the measured input and the actual input.

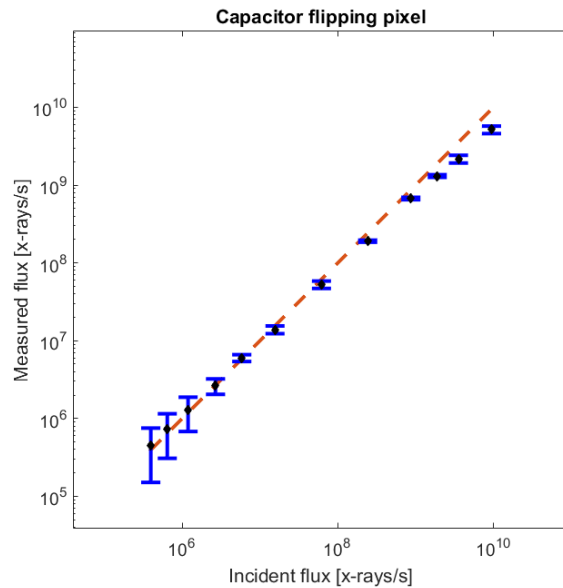


Figure 7.9: Signal measured by the capacitor flipping pixel with an externally supplied threshold voltage versus the signal measured by ion chambers. The dashed line represents perfect performance for comparison.

Figure 7.9 plots the response of the capacitor flipping pixel with an externally supplied threshold voltage. It also exhibits very linear performance. Measured signal at the high flux end begins to dip. It is unclear whether this is a delay induced error, as was explored in Chapter 5, or simply a slight miscalibration of the pixel response. In either case, the pixel would benefit from further calibration, but performs well within the tested range of flux.

Figure 7.10 plots the capacitor flipping pixel response with dynamic thresholding activated. Here a clear drop off in response is seen, and the performance is actually worse than in the externally thresholded case. The reason for this is most likely poor performance of the level shifting circuit. Even in low fluence testing, the circuit exhibited a tendency to switch sporadically, possibly due to a sensitivity to transients. The level shifter may require supplementary reset signals for optimal performance, but these have not been fully implemented.

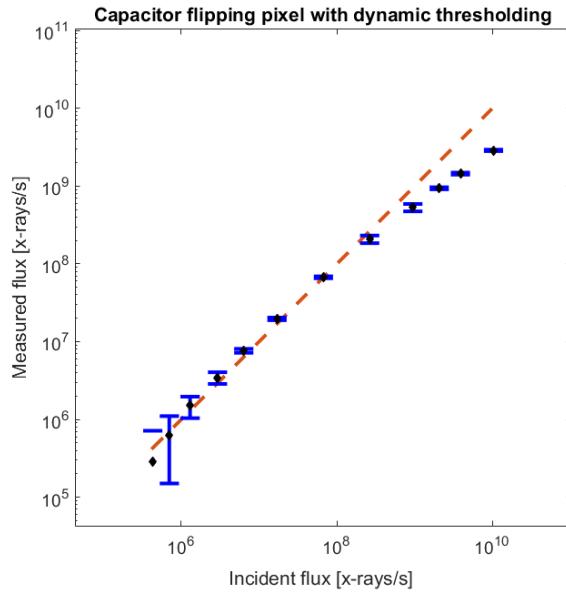


Figure 7.10: Signal measured by the capacitor flipping pixel with dynamic thresholding enabled versus the signal measured by ion chambers. The dashed line represents perfect performance for comparison.

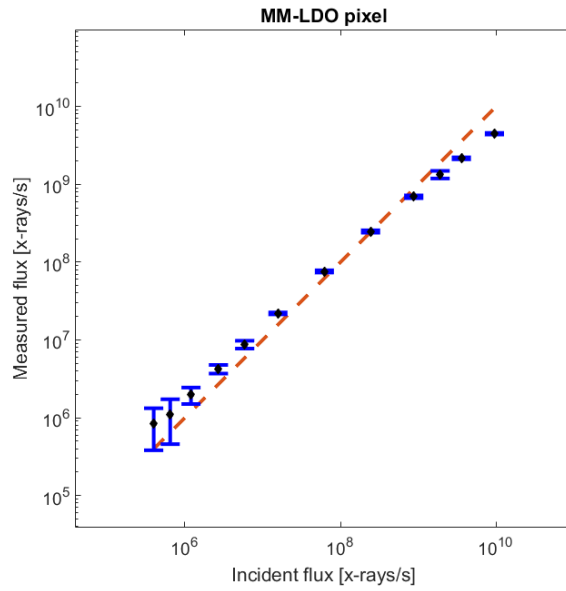


Figure 7.11: Signal measured by the MM-LDO pixel versus the signal measured by ion chambers. The dashed line represents perfect performance for comparison.

Finally, Figure 7.11 plots the response of the LDO pixel. While the response does appear linear, the slope of the measured input is consistently less than one. This is most likely due to an inadequate calibration of the low gain ADU to keV ratio.

Note that while the input to the pixels should be fairly constant, there are variations in beam flux throughout the course of measurement. Some of the uncertainty in the measured inputs can be attributed to these fluctuations. The beam intensity was stabilized by ion chamber feedback on the monochromator, but ion chamber measurements bring their own uncertainties, and feedback systems have characteristic time scales over which they operate. Overall, the system would benefit from further calibration and refinement of data interpretation. The parameters used to interpret these data were obtained empirically, but some refinement of calibration data could yield better results. Even so, the detector responds well to a very wide range of signals, through the full five orders of magnitude tested, up to 10^{10} 9.52 keV x-rays per pixel per second. The MM-PAD 2.0 pixel architecture demonstrates the most reliable performance.

7.2 Small signal resolution

The photon histogram data indicated that the signal to noise ratio of HDR-PAD pixels with signals generated by single 8 keV x-rays is unsatisfactory. In contrast to the well defined, separate peaks in figure 7.3, an analogous plot with 8 keV x-rays would feature Gaussian curves which are only distinguishably separate at their peaks, if at all. As discussed in Chapter 2, noise sources in detectors are abundant, but we can perform tests to identify the dominant sources.

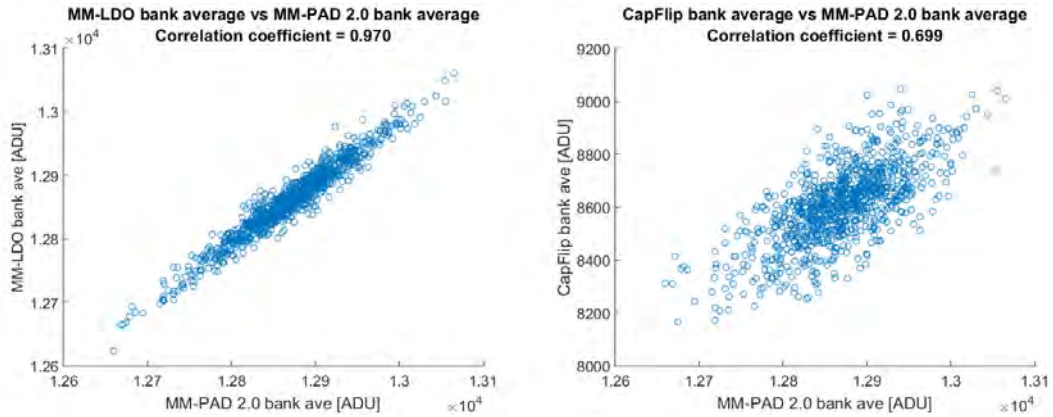


Figure 7.12: Pixel bank average versus pixel bank average. Each point represents one frame. Bank averages from within the same frame are compared. Correlation coefficient is computed.

7.2.1 Global noise sources

To begin, some noise sources are global, while others are local to pixels. Another way to say this is that some portion of the variability in pixel output is common to all pixels, while another portion differs from pixel to pixel. Figure 7.12 is a simple illustration of this phenomenon. Each point in the plots represents one frame. The horizontal position is dictated by the average analog output value of one bank of pixels, and the vertical position is the average analog output value of another bank of pixels. Exposure time was 10 μ s, kept low to minimize the effect of dark current on the measurement.

A clear correlation is seen between banks. The MM-PAD 2.0 bank and the MM-LDO bank are strongly correlated. This is to be expected because the pixel architectures are nearly identical, and so global noise sources are likely to affect these pixels in a similar way. Global noise sources include power supply and bias fluctuations, as well as pick up from external sources, among others. These will be investigated in turn. First we might ask what fraction of the pixel noise

can be attributed to global fluctuations?

If pixel noise were entirely independent between pixels, i.e., there are no global fluctuations, an average of many pixels should vary less from frame to frame than a single pixel output varies between frames. More rigorously, the variance of the mean of a set of pixels in time is

$$\text{Var}\left(\sum_{i=1}^N \frac{x_i}{N}\right) = \frac{1}{N^2} \left[\sum_{i=1}^N \text{Var}(x_i) + \sum_{i \neq j}^N \text{Cov}(x_i, x_j) \right] \quad (7.2)$$

Where i and j index the pixels in the set to be averaged, Var is the variance of the values over time, and Cov is the covariance of the values over time. Note that the covariance of a variable with itself is equal to its variance. If the pixels lack any correlation, i.e., their covariance is zero, the variance of the mean of pixels should equal the sum of the individual variances divided by N^2 , or equivalently the mean of the variances divided by N .

Figure 7.13 looks at this comparison. Standard deviations are plotted rather than the variances in equation 7.2 to make a clearer connection to equivalent noise charge. A set of 10,000 frames with 10 μs exposure time were acquired. In each frame, N MM-PAD 2.0 pixels were selected and averaged together. The standard deviation of the average value throughout the data set is plotted with a blue dotted line. The variance of the output of each of the individual pixels in the data set is also computed, and the variances are averaged and divided by N . This is repeated 5000 times for each N and the square root of overall average results is plotted. To reiterate, this plot compares the standard deviation of an average:

$$\text{dotted} = \sqrt{\text{Var}\left(\sum_{i=1}^N \frac{x_i}{N}\right)}, \quad (7.3)$$

versus the square root of the average of individual variances divided by N :

$$\text{dashed} = \sqrt{\frac{1}{N^2} \sum_{i=1}^N \text{Var}(x_i)}. \quad (7.4)$$

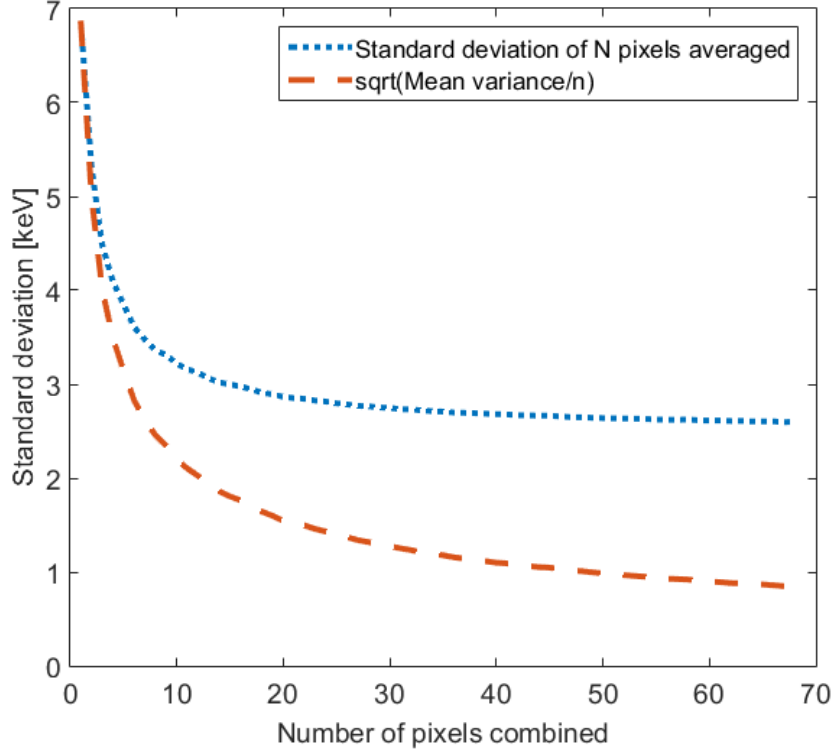


Figure 7.13: The standard deviation of N pixels averaged together is plotted as a blue dotted line. The average standard deviation of N pixels divided by N is plotted as an orange dashed line. If there were no global noise, the standard deviation of the average value of many pixels would approach zero as N increases.

For independent random variables x_i , every term in the covariance sum is zero. The orange dashed line approaches zero as $\frac{1}{\sqrt{N}}$ while the blue dotted line approaches the standard deviation of the global noise.

Where does this global noise come from? To simultaneously assess the variability of power supplies and bias voltages along with analog to digital conversion noise, the chip was removed from the ZIF socket and power supplies and bias voltages were connected directly to analog output channels in the ZIF socket, which feed to the ADC inputs. For supply voltages outside the normal range of ADC operation, the supply was connected to the output channel through a resistive bridge consisting of two 1000Ω resistors to ground. This

places a load on the supplies which is within their normal operating range. By sending frame commands to the FPGA while the PCB is wired in this configuration, the ADCs will continuously digitize the voltage at their input. This provides a measure of both fluctuations in supply/bias voltages and variability in analog to digital conversion.

If the result of this test were very high variability, further steps would be required to disentangle the source of the variance. However, what was discovered was a clear, high frequency fluctuation in the supply voltages, but not the bias voltages. This indicates that there is noise on the power supply lines, but the ADCs are operating reasonably well. It was discovered that the capacitors connected to the power regulators on the PCB had a lower equivalent series resistance than what is required by the regulators for stability. After replacing these capacitors, the digital supply line was the only noisy line remaining. Replacing the FPGA switching power supply with a linear power supply unit aided the reduction of this variability drastically. Table 7.2 lists the standard deviation of power supply and bias voltage analog to digital conversion values after these changes. These measurements suggest the degree to which power supply fluctuations might affect the variability of frame data from the ASIC, though the actual impact is most likely smaller than the figures themselves.

Note that in this configuration, the power supplies are not loaded dynamically, as they would be in actual operation. As a result, power supply droop resulting from changing current draw by the ASIC can not be diagnosed in this way.

To assess whether noise on the digital line is originating on the supply side or ground side, the measurements above were repeated with the analog power

Table 7.2: Power supply variability

Supply	σ [ADU]
MM-PAD 2.0 V_{ref}	2.21
Charge dump oscillator V_{ref}	1.98
Capacitor flip V_{ref}	1.25
MM-LDO V_{ref}	2.69
Analog supply voltage	1.50
Digital supply voltage	12.89

supply connected through the resistive divider to digital ground and with the digital power supply connected to analog ground. This crossing yielded standard deviations on both supplies of ~ 6.5 ADU, suggesting that the problem is not solely on either the supply or ground side. Rather, it is more likely that a digital component on the FPGA or PCB is generating fluctuations on both.

Finally, noise contributions of the Peltier thermoelectric used to regulate the temperature of the ASIC were assessed by imaging at room temperature with and without the Peltier turned on. Significant pickup was measured with the Peltier activated, though the noise was reasonably well addressed with a debounce algorithm.

In general, global noise can be mitigated with a so called debounce algorithm. By averaging the value of pixels which receive no external signal in a given frame, an estimate of the global noise is obtained. This value can then be subtracted from all pixels to remove the global component of noise on a frame-by-frame basis. While this technique was employed to address the remaining global noise in the HDR-PAD, its effectiveness was limited due to the variety of pixels in the pixel array. In any given frame, the number of pixels of a specific architecture which receive no signal is small, and so the estimation of the global

noise is poor.

7.2.2 Local noise

After accounting for chip-wide noise sources, which primarily originate off-chip and can therefore be addressed as discussed in section 7.2.1, the noise level of the pixels still does not provide a satisfactory signal to noise ratio for a single 8 keV x-ray. Several imaging modes can be utilized to locate the source of the signal variability. For example, the pixel can be read out continuously while the pixel reset signal is held high. In reference to figure 6.4, the switch labeled RST, which connects the input and output of the integrating amplifier, remains closed throughout the entirety of framing rather than being opened to permit the accumulation of charge by the pixel. In this configuration, the integrating amplifier output follows V_{ref} . This was verified by sweeping the value of V_{ref} and confirming that the output changed correspondingly.

With the reset signal held high, noise contributions from before the sample and hold amplifier are minimized. Other than noise on V_{ref} itself, which was shown above to be quite low, the amplifier output should be relatively constant. Pixel output standard deviation in this configuration are displayed in table 7.3. These figures are debounced bank averages.

Table 7.3: Pixel noise in reset

Pixel	σ [ADU]	σ [keV]
MM-PAD 2.0	12.11	0.93
Charge dump oscillator	22.74	2.81
Capacitor flip	13.02	1.70
MM-LDO	11.72	0.88

Table 7.4: Pixel noise in low gain

Pixel	C_{low} [fF]	σ_{raw} [ADU]	$\sigma_{debounced}$ [ADU]	$\sigma_{debounced}$ [keV]
MM-PAD 2.0 v1	880	15.20	13.25	22.35
MM-PAD 2.0 v2	2630	15.47	13.38	67.45
CDO	962	17.29	15.70	24.31
Capacitor flip	1000	29.43	14.87	48.48
MM-LDO	880	16.48	14.12	23.38

This indicates that noise contributions from the analog readout chain noise are not dominating the pixel output noise. These values are sufficiently low to obtain the desired signal to noise ratio in framing. Evidently the dominant noise sources are on the front end. Another imaging mode consists of framing with pixel gain starting low and staying low. I.e. the adaptive gain is forced to activate before framing has begun. By increasing the integration capacitance, we may be able to distinguish between a charge injection noise and a voltage noise. A voltage noise on the front end would be seen as a larger equivalent noise charge when integration capacitance is increased, while a charge injection noise should present roughly the same equivalent noise charge in high and low gain. Table 7.4 summarizes the findings. The table lists the standard deviations of banks before and after debouncing. Each half of the MM-PAD 2.0 bank is treated separately because their total low gain capacitances are different.

Here we see that the noise in low gain is very similar to that of the pixel in reset. By comparison, the noise values extracted from the photon histograms, listed in table 7.1, are significantly higher in ADU. This suggests that the pixel noise is dominated by some form of charge injection which is particularly problematic in high gain mode. There is of course some voltage noise as well, as evidenced by the higher equivalent noise change in low gain, but the drastically

reduced noise in terms of ADU imply that charge injection dominates. Relatively large switches were employed in the layout of the HDR-PAD and are a likely candidate for the source of charge injection noise. A rough calculation of the charge that may be injected by such switches follows.

The reset switch in the MM-PAD 2.0 has a width of $6.0\ \mu\text{m}$, a length of $0.36\ \mu\text{m}$, and a multiplicity of two. It is flanked by two dummy switches as described in a previous section, each with the same width and length but multiplicity of one. Based on TSMC 180 nm process parameters, the gate oxide capacitance of the reset switch is $C_{ox} = 8.68\ \text{fF}/\mu\text{m}^2$. The total gate capacitance of the active reset switch is then

$$C_{gate} = 2wlC_{ox}. \quad (7.5)$$

The reset signal swings from 1.8 V to 0 V. If we make the simplifying assumptions that the reset signal swing is fast enough to split injected charge evenly between the front end and the analog output node, and further assume that variations in the quantity of charge injected follows Poisson statistics, the standard deviation of the charge injected to the front end by the reset switch is

$$\sigma_{Q_{inj}} = \sqrt{wlC_{ox}\Delta V} = 649e^- \quad (7.6)$$

in number of electrons. The dummy switch on the front end will inject a quantity of charge from a distribution with the same standard deviation, so the total uncertainty in the quantity of charge injected onto the front end, when these quantities combine, is the standard deviation in equation 7.6 multiplied by $\sqrt{2}$ because the uncertainties add in quadrature. The total uncertainty due to this injected charge is equivalent to $\sim 3.3\ \text{keV}$ signal charge. Note that gate-source and gate-drain capacitances have been neglected.

The calculation above makes several simplifying assumptions, but serves

to illustrate that charge injection from the large switches used to reset the pixels could plausibly be the dominant noise source in HDR-PAD measurements. Large reset switches were employed in the HDR-PAD for handling large signals and resetting the pixels quickly. In simulation, the dummy switches canceled out injected charge very well. It may be that the clocking patterns used in the HDR-PAD can be refined to minimize the charge injection problem, and the switches will actually work to within the design specification. However, more testing and FPGA reprogramming is required.

The figures in table 7.4 also provide an opportunity to verify that the uncertainty of signals which are just large enough to trigger adaptive gain will be measurable with the desired signal to noise ratio. As verified in the high gain photon histograms, roughly 49.8 keV x-rays are sufficient to trigger the MM-PAD 2.0 adaptive gain. Poisson statistics dictate that a measured signal of 49.8 keV x-rays has an inherent uncertainty of ± 7 x-rays. The noise figures in table 7.4 suggest that the uncertainty of a signal in low gain is below this level in all pixels except the MM-PAD 2.0 pixels with a low gain integration capacitance of 2630 fF. If the uncertainty due to the detector is below the uncertainty due to shot noise, the total uncertainty of the measurement is near the experimental minimum, the square root of the measured signal, because the uncertainties add in quadrature. From this we can conclude that a low gain capacitance of 2630 fF is too low with a high gain integration capacitance of 40 fF. To employ this low gain capacitance and still resolve intermediate signals, a third gain stage would be required. However, the low gain capacitances of 880 fF and 1000 fF are small enough to provide Poisson limited measurements of intermediate signals.

CHAPTER 8

CONCLUSIONS

Throughout the course of this dissertation, the need for high dynamic range x-ray detectors at high brightness light sources and the case for developing integrating detectors to meet these needs was demonstrated. Integrating detectors are possibly the only detector architecture which can adequately utilize the capabilities of x-ray free electron lasers, and enhanced flux at third generation synchrotron sources cannot be fully utilized with other technologies, such as photon counting detectors.

The use of a high dynamic range integrating detector, the MM-PAD, in pulsed magnetic field studies at the Advanced Photon Source at Argonne National Lab serves to illustrate the importance of further developing this technology. The studies of Uranium dioxide are on-going, and evidence of its piezomagnetic properties on the atomic scale are being dissected. Further studies are required to draw firm conclusions, but the addition of magnetic field direction switching to these studies promises to shed light on the question of how piezomagnetism might arise from unit cell distortions.

The plasma effect in silicon diodes was investigated by simulating the electron-hole pair clouds generated by XFEL-like scatter with a pulse infrared laser. The results of these studies suggest that charge accumulation in detector pixels stretches to longer time scales than expected due to plasma effects in high density electron-hole pair clouds created in the sensors. These time scales can reach over 1 μs , which is sufficient time for charge removal circuits to provide a meaningful increase to the achievable dynamic range of an integrating pixel.

An initial small scale fabrication of pixel prototype front-ends demonstrated the potential benefit of combining adaptive gain with charge removal techniques. These integrating frameworks were evaluated with direct current injection, and results suggest that they may be capable of integrating continuous x-ray fluxes greater than 10^{11} 8 keV x-rays/pixel/s. The pixel front-ends were developed into fully functional pixels with mixed analog and digital readout. A composite detector consisting of five different pixel architectures was designed which would provide a platform for imaging with and evaluating the performance of all pixel architectures simultaneously.

Fabrication of a 16x16 pixel hybrid detector, development of support hardware and electronics, and refinement of operation resulted in a fully functional hybrid pixel array detector utilizing the prototype front-ends and demonstrated the functionality of the adaptive gain-charge removal combination in measuring high flux x-ray radiation. This culminated in successful measurements of an unattenuated x-ray beam at CHESS with a total flux greater than 10^{11} 9.52 keV x-rays/s spread over roughly twenty pixels.

By comparison, the measurements taken at CHESS represent a two order of magnitude improvement over the original MM-PAD in sustained integrated flux. The HDR-PAD may be able to integrate even higher fluxes, but this was the highest flux available for testing in this experiment. Detectors such as the AGIPD can integrate an average flux of this magnitude, but will saturate after roughly a microsecond. Here the HDR-PAD integrates 1000 times longer than that and does not come close to saturation. Because the CHESS beam is pulsed, the instantaneous flux on the target pixels is substantially higher than 10^{10} 9.52 keV x-rays/pixel/s. Photon counting detectors such as the PILATUS3,

even with re-triggering circuitry to account for pileup, would experience significant non-linearities when measuring a beam with one one-thousandth of the intensity measured here. The architectures tested in the HDR-PAD provide a solid foundation on which to build future detectors, but some lessons should be carried forward.

One significant shortcoming of the HDR-PAD is lack of small signal resolution. Specifically, the HDR-PAD does not achieve the target signal to noise ratio for a signal of one 8 keV x-ray. The most likely cause of this is charge injection due to large reset switches on the pixel front-ends. While large switches may be required for rapid reset in high frame rate experiments, smaller switches would likely suffice. Dummy switches were employed in the HDR-PAD to reduce the magnitude of charge injection, and while seem to be achieving this goal, they also add to the total variability of the detector output. With smaller switches, the magnitude of charge injection would also be smaller and dummy switch charge injection compensation might not be needed at all.

Dummy switches might still be employed if their timing can be controlled independently of the active switches. In future detectors, these signals should be controlled separately to permit fine-tuning of their relative behavior. Alternatively, greater care should be taken to match delays on each signal induced by chip-edge buffers.

The test current source in each pixel of the HDR-PAD was invaluable in debugging the detector operation. Bit shifts and shuffling of data were identified with their use, and they should absolutely be included in future detectors. However, the erratic turning-on of the test source gating did prove to be a nuisance. This behavior can be rectified by the addition of dedicated control signals for

writing to the in-pixel memory bits. Additionally, the current test source output level should be controlled by a current mirror in future chips, rather than an externally defined voltage. While the precision of a test source feeding the integration node of an integrating pixel will never be ideal, this would permit more linear changes in input strength, and would make performing some tests much easier with little downside.

The pixel front-end parasitic capacitance in the HDR-PAD was larger than expected. The current test source is one contributing factor to this capacitance, but another source of this which can be addressed is the protection diode which connects to the supply voltage included on the front-end of each pixel. While some measure of protection should be included in a detector intended for use at XFELs, the smallest possible diode should be used. The oversized switches of the HDR-PAD are certainly another contributor to the parasitic capacitance on the front-end node. Reducing this capacitance will improve the small signal resolution of the pixels provided that charge injection is not the dominant noise source.

Despite these shortcomings, the HDR-PAD represents a step forward in the evolution of high dynamic range integrating detectors. The technology is versatile, and a version of the detector presented here is being adapted for use with electron microscopes, where the high dynamic range combined with area resolution will continue to expand experimental opportunities.

APPENDIX A

LASER PULSE MEASUREMENT SCHEMATICS

Appendix A contains schematics for the printed circuit boards used to measure infrared laser pulses as discussed in Chapter 4. Figure A.1 is the layout of the printed circuit board to which the custom diode was connected. All PCBs in this appendix were designed by Dr. Julian Becker during his time in the Gruner Group at Cornell University.

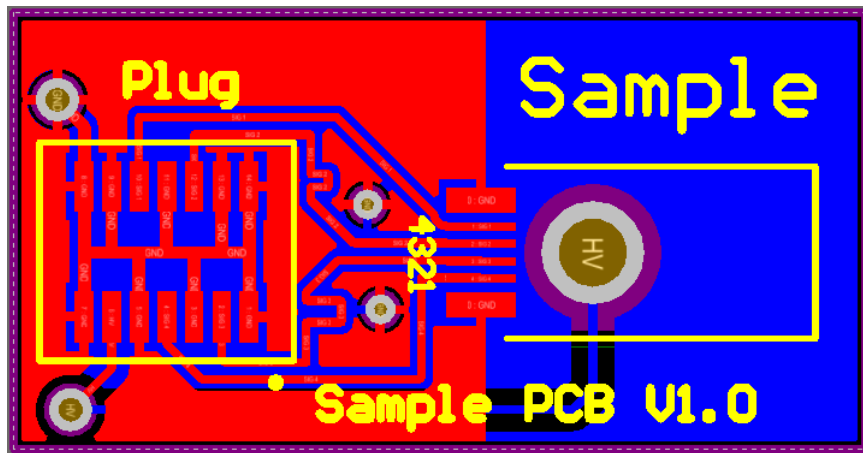
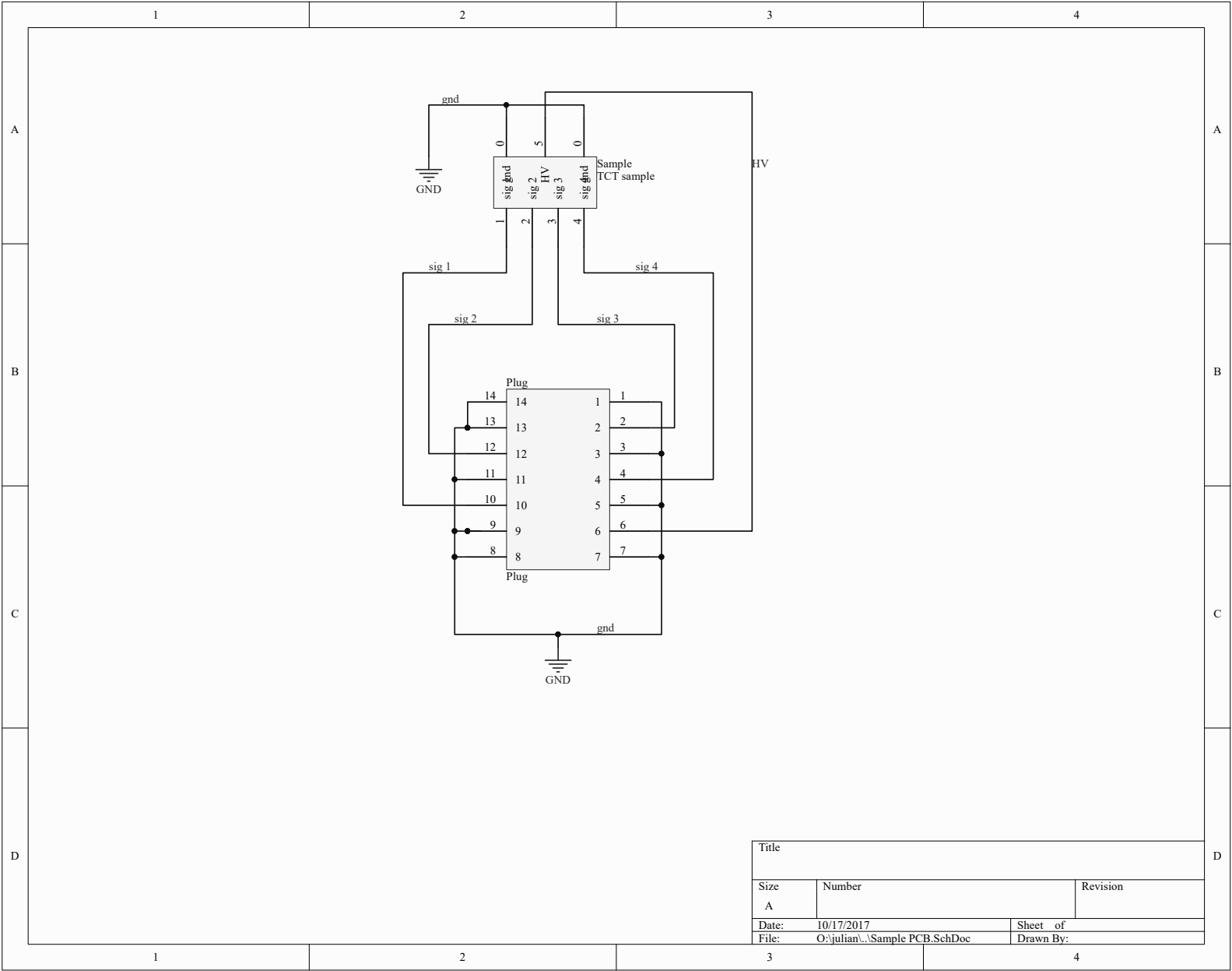
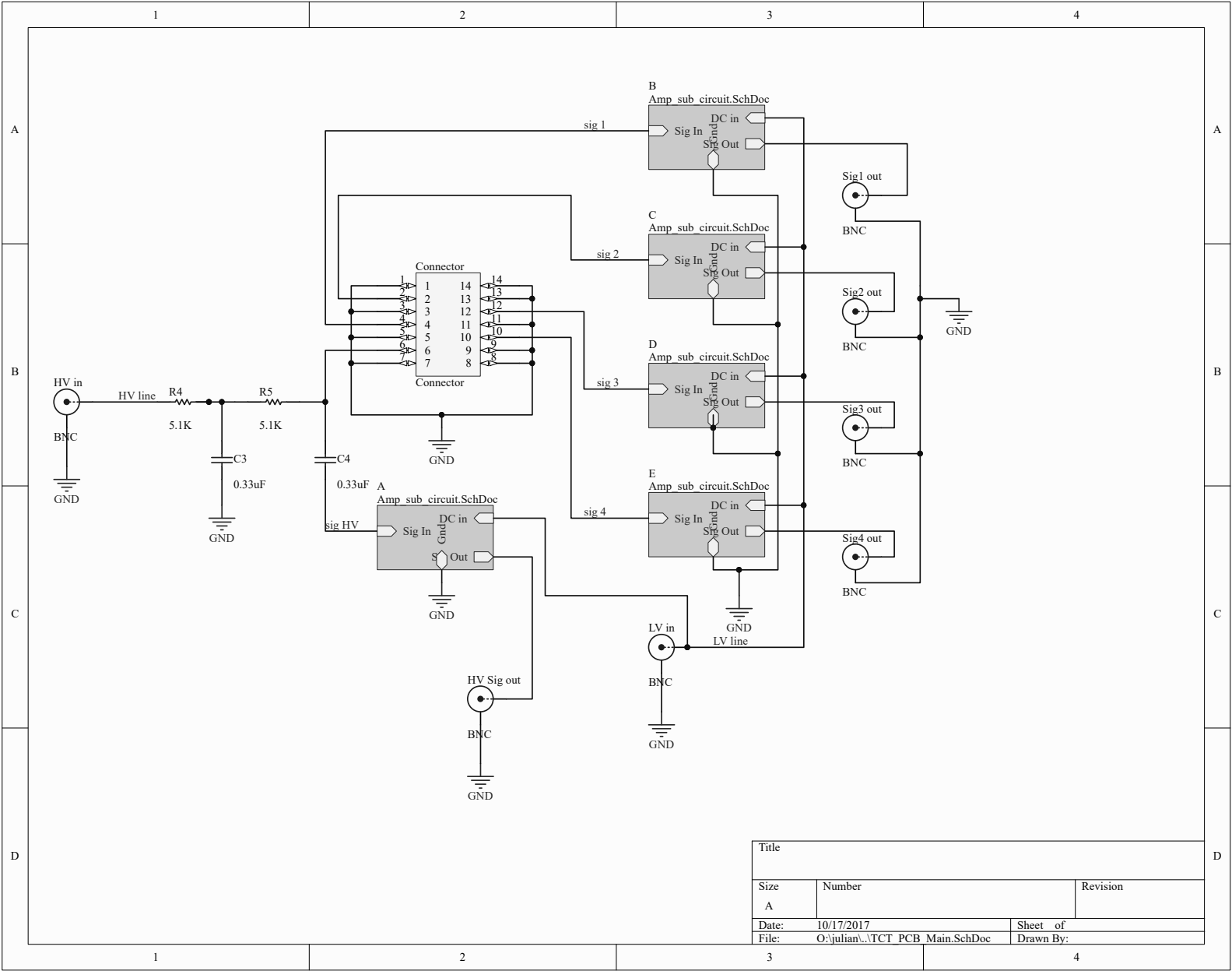


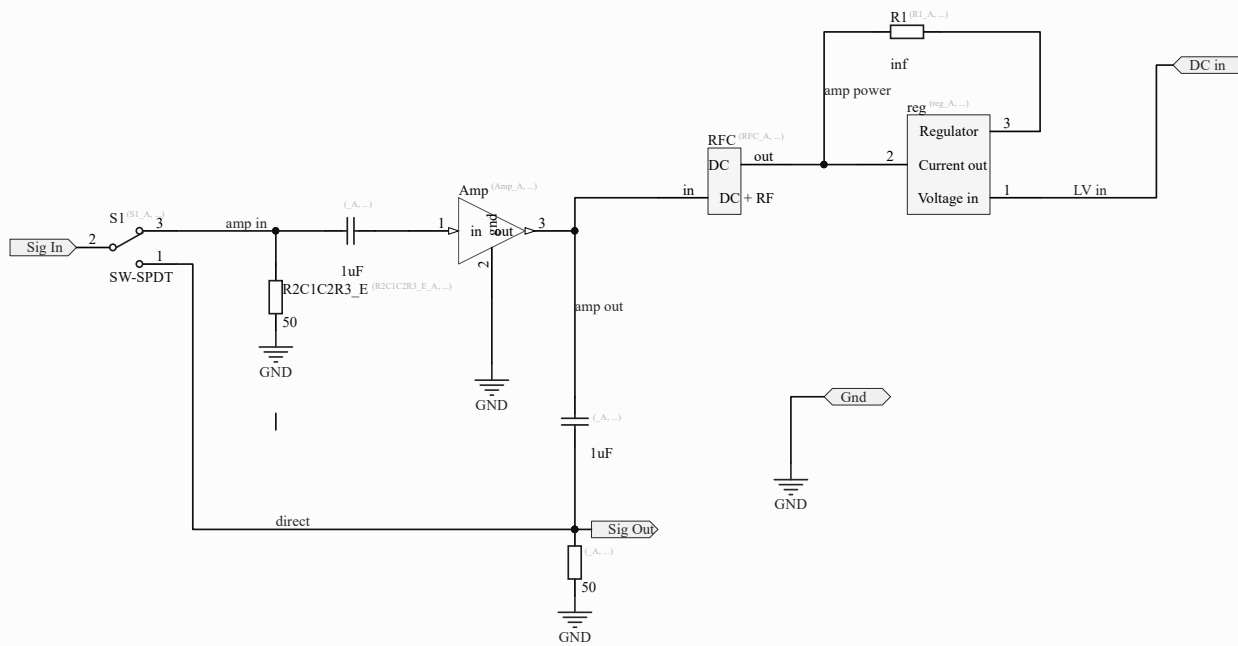
Figure A.1: Layout of sample PCB used in pulsed infrared laser studies discussed in Chapter 4. The circle labeled HV on the right side of the board is punched through to permit laser pulses to strike the diode, which is connected to the ring which supplies the bias voltage. Immediately to the left of this ring are wire bonding pads which are connected directly to pixels on the diode. Signals are routed through a connector to the circuitry for which schematics are provided on subsequent pages.



Title		
Size	Number	Revision
A		
Date:	10/17/2017	Sheet of
File:	O:\julian\Sample PCB.SchDoc	Drawn By:



Title		
Size	Number	Revision
A		
Date:	10/17/2017	Sheet of
File:	O:\julian\TCT_PCB_Main.SchDoc	Drawn By:



Title *			*
Size: A	Number:*	Revision:*	*
Date: 10/17/2017	Time: 10:35:51 AM	Sheet* of *	*
File: O:\julian\Altium\TCT PCB V1\Amp_sub_circuit.SchDoc			*



BIBLIOGRAPHY

- [1] Gabriella Carini, Peter Denes, Sol M. Gruner, and Elianne Lessner. Neutron and x-ray detectors. Technical report, USDOE Office of Science (SC)(United States), 2012. URL http://science.energy.gov/~media/bes/pdf/reports/files/NXD_rpt_print.pdf.
- [2] Keith A Nugent. Coherent methods in the x-ray sciences. *Advances in Physics*, 59(1):1–99, 2010.
- [3] Peter Denes and Bernd Schmitt. Pixel detectors for diffraction-limited storage rings. *Journal of synchrotron radiation*, 21(5):1006–1010, 2014.
- [4] B Henrich, J Becker, R Dinapoli, P Goettlicher, H Graafsma, H Hirsemann, R Klanner, H Krueger, R Mazzocco, A Mozzanica, et al. The adaptive gain integrating pixel detector agipd a detector for the european xfel. *Nuclear Instruments and Methods in Physics Research Section A: Accelerators, Spectrometers, Detectors and Associated Equipment*, 633:S11–S14, 2011.
- [5] Ulrich Trunk, A Allahgholi, J Becker, A Delfs, R Dinapoli, P Göttlicher, Heinz Graafsma, D Greiffenberg, H Hirsemann, S Jack, et al. Agipd: a multi megapixel, multi megahertz x-ray camera for the european xfel. *Proceedings of the SPIE, Volume 10328, id. 1032805 6 pp.(2017).*, 328, 2017.
- [6] N.W. Ashcroft and N.D. Mermin. *Solid State Physics*. HRW international editions. Holt, Rinehart and Winston, 1976. ISBN 9780030839931. URL <https://books.google.com/books?id=oXIfaQAAMAAJ>.
- [7] C. Kittel. *Introduction to Solid State Physics*. Wiley, 2004. ISBN 9780471415268. URL <https://books.google.com/books?id=kym4QgAACAAJ>.

- [8] Jens Als-Nielsen and Des McMorrow. *Elements of modern X-ray physics*. John Wiley & Sons, 2011.
- [9] Göran Wendin. Anomalous x-ray scattering. *Physica Scripta*, 21(3-4):535, 1980.
- [10] M Yoshimatsu and S Kozaki. High brilliance x-ray sources. *X-ray Optics*, pages 9–33, 1977.
- [11] Bernd R David, Hans Barschdorf, Volker Doormann, Rainer Eckart, Geoffrey Harding, Jens-Peter Schlomka, Axel Thran, Peter Bachmann, and Peter Flisikowski. Liquid-metal anode x-ray tube. In *Optical Science and Technology, SPIE's 48th Annual Meeting*, pages 432–443. International Society for Optics and Photonics, 2004.
- [12] Helmut Wiedemann. Synchrotron radiation primer. Technical report, 1998.
- [13] Wolfgang Eberhardt and Franz Himpsel. Next-generation photon sources for grand challenges in science and energy. Technical report, USDOE Office of Science (SC)(United States), 2008.
- [14] Giorgio Margaritondo. *Elements of synchrotron light: for biology, chemistry, and medical research*. Oxford University Press on Demand, 2002.
- [15] Adam P Hitchcock and John J Neville. Applications of synchrotron light to physics and chemistry. *Physics in Canada*, 55:191–198, 1999.
- [16] G Margaritondo, Y Hwu, and G Tromba. Synchrotron light: From basics to coherence and coherence-related applications. volume 3, page 1, 2003.
- [17] S Dierker, U Bergmann, J Corlett, S Dierker, R Falcone, J Galayda, M Gib-

- son, J Hastings, B Hettel, J Hill, et al. Science and technology of future light sources. Technical report, Brookhaven National Laboratory, 2008.
- [18] Katherine Sato Shanks. *Development of low-noise direct-conversion x-ray area detectors for protein microcrystallography*. PhD thesis, Cornell University, 2014.
- [19] James R Janesick. *Scientific charge-coupled devices*, volume 83. SPIE press, 2001.
- [20] R Turchetta, A Fant, P Gasiorek, C Esbrand, JA Griffiths, MG Metaxas, GJ Royle, R Speller, C Venanzi, PF van der Stelt, et al. Cmos monolithic active pixel sensors (maps): developments and future outlook. *Nuclear Instruments and Methods in Physics Research Section A: Accelerators, Spectrometers, Detectors and Associated Equipment*, 582(3):866–870, 2007.
- [21] Takaki Hatsui and Heinz Graafsma. X-ray imaging detectors for synchrotron and xfel sources. *IUCrJ*, 2(3):371–383, 2015.
- [22] SM Gruner, EF Eikenberry, and MW Tate. Comparison of x-ray detectors. In *International Tables for Crystallography Volume F: Crystallography of biological macromolecules*, pages 143–147. Springer, 2006.
- [23] Burton L Henke, Eric M Gullikson, and John C Davis. X-ray interactions: photoabsorption, scattering, transmission, and reflection at $e= 50\text{-}30,000$ ev, $z= 1\text{-}92$. *Atomic data and nuclear data tables*, 54(2):181–342, 1993.
- [24] Stephen E Reichenbach, Stephen K Park, and Ramkumar Narayanswamy. Characterizing digital image acquisition devices. *Optical Engineering*, 30(2): 170–177, 1991.

- [25] Adrian Bevan. *Statistical data analysis for the physical sciences*. Cambridge University Press, 2013.
- [26] Gruner, Sol; Mills, Dennis; Thompson, Al. Detector workshop proposes coordinated detector development for synchrotron facilities. *Synchrotron Radiat. News*, pages 6–8, 2006.
- [27] A Thompson, D Mills, S Naday, S Gruner, P Siddons, J Arthur, R Wehlitz, and H Padmore. A program in detector development for the us synchrotron radiation community. Technical report, 2001.
- [28] Sol Gruner, Mark Tate, Dan Schuette, and Matt Renzi. Integrating pixel array detectors. Technical report, Cornell University, 2005. New Science with New Detectors workshop, ESRF.
- [29] Gerhard Lutz et al. *Semiconductor radiation detectors*, volume 40. Springer, 1999.
- [30] Behzad Razavi and . *Design of analog CMOS integrated circuits*. , 2001.
- [31] Alan Owens and Anthony Peacock. Compound semiconductor radiation detectors. *Nuclear Instruments and Methods in Physics Research Section A: Accelerators, Spectrometers, Detectors and Associated Equipment*, 531(1):18–37, 2004.
- [32] Karlheinz Seeger. *Semiconductor physics*. Springer Science & Business Media, 2013.
- [33] Marius Grundmann. *Physics of Semiconductors*, volume 11. Springer, 2010.
- [34] Helmuth Spieler. *Semiconductor detector systems*, volume 12. Oxford university press, 2005.

- [35] We Shockley and WT Read Jr. Statistics of the recombinations of holes and electrons. *Physical review*, 87(5):835, 1952.
- [36] Christian Brönnimann and Peter Trüb. Hybrid pixel photon counting x-ray detectors for synchrotron radiation. *Synchrotron Light Sources and Free-Electron Lasers: Accelerator Physics, Instrumentation and Science Applications*, pages 1–29, 2014.
- [37] Umesh Mishra and Jasprit Singh. *Semiconductor device physics and design*. Springer Science & Business Media, 2007.
- [38] Simon Min Sze. *Semiconductor devices: physics and technology*. John Wiley & Sons, 2008.
- [39] I Yoshii. Radiation effects on mos devices and radiation-hard cmos technologies. *Nuclear Instruments and Methods in Physics Research Section A: Accelerators, Spectrometers, Detectors and Associated Equipment*, 342(1):156–163, 1994.
- [40] Sandor Lee Barna. *Development of a microsecond framing two-dimensional pixel array detector for time-resolved x-ray diffraction*. PhD thesis, Princeton University, 1997.
- [41] Hugh T Philipp, Marianne Hromalik, Mark Tate, Lucas Koerner, and Sol M Gruner. Pixel array detector for x-ray free electron laser experiments. *Nuclear Instruments and Methods in Physics Research Section A: Accelerators, Spectrometers, Detectors and Associated Equipment*, 649(1):67–69, 2011.
- [42] Winfield Hill and Paul Horowitz. *The art of electronics*. 1989.
- [43] Helmuth Spieler. Semiconductor detector systems. Technical report, 2005.

- [44] Helmuth Spieler. Radiation detectors and signal processing. Technical report, 2001.
- [45] Francois Krummenacher. Pixel detectors with local intelligence: an ic designer point of view. *Nuclear Instruments and Methods in Physics Research Section A: Accelerators, Spectrometers, Detectors and Associated Equipment*, 305(3):527–532, 1991.
- [46] R Ballabriga, M Campbell, E Heijne, X Llopart, L Tlustos, and Winnie Wong. Medipix3: A 64k pixel detector readout chip working in single photon counting mode with improved spectrometric performance. *Nuclear Instruments and Methods in Physics Research Section A: Accelerators, Spectrometers, Detectors and Associated Equipment*, 633:S15–S18, 2011.
- [47] R Ballabriga, M Campbell, EHM Heijne, X Llopart, and L Tlustos. The medipix3 prototype, a pixel readout chip working in single photon counting mode with improved spectrometric performance. In *Nuclear Science Symposium Conference Record, 2006. IEEE*, volume 6, pages 3557–3561. IEEE, 2006.
- [48] Katsuyuki Taguchi, Eric C Frey, Xiaolan Wang, Jan S Iwaczyk, and William C Barber. An analytical model of the effects of pulse pileup on the energy spectrum recorded by energy resolved photon counting x-ray detectors. *Medical physics*, 37(8):3957–3969, 2010.
- [49] P Trueb, BA Sobott, R Schnyder, T Loeliger, M Schneebeili, M Kobas, RP Rassool, DJ Peake, and C Broennimann. Improved count rate corrections for highest data quality with pilatus detectors. *Journal of synchrotron radiation*, 19(3):347–351, 2012.

- [50] P Trueb, C Dejoie, M Kobas, P Pattison, DJ Peake, V Radicci, BA Sobott, DA Walko, and C Broennimann. Bunch mode specific rate corrections for pilatus3 detectors. *Journal of synchrotron radiation*, 22(3):701–707, 2015.
- [51] GA Carini, W Chen, A Dragone, J Fried, J Jakoncic, A Kuczweski, Z Li, J Mead, R Michta, JF Pratte, et al. Tests of small x-ray active matrix pixel sensor prototypes at the national synchrotron light source. *Journal of Instrumentation*, 4(03):P03014, 2009.
- [52] G Mazza, R Cirio, M Donetti, A La Rosa, A Luparia, F Marchetto, and C Peroni. A 64-channel wide dynamic range charge measurement asic for strip and pixel ionization detectors. *IEEE transactions on nuclear science*, 52(4):847–853, 2005.
- [53] MW Tate, D Chamberlain, KS Green, HT Philipp, P Purohit, C Strohman, and SM Gruner. A medium-format, mixed-mode pixel array detector for kilohertz x-ray imaging. In *Journal of Physics: Conference Series*, volume 425, page 062004. IOP Publishing, 2013.
- [54] W Vernon, M Allin, R Hamlin, T Hontz, D Nguyen, F Augustine, SM Gruner, Ng H Xuong, DR Schuette, MW Tate, et al. First results from the 128x128 pixel mixed-mode si x-ray detector chip. In *Proc. SPIE*, volume 6706, page 67060U, 2007.
- [55] WM Jones, Joseph Gordon, and EA Long. The heat capacities of uranium, uranium trioxide, and uranium dioxide from 15 k to 300 k. *The Journal of Chemical Physics*, 20(4):695–699, 1952.
- [56] Ogden G Brandt and Charles T Walker. Temperature dependence of elastic

- constants and thermal expansion for $u o 2$. *Physical Review Letters*, 18(1):11, 1967.
- [57] Paolo Santini, Stefano Carretta, Giuseppe Amoretti, Roberto Caciuffo, Nicola Magnani, and Gerard H Lander. Multipolar interactions in f-electron systems: The paradigm of actinide dioxides. *Reviews of Modern Physics*, 81(2):807, 2009.
- [58] M Jaime, A Saul, M Salamon, VS Zapf, N Harrison, T Durakiewicz, JC Lashley, DA Andersson, CR Stanek, JL Smith, et al. Piezomagnetism and magnetoelastic memory in uranium dioxide. *Nature Communications*, 8, 2017.
- [59] DE Moncton, E Crosbie, and GK Shenoy. Overview of the advanced photon source. *Review of Scientific Instruments*, 60(7):1403–1405, 1989.
- [60] Zahirul Islam, Dana Capatina, Jacob PC Ruff, Ritesh K Das, Emil Trakhtenberg, Hiroyuki Nojiri, Yasuo Narumi, Ulrich Welp, and Paul C Canfield. A single-solenoid pulsed-magnet system for single-crystal scattering studies. *Review of Scientific Instruments*, 83(3):035101, 2012.
- [61] Ulrich Wolfgang Arndt and Bertram Terence Martin Willis. Single crystal diffractometry. *Single Crystal Diffractometry, by UW Arndt, BTM Willis, Cambridge, UK: Cambridge University Press, 2009*, 2009.
- [62] Julian Becker, Doris Eckstein, Robert Klanner, and Georg Steinbrück. Impact of plasma effects on the performance of silicon sensors at an x-ray fel. *Nuclear Instruments and Methods in Physics Research Section A: Accelerators, Spectrometers, Detectors and Associated Equipment*, 615(2):230–236, 2010.

- [63] B Henrich, J Becker, R Dinapoli, P Goettlicher, H Graafsma, H Hirsemann, R Klanner, H Krueger, R Mazzocco, A Mozzanica, et al. The adaptive gain integrating pixel detector agipd a detector for the european xfel. *Nuclear Instruments and Methods in Physics Research Section A: Accelerators, Spectrometers, Detectors and Associated Equipment*, 633:S11–S14, 2011.
- [64] A Jablonski. The nist electron effective-attenuation-length database. *Journal of Surface Analysis*, 9(3):322–325, 2002.
- [65] Martin A Green. Self-consistent optical parameters of intrinsic silicon at 300k including temperature coefficients. *Solar Energy Materials and Solar Cells*, 92(11):1305–1310, 2008.
- [66] Julian Becker, Doris Eckstein, Robert Klanner, and Georg Steinbrück. Impact of plasma effects on the performance of silicon sensors at an x-ray fel. *Nuclear Instruments and Methods in Physics Research Section A: Accelerators, Spectrometers, Detectors and Associated Equipment*, 615(2):230–236, 2010.
- [67] Mihaela Dinu. Dispersion of phonon-assisted nonresonant third-order nonlinearities. *IEEE journal of quantum electronics*, 39(11):1498–1503, 2003.
- [68] HK Tsang and Y Liu. Nonlinear optical properties of silicon waveguides. *Semiconductor Science and Technology*, 23(6):064007, 2008.
- [69] Zhong He. Review of the shockley–ramo theorem and its application in semiconductor gamma-ray detectors. *Nuclear Instruments and Methods in Physics Research Section A: Accelerators, Spectrometers, Detectors and Associated Equipment*, 463(1):250–267, 2001.
- [70] Antonio J López-Martín, Sushmita Baswa, Jaime Ramirez-Angulo, and Ramón González Carvajal. Low-voltage super class ab cmos ota cells with

very high slew rate and power efficiency. *IEEE Journal of Solid-State Circuits*, 40(5):1068–1077, 2005.

- [71] M Manghisoni, D Comotti, L Gaioni, L Lodola, L Ratti, V Re, G Traversi, and C Vacchi. Novel active signal compression in low-noise analog readout at future x-ray fel facilities. *Journal of Instrumentation*, 10(04):C04003, 2015.
- [72] Ramón González Carvajal, Jaime Ramírez-Angulo, Antonio J López-Martín, Antonio Torralba, Juan Antonio Gómez Galán, Alfonso Carlosena, and Fernando Muñoz Chavero. The flipped voltage follower: A useful cell for low-voltage low-power circuit design. *IEEE Transactions on Circuits and Systems I: Regular Papers*, 52(7):1276–1291, 2005.
- [73] J Ramirez-Angulo and M Holmes. Simple technique using local cmfb to enhance slew rate and bandwidth of one-stage cmos op-amps. *Electronics Letters*, 38(23):1409–1411, 2002.
- [74] Lucas Koerner. *X-ray analog pixel array detector for single synchrotron bunch time-resolved imaging*. PhD thesis, Cornell University, 2010.
- [75] Li Dong-Mei, Wang Zhi-Hua, Huangfu Li-Ying, and Gou Qiu-Jing. Study of total ionizing dose radiation effects on enclosed gate transistors in a commercial cmos technology. *Chinese Physics*, 16(12):3760, 2007.
- [76] Giovanni Maria Anelli. Design and characterization of radiation resistant integrated circuits for the lhc particle detectors using deep sub-micron cmos technologies. 2000.
- [77] Li Chen and Douglas M Gingrich. Study of n-channel mosfets with an enclosed-gate layout in a 0.18/ μm cmos technology. *IEEE Transactions on Nuclear Science*, 52(4):861–867, 2005.

- [78] Bing J Sheu and Chenming Hu. Switch-induced error voltage on a switched capacitor. *IEEE Journal of solid-state Circuits*, 19(4):519–525, 1984.
- [79] Weize Xu and Eby G Friedman. Clock feedthrough in cmos analog transmission gate switches. In *ASIC/SOC Conference, 2002. 15th Annual IEEE International*, pages 181–185. IEEE, 2002.
- [80] Yongwang Ding and Ramesh Harjani. A universal analytic charge injection model. In *Circuits and Systems, 2000. Proceedings. ISCAS 2000 Geneva. The 2000 IEEE International Symposium on*, volume 1, pages 144–147. IEEE, 2000.
- [81] Christoph Eichenberger and Walter Guggenbuhl. On charge injection in analog mos switches and dummy switch compensation techniques. *IEEE Transactions on Circuits and Systems*, 37(2):256–264, 1990.